Modified Track-Etched Membranes using Photocatalytic Semiconductors for Advanced Oxidation Water Treatment Processes

by

Arnoux Rossouw

Thesis presented in partial fulfilment of the requirements for the degree of Master of Science in Engineering in Electronic Engineering in the Faculty of Engineering at Stellenbosch University

Department of Electrical and Electronic Engineering,
University of Stellenbosch,
Private Bag X1, Matieland 7602, South Africa.

Supervisor: Prof W.J. Perold

March 2013

Declaration

By submitting this thesis electronically, I declare that the entirety of the work contained therein is my own, original work, that I am the sole author thereof (save to the extent explicitly otherwise stated), that reproduction and publication thereof by Stellenbosch University will not infringe any third party rights and that I have not previously in its entirety or in part submitted it for obtaining any qualification.

Date: March 2013

Abstract

Modified Track-Etched Membranes using Photocatalytic Semiconductors for Advanced Oxidation Water Treatment Processes

A. Rossouw

Department of Electrical and Electronic Engineering,
University of Stellenbosch,
Private Bag X1, Matieland 7602, South Africa.

Thesis: MScEng (Electronic)

March 2013

The purpose of this study was to develop modified tract-etched membranes using nanocomposite TiO_2 for advanced water treatment processes. Photocatalytic oxidation and reduction reactions take place on TiO_2 surfaces under UV light irradiation, therefore sunlight and even normal indoor lighting could be utilised to achieve this effect. In membrane filtration, caking is a major problem, by enhancing the anti-fouling properties of photocatalysts to mineralise organic compounds the membrane life and efficiency can be improved upon.

In this study the first approach in nanocomposite membrane development was to directly modify the surface of polyethylenetherephthalate (PET) track-etched membranes (TMs) with titanium dioxide (TiO_2) using inverted cylindrical magnetron sputtering (ICMS) for TiO_2 thin film deposition. The second approach was first to thermally evaporate silver (Ag) over the entire TM surface, followed by sputtering TiO_2 over the silver-coated TM. As a result a noble metal-titania nanocomposite thin film layer is produced on top of the TM surface with both self-cleaning and superhydrophilic properties. Reactive inverted cylindrical magnetron sputtering is a physical vapour deposition method, where material is separated from a target using high energy ions and then re-assimilated on a substrate to grow thin films. Argon gas is introduced simultaneously into the deposition chamber along with O_2 (the reactive gas) to form TiO_2. The photocatalytic activity and other film properties, such as crystallinity can be influenced by changing the sputtering power, chamber pressure, target-to-substrate distance, substrate temperature, sputtering gas composition and flow rate. These characteristics make sputtering the perfect tool for the preparation of different kinds of TiO_2 films and nanostructures for photocatalysis.

In this work, the utilisation of ICMS to prepare photocatalytic TiO_2 thin films deposited on track-etched membranes was studied in detail with emphasis on band-gap reduction and TM surface regeneration. Nanostructured TiO_2 photocatalysts were

prepared through template directed deposition on track-etched membrane substrates by exploiting the good qualities of ICMS. The TiO_2-TM as well as Ag-TiO_2-TM thin films were thoroughly characterised. ICMS prepared TiO_2 films were shown to exhibit good photocatalytic activities. However, the nanocomposite Ag-TiO_2 thin films were identified to be a much better choice than TiO_2 thin films on their own. Finally a clear enhancement in the photocatalytic activity was achieved by forming the Ag-TiO_2 nanocomposite TMs. This was evident from the band-gap improvement from 3.05 eV of the TiO_2 thin films to the 2.76 eV of the Ag-TiO_2 thin films as well as the superior surface regenerative properties of the Ag-TiO_2-TMs.

Uittreksel

Gemodifiseerde baan-geëtste membrane met fotokatalitiese halfgeleiers vir gevorderde oksidasie in waterbehandelingsprosesse

("Modified Track-Etched Membranes using Photocatalytic Semiconductors for Advanced Oxidation Water Treatment Processes")

A. Rossouw

Departement Elektriese en Elektroniese Ingenieurswese,
Universiteit van Stellenbosch,
Privaatsak X1, Matieland 7602, Suid-Afrika.

Tesis: MScIng (Elektronies)

Maart 2013

Die doel van hierdie studie was om verbeterde baan-geëtste membrane (BMe) met behulp van nano-saamgestelde titaandioksied (TiO_2) vir gevorderde water behandeling prosesse te ontwikkel. Fotokatalitiese oksidasie- en reduksie reaksies vind plaas op die TiO_2 oppervlaktes onder UV-lig bestraling, en dus kan sonlig en selfs gewone binnenshuise beligting gebruik word om die gewenste uitwerking te verkry. In membraan filtrasie is die aanpaksel van onsuiwerhede 'n groot probleem, maar die verbetering van die self-reinigende eienskappe van fotokatalisators deur organiese verbindings te mineraliseer, kan die membraan se leeftyd en doeltreffendheid verbeter word.

In hierdie studie was die eerste benadering om nano-saamgestelde membraan ontwikkeling direk te verander deur die oppervlak van polyethylenetherephthalate (PET) BMe met 'n dun lagie TiO_2 te bedek, met behulp van reaktiewe omgekeerde silindriese magnetron verstuiwing (OSMV).Die tweede benadering was eers om silwer (Ag) termies te verdamp oor die hele BM oppervlak, gevolg deur TiO_2 verstuiwing bo-oor die silwer bedekte BM. As gevolg hiervan is 'n edelmetaal-titanium nano-saamgestelde dunfilm laag gevorm bo-op die oppervlak van die BM, met beide self-reinigende en verhoogde hidrofiliese eienskappe. OSMV is 'n fisiese damp neerslag metode, waar materiaal van 'n teiken, met behulp van hoë-energie-ione, geskei word, en dan weer opgeneem word op 'n substraat om dun films te vorm. Argon gas word gelyktydig in die neerslag kamer, saam met O_2 (die reaktiewe gas), vrygestel om TiO_2 te vorm. Die fotokatalitiese aktiwiteit en ander film eienskappe, soos kristalliniteit, kan beïnvloed word deur die verandering van byvoorbeeld die verstuiwingskrag, die druk in die reaksiekamer, teiken-tot-substraat afstand, substraattemperatuur, verstuiwing gassamestelling en vloeitempo. Hierdie eienskappe maak verstuiwing die ideale hulpmiddel vir die voorbereiding van die verskillende soorte TiO_2 films en nanostrukture vir fotokatalisasie.

In hierdie tesis word OSMV gebruik ter voorbereiding van fotokatalitiese TiO_2 dunfilms, wat gedeponeer is op BMe. Hierdie films word dan in diepte bestudeer, met die klem op bandgaping vermindering en BM oppervlak hergenerasie. Nano-gestruktureerde TiO_2 fotokataliste is voorberei deur middel van sjabloongerigte neerslag op BM substrate deur die ontginning van die goeie eienskappe van OSMV. Die TiO_2-BM dunfilms, sowel as Ag-TiO_2-BM dunfilms, is deeglik gekarakteriseer. OSMV voorbereide TiO_2 dunfilms toon goeie fotokatalitiese aktiwiteite. Nano-saamgestelde Ag-TiO_2 dunfilms is egter geïdentifiseer as 'n veel beter keuse as TiO_2 dunfilms. Ten slotte is 'n duidelike verbetering in die fotokatalitiese aktiwiteit bereik deur die vorming van die Ag-TiO_2 nano-saamgestelde BMe. Dit was duidelik uit die bandgapingverbetering van 3,05 eV van TiO_2 dunfilms in vergelyking met die 2,76 eV van Ag-TiO_2 dunfilms. 'n Duidelike verbetering is behaal in die fotokatalitiese aktiwiteit deur die vorming van die Ag-TiO_2 nano-saamgestelde TMs.

Acknowledgements

I would not be here today if it was not for the grace of God and the people he put along my way.

I would especially like to thank:

Mr Ulrich Büttner for his continued support and opening my eyes to studying further;

Prof Perold who took a chance on me and agreed to be my supervisor, despite my eccentric tendencies;

Prof Maaza for broadening my horizons and introducing me to nuclear physics;

Dr Carlos Pineda for all those extra hours he put in helping me to analyse data;

Prof Leslie Petrik for sending me to Russia and always being there when I needed her;

Alex and Olga, спасибо большое. ты мой дом далеко от дома.

My parents and little sister, no matter what, you always believe in me.

Friends and colleagues, you made it one hell of a ride. Thanks for the good times.

And last but not least, cupcakes, appreciate everything xoxo.

Contents

List of Figures

List of Tables

Nomenclature

Abbreviations

AFM	:	Atomic Force Microscopy
Ag	:	Silver
atm	:	atmospheric pressure
CB	:	Conduction Band
CVD	:	Chemical Vapour Deposition
DC	:	Direct Current
eV	:	electron Volt
FWHM	:	Full Width at Half-Maximum of the rocking curve
ICMS	:	Inverted Cylindrical Magnetron Sputtering
PC	:	Polycarbonate
PET	:	Polyethylenetherephthalate
PIXE	:	Particle-induced X-ray emission
PLD	:	Pulsed Laser Deposition
PMR	:	Photocatalytic membrane reactor
PVD	:	Physical Vapour Deposition
QCM	:	Quartz Crystal Microbalance
RBS	:	Rutherford Backscattering Spectrometry
RF	:	Radio Frequency
R6G	:	Rhodamine 6G
SEM	:	Scanning Electron Microscope
TiO_2	:	Titanium Dioxide
TM	:	Track-etched membrane
UV	:	Ultraviolet
VB	:	Valence Band
XRD	:	X-ray Diffraction

Units

Kilo	:	10^{3}
Milli	:	10^{-3}
Micro	:	10^{-6}
Nano	:	10^{-9}
Ångström (Å)	:	10^{-10} m

Chapter 1

Introduction

Thin films are material layers ranging in thickness from one monolayer of atoms or molecules to several micrometres. The upper thickness limit is somewhat vague, but usually thin film thicknesses are in the nanometre range (i.e. below 1μm). Thin films are all around us in everyday life. For example, all modern electronic devices rely on thin film technologies that allow the preparation of integrated circuits, where a huge number of transistors or other devices are prepared simultaneously on a single silicon wafer. Thin films are used in optical components such as camera lenses, sunglasses and filters for anti-reflection and scratch-proof properties. Mirrors, windows, flat panel displays, DVDs and CDs are all examples of applications of thin film technology.

As part of the recent "nanoboom", functional thin films in the nanometre range are often connected with nanotechnology, although no real nanoscale phenomenon exists. Nevertheless, thin films are increasingly being applied to all sorts of new applications and the existence of a nanoscale effect is not really that important as long as the film has all the desired properties. One of these new application areas is photocatalysis, which is the main topic of this thesis. Photocatalysis is the catalysis of a spontaneous chemical reaction, where light is required for the catalyst to function. A photocatalyst can transform light energy into chemical energy by creating strong redox (reductive and oxidative) species, which greatly enhance the rate of the spontaneous reaction. During this transformation the photocatalyst itself remains intact and unchanged. Photocatalysts are heterogeneous catalysts, usually in the form of a thin film or powder. Studies related to photocatalysis have increased immensely over the past few years and currently hundreds of research papers are published annually [1].

Photocatalytic materials have raised a lot of attention lately in application areas such as water and air purification and sterilisation. Also, photocatalytic self-cleaning tiles, windows and building materials are currently used in many locations to confront various pollution and fouling related problems. Titanium dioxide (TiO_2) is usually the material of choice for photocatalytic applications, because it has often been found to possess the best stability and activity when compared to other materials. TiO_2 also has the ability to turn superhydrophilic when irradiated [2]. Thus, water will easily wash out any accumulated dirt from the film surface, thereby adding to TiO_2 a second self-cleaning functionality. TiO_2 also has some limitations, the biggest being the fact that it requires UV irradiation to function as a photocatalyst. The bandgap of anatase TiO_2 is 3.2 eV (λ= 388 nm) makes the utilisation of indoor and solar light very inefficient for photocatalysis, because only a small percentage of the available radiation can be

used. Doping TiO_2 with additional elements or creating composite photocatalysts are common solutions to increase the absorbance of visible light, but care should be taken not to destroy the good qualities of TiO_2 in the process.

In photocatalytic water treatment processes, a high reactive surface area is vital for optimum performance. When maximising the surface area, many factors have to be considered. The diffusion of reactants should be rapid in and out of the surface region. Light is a prerequisite for the photocatalytic reactions, therefore the geometry should be such that the light is able to reach all the available surface areas. Powdered photocatalysts have high surface areas and consequently good activities, but their separation after water purification processes is extremely intense and presents a problem. For this reason immobilised photocatalysts with high surface areas have been sought after by pioneering materials with nanoscale geometries. Thin film deposition methods can be used to prepare nanostructured photocatalysts, but due to the complex three-dimensional structures and large surface areas involved, highly conformal film growth is required.

Reactive inverted cylindrical magnetron sputtering (ICMS) is a physical gas phase deposition method where material is separated from a target using high energy ions and then re-assimilated on the substrate surface to grow a thin film. Argon is typically used as the sputtering gas. The method is principally very straightforward. Ideally, the growing film will have the same composition as the target. In the case of oxides, however, the films tend to become oxygen deficient. For this reason reactive sputtering is often used, where a reactive gas like O_2 is introduced simultaneously into the deposition chamber. Doping can be accomplished by adding yet another gas such as N_2 [3]. The photocatalytic activity and other film properties such as crystallinity can be influenced by changing the sputtering substrate temperature, sputtering power or pressure and sputtering gas composition [4, 5, 6]. These characteristics make sputtering the perfect tool for the preparation of diverse, undoped and doped TiO_2 films and nanostructures for photocatalysis.

1.1 Motivation and objectives

From a technological and scientific point of view, it is interesting to study nanostructured materials, either because the particles interact with a surrounding matrix material or because their properties may be modified as a function of their particle size, or both. Those smart materials whose mechanisms are based on phase transitions, such as metal-semiconductor transformations, are particularly intriguing, since the associated property changes when induced by external perturbations can be rapid and reversible. This is certainly true for the specific case of the titanium dioxide, TiO_2 and Ag-TiO_2 composite films.

The main objective of this research has been to explore physical properties of thin solid film materials and to carry out fundamental research studies for describing the relationship between growth parameters, structure/composition and physical properties of TiO_2 and nanoplasmonic Ag-TiO_2.

1.2 Aims of the Thesis

The aims of the proposed research project are as follows:

- The development of advanced composite materials based on membrane and photovoltaic catalyst technology;
- To develop the needed technologies to fabricate functional TiO_2 and plasmonic nanostructured Ag-TiO_2 thin films for advanced oxidation water treatment processes by inverted cylindrical magnetron sputter deposition;
- To characterise the modified nanostructures in order to carry out the structural, morphological, interfacial and optical properties of the latter and also to understand the properties of these optically active nanosystems;
- To develop a prototype setup for testing hybrid water treatment technology.

1.3 Structure of the Thesis

Chapter 2 gives a short literature survey and the state of the art of TiO_2 thin film photocatalysis.

Chapter 3 is dedicated to a description of the experimental procedure used in the fabrication of the samples and to explain the different techniques employed throughout this work to characterise their structure, morphology and optical properties.

Chapter 4 reports the results of synthesis and feasibility of the produced TiO_2 and Ag-TiO_2 by a novel physical vapour deposition method, named inverted cylindrical magnetron sputtering (hollow cathode sputtering). Structural, morphological, interfacial analyses and optical properties of synthesized TiO_2 and Ag-TiO_2 nanocomposite thin films are discussed in detail.

Chapter 5 summarises the aforementioned work done and highlights the outlook for the possible continuation of this research project.

Chapter 2

Literature review

The literature review presented in this chapter defines the thesis topic presented in Chapter 1. The research design, refinement and delimitations from which the topic was studied were also developed from the perspective gained from the literature review.

2.1 Advanced water treatment technologies

The use of waste water and conventional water treatment processes becomes increasingly challenged with the identification of more contaminants, industrial activities, rapid growth of population and the diminishing availability of water resources. Three emerging treatment technologies, namely advanced oxidation processes (AOPs), UV irradiation and membrane filtration, hold great promise in providing alternatives for better protection of the environment and public health. With the advances in the manufacturing industry and the growing knowledge base, the applications of these technologies will increase at an exceptional rate in the not too distant future [7].

2.1.1 Advanced oxidation processes

Oxidation is defined as the transfer of one or more electrons from an electron donor (reductant, which has a lower affinity for electrons) to an electron acceptor (oxidant, which has a higher affinity for electrons). These electron transfers result in the chemical transformation of both the reductant and the oxidant, in some cases resulting in chemical species with an odd number of valence electrons. These species, known as radicals, are inclined to be highly unstable, and thus highly reactive because of their unpaired electron.

Oxidation reactions that produce radicals tend to start a chain response. They are inclined to be followed by additional oxidation-reduction reactions between the radical oxidants and other reactants, both organic and inorganic, until thermo-dynamical stability is reached. An oxidant's ability to initiate chemical reactions is measured in terms of its oxidation potential. The most powerful oxidants are fluorine, hydroxyl radicals, ozone and chlorine with respective oxidation potentials of 2.84 V, 2.70 V, 2.07 V and 1.49 V [8]. The end products of complete oxidation of organic compounds (i.e. mineralisation) are carbon dioxide (CO_2) and water (H_2O).

AOPs are made up of the two stages of oxidation discussed above, firstly, the formation of a strong oxidant (such as hydroxyl radicals) and secondly, the reaction of these oxidants with the organic contaminants in water. However, the term advanced oxidation processes refer specifically to the process in which organic contaminants are oxidised, primarily through their reactions with hydroxyl radicals [9].

In water treatment applications, AOPs usually refer to a particular subset of processes that involves ozone (O_3), hydrogen peroxide (H_2O_2) and/or UV light. However, in this study, AOPs will be used to refer to the general group of processes involving titanium dioxide (TiO_2), producing hydroxyl radicals, which can react with and destroy a wide range of organic contaminants. In general, the effectiveness of AOPs is directly proportional to their ability to generate hydroxyl radicals.

2.1.2 Membrane processes

Membrane processes are separation techniques which are widely applied in different sectors of industry including chemical, petrochemical, pharmaceutical, electronic, cosmetic, water desalination, water and wastewater treatment and many more.

The main advantages of membrane processes are:

1. Low energy consumption;
2. Automatic control and stable operation, allowing performance of a continuous nature;
3. Production of water of stable quality almost independent of the quality of the treated water;
4. Easy scale-up by simple connection of additional membrane modules.

The disadvantages of membrane processes are:

1. Membrane fouling due to particles and colloids present in the feed stream;
2. A limited lifetime of the membranes.

Up to now only two types of membrane techniques have found application in photocatalytic membrane reactors, namely:

1. Pressure driven membrane processes;
2. Processes that make use of a concentration (or partial pressure) difference as the driving force.

Pressure driven membrane processes can be classified into:

- Microfiltration (MF);
- Ultrafiltration (UF);

- Nanofiltration (NF);
- Reverse osmosis (RO).

Because of the driving force, i.e. the applied pressure, the solvent and various solute molecules permeate through the membrane, whereas other molecules or particles are rejected to various extents dependent on the structure of the membrane. The size (or molecular weight) of the particles or molecules separated diminishes from MF through UF and NF to RO, and consequently the pore sizes in the membranes are smaller. As a result, the resistance of the membranes to mass transfer increases and hence the applied pressure (driving force) has to be increased to obtain the same flux [10]. The MF membranes are able to reject particles and dissolved molecules larger than 0.1 μm. In UF the particles and dissolved molecules smaller than 0.1 μm and larger than 2 nm are separated. The NF membranes can reject particles and dissolved molecules smaller than 2 nm. In RO the applied transmembrane pressure causes selective movement of solvent against its osmotic pressure difference and as a result almost complete separation of salts, metal ions or small organic molecules is obtained [11].

The other group of membrane techniques which have found application in PMRs includes dialysis, pervaporation and direct contact membrane distillation. Dialysis is a process where solutes diffuse from one side of the nonporous membrane (feed side) to the other side (the dialysate or permeate side) according to their concentration gradients. Separation between the solutes is obtained as a result of differences in diffusion rates across the membrane arising from differences in molecular size and difference in solubility [10]. Pervaporation is a process in which a binary or multicomponent liquid mixture is separated by a partial vaporization through a dense membrane. The driving force for the mass transfer of permeants from the feed side to the permeate side of the membrane is the difference of chemical potentials of the permeants across the membrane. This difference can be created by reducing the partial pressure on the permeate side of the membrane, either by using a vacuum pump or by using a sweeping gas. In PV, separation of a mixture results from the differences in the solubilities of the components in the membrane and from the differences in the diffusivities of these components through the membrane. Separation during pervaporation does not depend on the liquidÐvapour equilibrium, thus this process can be used for the separation of azeotropes or close-boiling liquids [12]. Direct contact membrane distillation is a process of evaporation of feed volatile components through a porous hydrophobic membrane. During the process, the gas phase is maintained inside the pores of the membrane. The driving force of the mass transfer through the membrane pores is a vapour pressure difference on both sides of the membrane, which depends on the temperature and the solution's composition in the layers adjacent to the membrane. For solutions containing non-volatile solutes only water vapour is transferred through the membrane, hence the obtained distillate comprises demineralized water [13, 14].

2.1.2.1 Why track-etched membranes?

Track-etch membranes (TMs) offer distinct advantages over conventional membranes due to their precisely determined structure. Their pore size, shape and density can be varied in a controllable manner so that a membrane with the required transport and retention characteristics can be produced. The use of heavy ion accelerators made

it possible to vary the linear energy transfer (LET) of track-forming particles, angle distribution of pore channels and pore lengths. So far the track formation and etching process have been studied in detail for several polymeric materials. Today we understand the determining factors and have numerous empirical data enabling us to manufacture any particular product based on polyethylene terephthalate (PET) or polycarbonate (PC) films. Pore shape can be made cylindrical, conical, funnel-like, or cigar-like at will. A number of modification methods have been developed for creating TMs with special properties and functions. Applications of "conventional" track membranes can be categorised into three groups, namely process filtration, cell culture, and laboratory filtration. Nuclear track pores find diverse applications as model systems and as templates for the synthesis of micro- and nanostructures.

The process of track formation and etching in polyethylene terephthalate is well-studied [15, 16]. PET is rather stable in acids, organic solvents, biologically inert, and mechanically strong. A high etch rate ratio is achievable (when using UV sensitisation), which makes it possible to produce a wide range of membranes with different pore diameters. The etching procedure is simple and fast. Alkaline solutions (sometimes with additives) are used to develop tracks. The membranes are relatively hydrophilic without any additional modification.

Polycarbonate is the material that has been used for track membrane production since the seventies [17]. The production technology is very close to that for PET. Compared to PET, the sensitivity of PC is higher, which makes it possible to produce membranes with a pore diameter as small as 0.01 μm without the UV sensitisation stage. Polycarbonate track membranes differ from PET membranes, exhibiting a lower resistance to organic solvents and a lower wettability.

Track membranes are known as precise porous films with a very narrow pore size distribution [18, 19, 20]. A unique property of TMs is that the number of pores and the pore size are two almost independent parameters, which can be varied over a very wide range. The pore diameter can be from 10 nm to tens of micrometers. The pore density can vary from 1 to 10^{10} cm^{-2}. No other type of membrane provides such a possibility. In most cases the pore geometry is very simple (cylinders, cones or combinations of these), which leads to simple relationships between the membrane structure parameters and transport characteristics, such as the gas or water flow rate. Poiseuillc and Knudsen formulae adequately describe the viscous flow and the molecular flow through a track membrane [21]. In the production process the finished membrane is normally subjected to rigorous testing by scanning electron microscopy, gas and water flow rate methods, bubble point, and some other measurements [22, 23].

The determining factors are currently well understood and numerous empirical data exist, enabling us to manufacture any particular product based on PET and PC. Pore shape can be made cylindrical, conical, funnel-like, and cigar-like at will. Various asymmetric structures can be also produced [19]. The scanning electron micrographs in Fig. 2.1 illustrate the variety of pore structures in track membranes.

The separation properties of TMs depend, first of all, on the structure parameters. In the absence of adsorption, the track membrane acts as a "screen" membrane. The retention of particles is determined by the relationship between the pore diameter and the particle size [24, 25]. If the surface of the membrane adsorbs the particles, the retention characteristics change drastically. In this case the result depends on the nature of the membrane surface and the nature of the particles, and also depends on

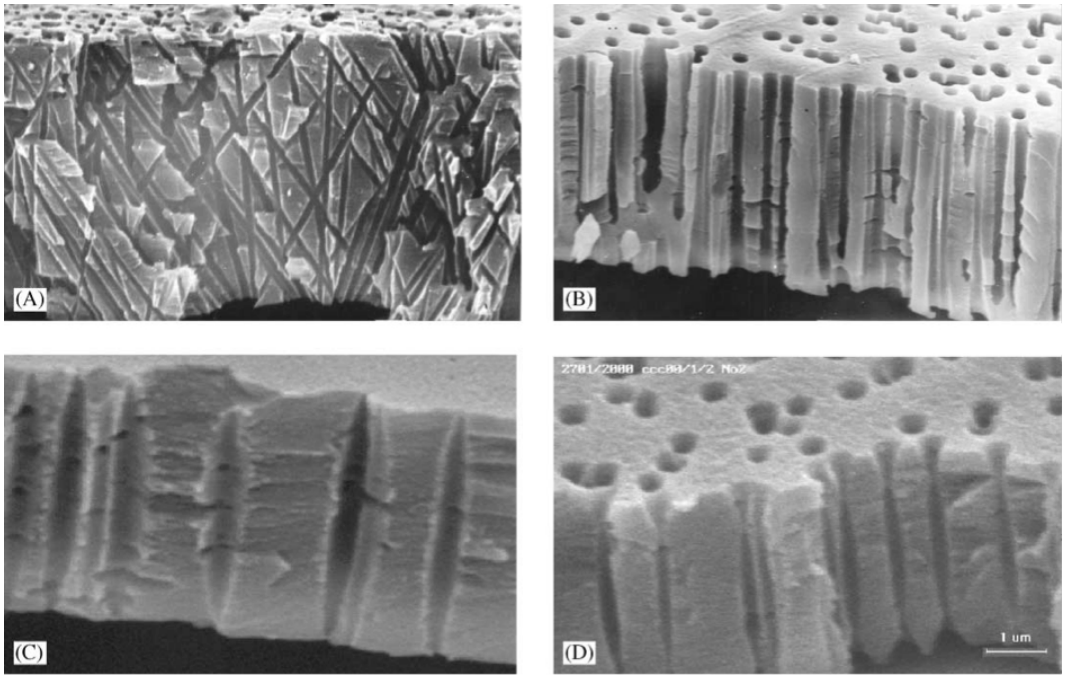

Figure 2.1: Examples of porous structures produced in thin polymeric films using various methods of irradiation and chemical treatment: (A) cross section of a polycarbonate TM with cylindrical non-parallel pore channels; (B) polypropylene TM with slightly conical (tapered towards the centre) parallel pores; (C) polyethylene terephthalate TM with cigar-like pores; (D) polyethylene terephthalate TM with "bow-tie" pores [19].

pH, presence of surfactants, etc. [26, 27]. Adsorption of solutes leads to a decrease in the filtration rate or to the loss of a substance that is expected to pass through the membrane [28, 29]. An example is sorption of proteins onto the PET membrane surface that is negatively charged at medium and high pH. To solve such problems, track membranes with various specific surface properties have to be manufactured.

Applications of commercially produced track membranes can be categorized into three groups:

1. Process filtration;
2. Cell culture;
3. Laboratory filtration.

The process of filtration implies the use of membranes, mostly in the form of cartridges with a membrane area of at least 1 m^2. Purification of deionised water in microelectronics, filtration of beverages, separation and concentration of various suspensions are typical examples. There is a strong competition with other types of membranes available on the market. Casting membranes often provide a higher dirt loading capacity and a higher throughput. For this reason the use of track membranes in this field is still limited [30].

In recent years a series of products were developed for use in the domain called cell and tissue culture [31, 32, 33, 34]. Adapted over the years to a variety of cell types, porous membrane filters are now recognised as providing significant advantages

for cultivating cells and studying the cellular activities such as transport, absorption and secretion [35]. The use of permeable support systems based on TMs has proven to be a valuable tool in cell biology [36]. A traditional application of track membranes is laboratory filtration [37]. TM is a very good instrument when small particles should be collected onto the membrane surface and analysed. For such purposes track membranes are delivered in the form of disks and filtration kits.

The use of track-etch pores (often specially produced for a certain experiment) for solving various scientific tasks should be mentioned separately. One-pore [19, 38], oligo-pore [39] and multi-pore samples can serve as unique models for studying the transport of liquids, gases, particles, solutes, electrolytes [21, 40, 41], and electromagnetic waves [42] through narrow channels. Many experiments of this kind are relevant to biological and medical topics [43]. Track membranes can also serve as templates for making various micro- and nanostructures. Magnetic, conducting and superconducting nanowires, possessing special properties, have been manufactured in this way [44, 45, 46, 47]. Using small-pore TMs as matrices, electrically switchable ion-selective membranes and sensors can be produced [48].The advantage of TMs over conventional membranes is their precisely determined structure. However, many large-scale applications are "insensitive" to such a brilliant property of TMs. Track membranes occupy a niche in biological, medical, analytical and scientific applications. This type of membrane is indispensable for the manipulation of small particles of living and any other matter. Track membranes seem to be the best porous material for providing a controllable transport of solutes. Further progress in TM technology can be connected with the creation of membranes having particular properties for a particular use. Membranes that do not adsorb proteins, membranes with various functional groups on the surface, etc., might be developed and introduced into industry.

2.1.3 Hybrid water treatment processes

When hybrid photocatalysis-membrane processes are conducted in an installation, it is often referred to as a photocatalytic membrane reactor (PMR).

However, the literature is full of other names for these configurations:

- Membrane reactor [49];
- Membrane chemical reactor (MCR) [50];
- Membrane photoreactor [49];
- Photocatalysis-ultrafiltration reactor (PUR) [51];
- Submerged membrane photocatalysis reactor [52].

Since all these names relate to the hybridisation of membrane processes in conjunction with photocatalysis, the general term of "photocatalytic membrane reactor" (PMR) will be used from this point onwards.

Photocatalytic membrane reactors can be divided into two principal groups:

1. Reactors with catalyst suspended in the feed solution;

2. Reactors with catalyst supported on/in membranes.

In the case of the first group, membrane filtration may be used as a single step for the complete recovery of catalyst particles from a solution [49]. The major disadvantages of such a configuration are membrane fouling and deterioration of the permeate flux, which are particularly observable in the case of pressure-driven membrane techniques. A solution for this problem might be the application of photocatalytic membranes. In this configuration, oxidation (by hydroxyl radicals) occurs on the external surface and within the pores of the membrane, whilst reactants are permeating in a one-pass flow. However, fixation of the photocatalyst often results in a loss of photoactivity [53]. Furthermore, proper UV and hydroxyl radical resistant membrane selection is necessary.

In both configurations, i.e. utilising photocatalyst in suspension or immobilised on/in a membrane, the membrane might act as a barrier for the molecules which are degraded and products and by-products of their decomposition. However, this role strongly depends on the separation characteristics of the membrane used and the membrane process applied. The products and by-products of photodecomposition of organics are, in general, low molecular weight compounds. Therefore, in case of pressure driven membrane processes, only NF and RO might be considered as processes able to separate these substances.

2.2 Titanium dioxide

Titanium dioxide (TiO_2) is found in nature in mainly one of three crystal structures, namely anatase, rutile and brookite. TiO_2 is mechanically and chemically very stable. It has a melting point of 1843°C and is water, hydrochloric acid (HCL), nitric acid (HNO_3) and diluted sulphuric acid (H_2SO_4) insoluble. However, it can be dissolved in hot, concentrated sulphuric acid (H_2SO_4) and hydrofluoric acid (HF) [54]. The extent of solubility depends on the specific structure, rutile being less soluble than anatase. TiO_2 can be prepared from its crude ore by first reducing titanium with carbon and reacting with chlorine at high temperatures to yield $TiCl_4$. Liquid $TiCl_4$ can be purified by distillation and further reacted with oxygen to yield pure TiO_2. TiO_2 can also be separated from ilmenite by the sulfate process. The ore is dissolved in sulfuric acid where iron (II) sulfate crystallizes and is filtered off. The remaining titanium salt can then be further processed to give pure TiO_2. TiO_2 is nontoxic and bio-compatible, making it a suitable material for various implants. It is used in many consumer products such as toothpaste, lipstick, paints, food additives and pharmaceuticals [55, 56, 57].

2.2.1 Mineralogical forms and physic-chemical properties of TiO_2

TiO_2 usually crystallizes in one of the three principal structures, namely anatase, rutile and brookite [58, 59, 60], as can be seen in Fig. 2.2 below.

Brookite is more difficult to prepare and is rarer too. Thus rutile and anatase properties have been studied much more than those of brookite. The basic building block of rutile and anatase is a distorted TiO_6 octahedron. In both structures two

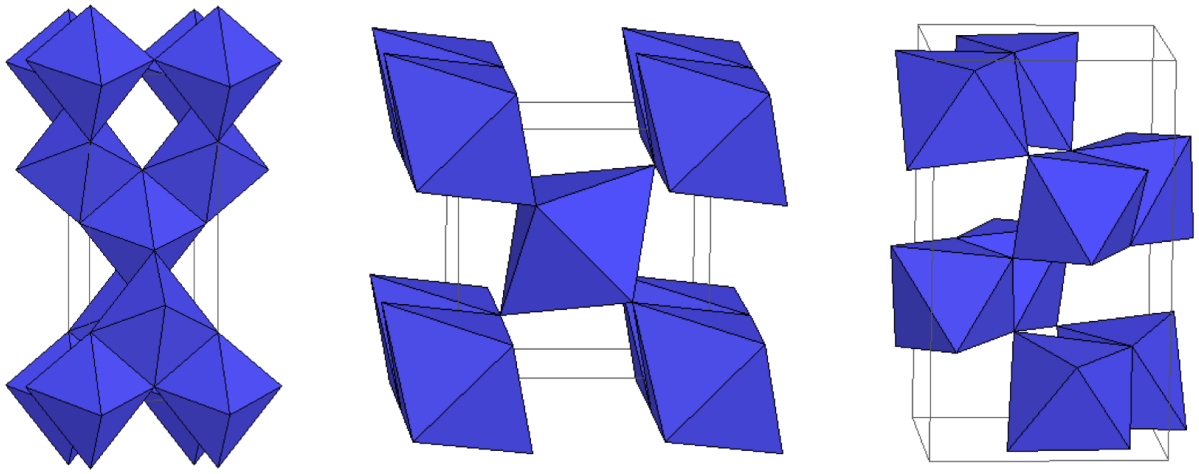

Figure 2.2: Crystal structures for (a) anatase, (b) rutile and (c) brookite TiO_2 [61]

TiO_2	Anatase	Rutile	Brookite
Crystal system	Tetragonal	Tetragonal	Rhombohedral
Melting point (°C)	1843	1843	1843
Density (g/cm^3)	3.830	4.240	4.170
Molar Volume	13.625	18.693	25.738
Optical properties	Uniaxial (-)	Uniaxial (+)	Biaxial (+)
bandgap (eV)	3.26	3.05	???

Table 2.1: Crystal properties of the three main polymorphs of TiO_2

opposite Ti-O bonds are slightly longer than the other four. The TiO_6 octahedra are more distorted in anatase, which results in differences in the TiO_6 octahedra stacking arrangements in the two structures. As a consequence, the crystal faces with the lowest energy are (110) and (100) for rutile, and (101) and (001) for anatase. These crystal faces are thus the most common for polycrystalline samples and understanding their surface chemistry is important [57].

Even though the structures of anatase and rutile are similarly based on octahedra (TiO_6), they still differ from one another by the distortion of each octahedral and by the assembly patterns of the octahedral chains. Anatase is built up from octahedra which are mainly connected by their vertices. Octahedral structures in rutile are mostly connected by the edges. Both vertical and edge connections are found in the octahedral structure of the brookite form. Although both anatase and rutile are the same tetragonal system, anatase has longer vertical axes of the crystals than rutile. On the other hand, brookite crystallizes in the orthorhombic system.

Moreover, rutile is the most stable phase of titanium dioxide, while anatase and brookite are metastable phases. The metastable structures are almost as stable as rutile at normal pressure and temperature, because of small difference in the Gibbs free energy (4-20 kJ/mol) between three phases [62]. Other crystal properties of all three forms of TiO_2 [61] are shown in Table 2.1.

2.2.2 Electrical and optical properties of TiO_2

Anatase and rutile TiO_2 are n-type semiconductors with bandgaps of 3.2 eV and 3.05 eV respectively [63]. The conductivity of TiO_2 is dependent on the oxygen deficiency through creation of defects such as oxygen vacancies, Ti^{3+} and Ti^{4+} interstitials and crystallographic shear planes (CSP) [57]. Oxygen deficiency is easily created in TiO_2, especially when the preparation is done in a vacuum. The amount of oxygen deficiency and thus the conductivity can also be adjusted after preparation by heat treatment in oxygen-rich or reducing atmospheres. The nature and amount of other impurities can also largely affect the electrical properties of TiO_2. Hydrogen impurities, for example, can increase the electrical conductivity [64, 65, 66]. Impurities can be incorporated intentionally or they can be residues from the preparation process. The electrical properties of TiO_2 thus depend strongly on the preparation method and sample history [57]. Various molecules can cause a measurable change in the conductivity when they interact with the TiO_2 surface. For this reason TiO_2 has been studied for various gas sensing applications [67, 68, 69, 70].

The dielectric constant (k) of TiO_2 is 40 for anatase and 86 to 170 for rutile (depending on crystal orientation) [57, 71, 72]. TiO_2 has therefore been studied as a high-k insulator for metal-oxide-semiconductor field-effect transistors (MOSFET) and dynamic random access memories (DRAM) [73, 74, 75, 76]. The biggest limitation for the use of TiO_2 as an insulator is the high leakage caused by its relatively wide bandgap and n-type conductivity. Especially, the easy creation of oxygen deficiency contributes to the increased conductivity. Various solutions for decreasing the leakage currents in TiO_2 thin films have been attempted. These include the passivation of grain boundaries by fluoride [77, 78], using high O_3 concentrations during preparation [74], doping with Al [79] and deposition of nanolaminates [80, 81, 82], for example. On the other hand, the oxygen vacancies can have an important role in the future of non-volatile random access memories (NVRAM). Recently, a $Pt/TiO_2/Pt$ memristor device capable of fast bipolar non-volatile switching was reported [83]. The switching in this device was shown to be caused by the drift of oxygen vacancies in TiO_2 by an applied electric field.

TiO_2 is transparent to visible wavelengths as can be concluded from its bandgap energy. The refractive index of TiO_2 is the highest of all oxides [57]. The index is even higher than that of diamond, and thus large and pure TiO_2 crystals have gem-like reflectance, refraction and brilliance and are suitable for use in jewellery [54]. The high refractive index has also enabled the wide use of TiO_2 as a white pigment and also in many other optical applications [84]. Because TiO_2 absorbs UV light and is biocompatible it is used in sunscreens.

2.2.3 TiO_2 as a photocatalyst

Scientific interest in the photocatalytic properties of TiO_2 has been increasing from the early 1990s. Hundreds of research papers are published annually on the subject [85, 86, 87, 88, 89, 90, 91, 92, 93, 94, 95, 96, 97, 98, 99, 100, 101, 102, 103]. There is a great amount of information about TiO_2 photocatalysis. A vast amount of these articles are focused on powder materials and only a limited amount deals with thin films of TiO_2. Although this work is focused on thin films, a general understanding

of the material properties of all forms of TiO_2 is required, because many important studies and major advances in photocatalytic materials are often reported on powder samples first.

A photocatalyst is a material which can induce various oxidative and reductive chemical reactions on its surface in the presence of light. ΔG° for the net reaction is always negative. A photoinduced reaction with a positive ΔG° is termed photosynthesis [92]. Photocatalytic materials can be used to purify contaminated air and water, or to split water into oxygen and hydrogen [85, 103]. Photoreduction of carbon dioxide and various metal ions have been examined [97, 104]. Additionally, photocatalytic reactions can be used to keep surfaces sterile and clean [85, 92, 98].

Other applications for photocatalysis are:

- Photocatalytic lithography [85];
- Self-cleaning clothes [58, 98];
- Self-sterilizing catheters [85];
- Cancer treatment [98];
- Self-cleaning tent materials [85];
- NO_x removing pavement and cement [85].

Detailed mechanisms of photocatalysis can be quite complex, but the basic principles are usually the same. The process begins with the absorption of light with energy greater than the bandgap of the semiconducting photocatalyst (Fig. 2.3). In the case of TiO_2 this energy is 3.2 eV for the anatase phase and 3.05 eV for the rutile phase. After absorbtion of a photon, an electron-hole-pair is created within the photocatalyst. Some of these electron-hole-pairs recombine immediately and release the energy as heat. Some of the electrons and holes avoid recombination and diffuse to the surface of the photocatalyst, where they participate in charge transfer reactions with available surface species, while the photocatalyst itself remains intact. The electrons and holes can either react directly with the target compounds or indirectly by forming first superoxide ($O_2^{\bullet -}$), singlet oxygen ($^1O_2$), hydroxyl radicals ($^\bullet OH$) or hydrogen peroxide (H_2O_2) from O_2, H_2O and OH groups which are typically present in atmospheric conditions. Virtually any organic compound can be decomposed to CO_2, H_2O and mineral acids by these active oxygen species when the photocatalyst is irradiated with light of sufficient energy. Especially the OH radical is a very strong oxidant. Also, direct oxidation of the target compound by the photogenerated hole is possible.

In brief, the mechanism of the photocatalytic oxidation of organic compounds under UV light can be presented as follows:

$$
\begin{aligned}
TiO_2 + h\nu &\rightarrow TiO_2(e_{CB^-} + h_{VB^+}) \\
TiO_2(h_{VB^+}) + H_2O &\rightarrow TiO_2 + H^+ + {}^\bullet OH \\
TiO_2(h_{VB^+}) + OH^- &\rightarrow TiO_2 + {}^\bullet OH \\
TiO_2(e_{CB^-}) + O_2 &\rightarrow TiO_2 + O_{2\bullet -} \\
O_{2\bullet -} + HO_{2\bullet} &\rightarrow TiO_2 + HO_{2\bullet} \\
HO_{2\bullet} + HO_{2\bullet} &\rightarrow H_2O_2 + O_2 + O_2
\end{aligned}
$$

$$
\begin{aligned}
\mathrm{TiO_2}(e_{CB^-}) + \mathrm{H_2O_2} &\rightarrow \mathrm{OH^\bullet} + \mathrm{OH^-} \\
\mathrm{H_2O_2} + \mathrm{O_{2\bullet -}} &\rightarrow \mathrm{OH^\bullet} + \mathrm{OH^-} + \mathrm{O_2} \\
\mathrm{H_2O_2} + + h\nu &\rightarrow 2\mathrm{OH^\bullet} \\
\text{Organic compound} + \mathrm{OH^\bullet} &\rightarrow \text{Degradation products} \\
\text{Organic compound} + \mathrm{TiO_2}(h_{VB^+}) &\rightarrow \text{Oxidation products} \\
\text{Organic compound} + \mathrm{TiO_2}(e_{CB^-}) &\rightarrow \text{Reduction products}
\end{aligned}
$$

The chemical reaction is graphically represented in Fig. 2.5.

It is not always easy to know which mechanisms are operating and to what extent in different photocatalytic systems, as their occurrence is dependent on the properties of the photocatalyst, the nature of the compound being oxidized and the surrounding medium (water, air or vacuum). The only sure thing is that the reduction reactions

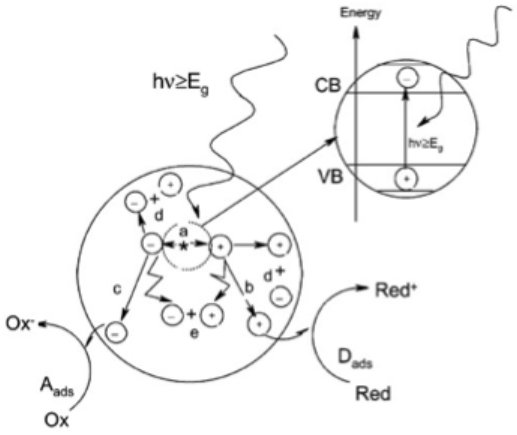

Figure 2.3: Main processes occurring on a semiconductor particle: (a) electron-hole generation; (b) oxidation of donor (D); (c) reduction of acceptor (A); (d) and (e) electron-hole recombination at surface and in bulk, respectively [92].

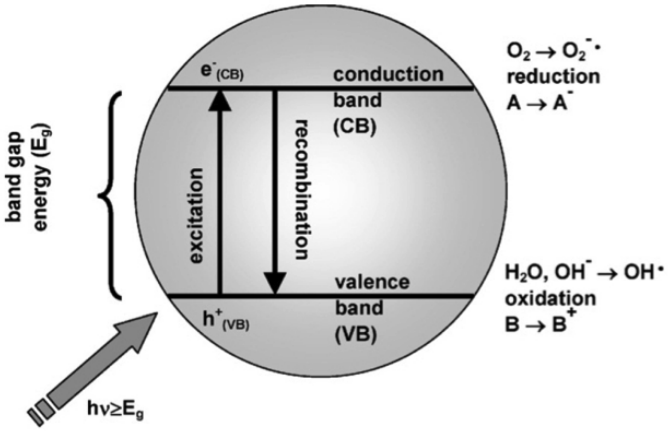

Figure 2.4: Idea of photocatalysis: A, electron acceptor; B, electron donor [105, 106].

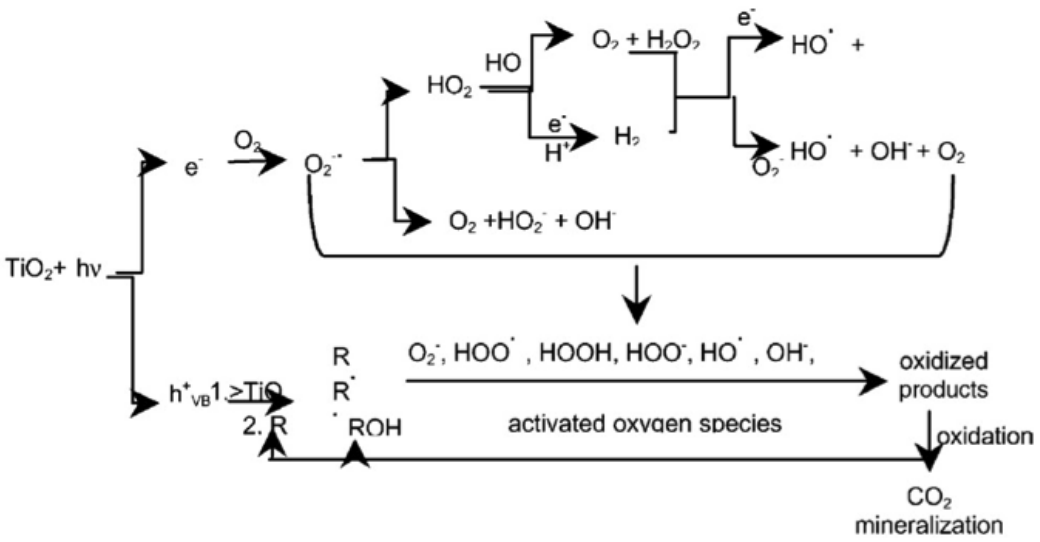

Figure 2.5: Secondary reactions with activated oxygen in the mechanism of photo-oxidative mineralization of organic compounds [88].

by the photogenerated electrons and oxidation reactions by the photogenerated holes must balance precisely so that the photocatalyst itself remains intact.

TiO_2 has been frequently found to possess the best photocatalytic properties. The biggest factor limiting its applicability is the size of its bandgap, because the wavelength of light needed for its excitation lies in the UV region of the electromagnetic spectrum. The differences in lattice structures of anatase and rutile TiO_2 cause different densities and electronic band structures, leading to different bandgaps (for bulk materials: anatase 3.20 eV and rutile 3.05 eV) [98, 107]. Therefore, the absorption thresholds correspond to 388 nm and 405 nm wavelength for the two titania forms, respectively.

This means that TiO_2 can use only a very small portion of the solar energy and an even smaller fraction of normal indoor lighting. A stable photocatalyst that could operate under visible light has therefore been the subject of many studies in the past ten years.

2.2.4 Noble metal loaded TiO_2 photocatalyst

In composite TiO_2 photocatalysts the properties of some other materials are combined with TiO_2 in order to produce enhanced photocatalytic performance [86, 108, 109, 110, 111, 112, 113, 114]. The role of the other material can be, for instance, better absorption of visible light [108, 109, 110], better adsorptive capabilities [113], increased superhydrophilicity [111, 112], or it can be used to improve charge separation to prevent the recombination of photogenerated electrons and holes [108, 109, 114].

The photocatalytic activity of TiO_2 can be increased by adding noble metals on the surface [86, 87, 93, 97]. This creates a Schottky barrier in the metal-TiO_2 interface, which prevents electron back injection into TiO_2 and thereby reduces electron-hole recombination, thus improving the charge separation. More holes can therefore reach the TiO_2 surface to initiate photo-oxidation reactions. The electrons in the noble metal

can react with oxygen for example [93]. Pt and Ag are the most common noble metals that have been used for TiO_2 surface modification. Ag has also antimicrobial properties, which makes it an obvious choice for photocatalytic sterilization applications.

There is always an optimum noble metal surface loading that leads to the best photocatalytic activity. Because noble metals block the UV radiation quite efficiently, the number of photons reaching the TiO_2 decreases with increasing metal loadings. At some point the light blocking effect starts to outweigh the effects of the better charge separation. Also, with high metal loadings the increased negative charge of the metal particles can attract the holes in the TiO_2 too much, causing the metal particles essentially start acting as recombination centres [93]. This occurs especially if the trapped electrons are not further transferred out from the metal [100].

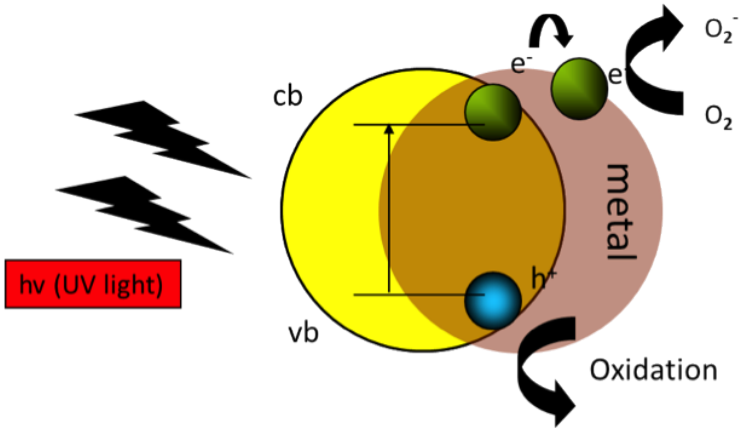

Figure 2.6: Schematic of the main processes occurring on an Ag-TiO_2 composite photocatalyst.

2.3 Photocatalytic titanium dioxide thin films

The previous section focused on the general characteristics of TiO_2 photocatalyst materials. This section describes how the photocatalytic properties are manifested in thin film TiO_2 materials and gives examples of different preparation methods.

2.3.1 Self-cleaning surfaces

Due to photocatalytic reactions a TiO_2 surface can potentially be self-cleaning in the presence of UV (or visible) light. The rate of destruction/removal of the surface contaminants should, of course, be higher than the rate of deposition of the contaminant. If a too thick layer of contaminant accumulates on the photocatalytic surface, it will eventually block all the necessary UV light and the photocatalytic reactions will cease. Also, photocatalytic reactions cannot remove particles of stable materials, such as sand dust. Thus, in many situations photocatalysis alone would not be enough to make the surface self-cleaning in practice. Fortunately, TiO_2 surfaces have another property, in addition to photocatalysis, which contributes to the self-cleaning ability. The photoinduced superhydrophilic effect was reported in 1997 by Wang et al. and since then it

has been under intensive study [115]. It was shown that, upon UV irradiation, the surface of TiO_2 turns highly hydrophilic. The contact angle between a water droplet and the surface approaches zero and instead of forming droplets, water forms a thin film on the surface which remains clear and transparent.

The water droplet contact angle is measure of the angle subtended from a tangent on the surface of the water droplet to the surface upon which it rests. This is marked as θ_c in Fig. 2.7.

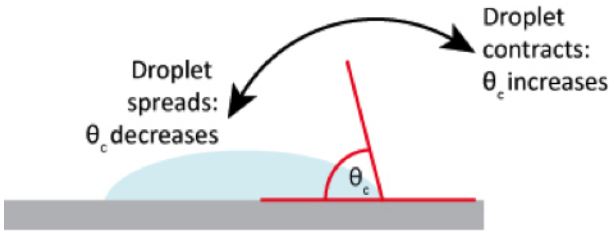

Figure 2.7: Schematic representation of the contact angle.

A three-dimensional representation of hydrophobic versus hydrophilic behaviour is given in Fig. 2.8. If a surface is hydrophilic, the water droplet contact angle is low. The droplet spreads, because the surface has an affinity for water. If the surface is hydrophobic, the water droplet contact angle is high and the droplet contracts, because the surface does not have an affinity for water. As the photoinduced hydrophilicity of a sample is observed, the droplet spreads, its diameter increases, and its contact angle decreases.

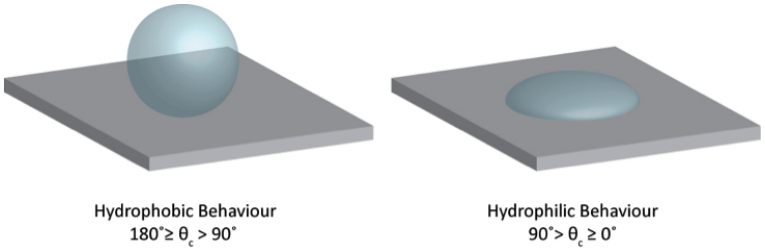

Figure 2.8: 3D representation of hydrophobic and hydrophilic behaviour of a droplet of water.

Different explanations for the photoinduced superhydrophilic effect have been given in the literature. The first proposed model involves the ejection of oxygen atoms from the TiO_2 lattice, leading to the generation of surface oxygen vacancies [115, 116]. These defects are known to cause water dissociation, which would then cause an increase in the number of surface hydroxyl groups and an increase in surface hydrophilicity [82]. The second model proposes that significant reconstruction of the surface hydroxyl groups occurs upon UV irradiation [117]. An increased amount of metastable, more weakly bound hydroxyl groups are claimed to be present after UV irradiation, causing a more hydrophilic surface. The third, perhaps the most simple explanation, suggests that the superhydrophilicity is an inherent property of clean TiO_2 surfaces and that the

observed decrease in water contact angles upon UV irradiation is just caused by the photocatalytic oxidation of surface hydrocarbon contaminants [90, 118, 119, 120].

Despite the on-going debate about the actual mechanisms, the discovery of the superhydrophilic property caused a keen interest towards TiO_2 surfaces and many applications began appearing on the market. Photocatalytic TiO_2 thin films can be used as self-cleaning surfaces to tackle fouling issues in many environments. Perhaps the most well known examples are self-cleaning windows manufactured by Pilkington, PPG and Saint-Gobain. The operation of these windows is bifunctional. Photocatalytic reactions on the surface of TiO_2 break down accumulated organic dirt and thus clean the surface whenever there is UV light present. Due to the superhydrophilicity of the irradiated TiO_2 any dirt on the surface should also be easily washed away by water. Besides windows, photocatalytic self-cleaning surfaces have been demonstrated to prevent fouling in many other applications, such as bathroom tiles, lamp covers in a highway tunnel, building walls etc. [1, 121]. Because water droplets cannot form on a superhydrophilic surface, it always remains clear and fog-free. The anti-fogging ability of TiO_2 surfaces has been exploited in bathrooms and car side-view mirrors, for example [121].

2.3.2 Antimicrobial surfaces

Due to the strong oxidative power of the photogenerated active oxygen species, photocatalytic surfaces can have antimicrobial properties [1, 122]. As extremely small amounts of microbes can be potentially dangerous, their destruction using photocatalysis is sensible. Various bacteria, endotoxins, fungal spores and biofilm components can be photocatalytically oxidized to CO_2, H_2O and mineral acids [1, 122, 123]. A hybrid material, where TiO_2 is modified with antimicrobial metals, such as Ag and Cu, can have very good sterilizing properties [1]. First the outer membrane of the bacterium cell is breached by photocatalytic oxidation, after which the antimicrobial metal ions can diffuse inside the cell, thus becoming much more lethal for the bacterium [85]. Photocatalytic antimicrobial surfaces have potential uses in hospital environments to combat dangerous microbes such as Methicillin-resistant Staphylococcus aureus (MRSA) and Escherichia coli [124]. Detoxification and antimicrobial activity are also important in air and water purification systems [125]. Biofilm growth on surfaces is a serious problem in many industrial processes, such as the paper machine environment, and photocatalytic coatings have been considered as a solution [126].

2.3.3 Photocatalytic activity measurements

Measurement of the photocatalytic activity of a thin film sample is relatively straightforward. The compound to be degraded is brought in contact with the TiO_2 film, which is irradiated by UV or visible light. The degradation reaction is followed as a function of time by some standard analysis technique, such as gas or liquid chromatography or IR or UV/VIS spectroscopy. Due to the use of different test compounds (liquid, gas or solid) and different irradiation sources (fluorescent, halogen, solar), direct comparison of photocatalytic activities of TiO_2 samples reported by different research groups is difficult. A good idea, to make the comparison easier, would be to use a widely available TiO_2 film, such as Activ™ glass, as a reference sample [127].

Rhodamine 6G (Fig. 2.9) is a chemical compound ($C_{28}H_{31}N_2O_3Cl$) and a dye. It is often used as a tracer dye within water to determine the rate and direction of flow and transport. The dye has a remarkably high photostability, high fluorescence quantum yield (0.95) [128], low cost, and is frequently used as a model compound to study photocatalytic activity in aqueous solutions [121, 127, 128]. Rhodamine 6G has a very high molar absorptivity at 550 nm, which makes the measurement of small concentrations possible by standard UV/VIS spectroscopy. As R6G is photocatalytically decomposed, its absorbance decreases and the rate of decomposition can be determined. The photocatalytic degradation of R6G usually follows first-order kinetics.

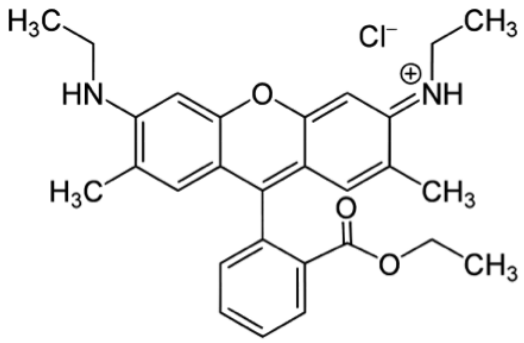

Figure 2.9: Chemical structure of Rhodamine 6G.

Photocatalytic degradation of gas phase compounds has been widely used to evaluate the activities of TiO_2 samples [129, 130, 131, 132, 133]. Typical test compounds include common pollutants such as toluene [129], trichloroethylene [129], formaldehyde [130, 131] and NO_x [132, 133]. Gas chromatography-mass spectroscopy (GC-MS) methods are usually used to follow the kinetics of degradation. By-products and CO_2 generation can also easily be measured, which gives more information on the mechanism. Many factors such as contaminant concentration, relative humidity, O_2 concentration and reactor design have an influence on the rate of photocatalytic oxidation. Gas phase testing of photocatalysts is perhaps best suited for high surface area samples, where TiO_2 is either grown as a film, or impregnated in particulate form on a high surface area support.

2.3.4 Preparation of TiO_2 thin films

TiO_2 thin films can be prepared using virtually all the common liquid and vapour phase deposition methods. Usually all the liquid phase deposition methods produce amorphous TiO_2 and a separate annealing step is required to crystallize the film. Crystalline TiO_2 can more easily be produced directly by vapour phase methods. Photocatalytic thin films deposited on a solid substrate offer a major advantage over powder materials in photocatalytic water purification systems, because the costly filtration step is avoided. On the other hand, the surface area of the photocatalyst should be as high as possible, which is often an advantage of powders over thin films in these systems.

Among liquid based thin film deposition methods, the sol-gel technique is by far the most popular in the preparation of photocatalytic TiO_2 thin films [134, 135, 136, 137,

138, 139, 140]. The sol-gel technique is a versatile method offering many possibilities to tune the properties of the thin film. Dopants and other modifying agents can easily be introduced to the starting sol to change the properties of the final film. Typically titanium salts or alkoxides are used as precursors in a sol-gel process. The precursors are hydrolysed in a controlled manner, thus forming a polymeric network of Ti-O bonds in a solvent. This state is called the sol because it contains colloidal particles in solution. When the solvent evaporates to the extent that a continuous 3D network of solid material forms, the state has turned into a gel. The gel is dried to remove all the solvent and usually also crystallized by annealing at high temperature. Film growth using the sol-gel technique is usually accomplished using either dip-coating or spin-coating. In dip-coating the substrate is simply dipped in the sol and pulled away using a constant speed, during which the sol changes into a gel on the substrate surface through evaporation of the solvent. In spin-coating a small amount of the sol is dropped on the substrate, followed by spinning it at high speed, which removes all the excess sol by centrifugal force. At the same time the solvent evaporates and a uniform gel film forms on the surface. The thickness of the formed film can be controlled by changing the viscosity, concentration and solvent evaporation rate of the sol, or by changing the withdrawal speed in dip-coating or spinning speed in spin-coating.

Several sol-gel recipes for the preparation of high quality photocatalytic TiO_2 thin films have been reported. To control the hydrolysis reaction better Paz et al. used a $Ti(^iOPr)_4$ based sol, where a bidentate acetyl acetonate (acac) ligand was used to shield the titanium [134, 135]. This resulted in a stable sol with a shelf life of at least two months. TiO_2 films prepared from the sol by spin-coating and calcination were highly active in the degradation of stearic acid by 365 nm or 254 nm irradiation. HCl, diethanolamine (DEA), polyethylene glycol (PEG) and diethylene glycol (DEG) are other possible additives which can stabilise $Ti(^iOPr)_4$ based sols and give more control over the hydrolysis reactions [136, 137, 138, 139, 140]. Using PEG as an additive porous photocatalytic TiO_2 films can also be readily obtained [136, 138]. The pores form during the calcination step and their size can be controlled by the concentration of PEG in the sol. This is a convenient way to increase the surface area of the coatings in order to increase their photocatalytic activity.

Low temperature liquid phase preparation routes have been investigated in order to produce crystalline TiO_2 films on heat sensitive materials such as polymers. These include the direct growth of anatase from TiF4 solutions and hydrothermal treatment of amorphous TiO_2, where temperatures close to 100°C are enough to induce crystallization [141, 142, 143, 144].

Gas phase methods generally lead to higher quality thin films than liquid phase methods. Lower impurity contents and higher film densities are usually obtained. Vapour deposited TiO_2 films are often crystalline as-deposited and a separate heat treatment is not required. TiO_2 thin films prepared by the sol-gel technique typically require annealing temperatures around 400-500°C to crystallize, whereas vapour phase techniques can produce crystalline anatase TiO_2 at much lower temperatures, e.g. close to 200°C. Vacuum equipment makes gas phase methods usually significantly more expensive as compared to liquid phase methods.

Pulsed laser ablation (PLD) is a physical vapour deposition (PVD) method. The pulsed laser ablation process is very complex. At a superficial level, ablation might be viewed simply as a rapid boiling of material within a localised interaction volume

at, and close to, the surface of the target. When investigated more deeply, however, the hidden complexity soon becomes apparent. If a solid or liquid is irradiated with an intense laser beam, a small amount of material on the surface is vaporised and ejected away from the sample. This vapour is a collection of atoms, molecules, ions and electrons. The exact ratio and kinetic energy depend on the laser parameters (intensity, wavelength, pulse width) and to some degree on the target sample. If this vapour comes in contact with another surface it may re-condense on the surface. Repeated pulses of laser light, and subsequent repeated vapour plumes, will build up material on the surface to form what is termed a thin film [145].

Evaporation is another physical method used to grow photoactive TiO_2 thin films. In this method the source material is heated, either resistively or with an electron beam, in a high vacuum, which causes it to evaporate. The evaporated material is collected on a substrate, thus forming a thin film. Yang et al. studied the deposition of TiO_2 films by electron beam evaporation (EBE), using a substrate temperature of 250°C [146]. The effect of O_2 partial pressure during deposition was studied and an optimum value was found for the best photoactivity. Only the photoinduced superhydrophilicity of the films was studied, however.

CVD has been used in many studies to prepare photocatalytic TiO_2 thin films [147, 148, 149, 150, 151, 152, 153, 154]. Typically, a decomposition CVD reaction is used where a titanium alkoxide vapour is controllably led over the substrate at a temperature where the titanium precursor molecules decompose, leading to TiO_2 growth [148, 150, 151]. In some cases O_2 is also led to the reactor [153]. Plasma enhanced CVD (PECVD) has been used to deposit photocatalytic TiO_2 thin films using $Ti(^iOPr)_4$ and O_2 plasma [152]. A halide precursor, $TiCl_4$, together with ethyl acetate as the oxygen source can also be used in the CVD of photocatalytic TiO_2 thin films [149, 154]. The films were photocatalytically active in the degradation of stearic acid by UV light and also turned superhydrophilic after irradiation.

Atmospheric pressure chemical vapour deposition (APCVD) is a convenient method for fast coating of large flat surfaces. Because a vacuum is not required, high throughput film deposition can be realized in a production line. APCVD is used in the production of the Pilkington Activ™ self-cleaning glass [155]. The deposition is done at 615°C in the float glass process line, using $TiCl_4$ and ethyl acetate as precursors. In the Pilkington Activ™glass the TiO_2 film thickness is 15 nm and a 30 nm SiO_2 barrier layer is also used to prevent sodium diffusion from the glass to the TiO_2 film. With such a thin TiO_2 layer the photocatalytic activity is quite modest. Thicker TiO_2 layers in window applications are not very practical, because optical interference would lead to disturbing colouring. Besides ethyl acetate H_2O, MeOH, EtOH and ^{i}PrOH have also been studied as oxygen sources in the APCVD of TiO_2 [156]. All oxygen sources produced anatase films at 500-650°C with $TiCl_4$ as the Ti source. All the films exhibited good activity in photocatalytic degradation of stearic acid and showed superhydrophilic properties [156]. Nitrogen doped TiO_2 films have also been prepared from $TiCl_4$, O_2 and NH_3 using APCVD [157].

2.4 Sputter deposition of titanium dioxide

When a solid is bombarded with energetic particles, such as accelerated ions, surface atoms of the solid are partly scattered backward due to collisions between the energetic particles and the surface atoms. This phenomenon is called sputtering, which is extensively used for etching, surface cleaning, thin film deposition, etc.

The basic sputter deposition system is composed of a pair of electrodes. One of the electrodes is the anode and the other the cathode. The front surface of the cathode is covered with the target material to be sputtered. The substrate is placed on the anode. The sputter chamber is filled with the sputter gas, typically Argon. The glow discharge is maintained under the application of a voltage between the electrodes. The Ar^+ ions generated in the glow discharge are accelerated towards the cathode (target). The bombardment of the target by these energetic positive ions causes the removal of target atoms. These target atoms deposit on the substrate and a thin film is formed. In this process, no chemical reaction occurs between the gas and the target atoms. However, if at least one reactive gas (e.g. Oxygen or Nitrogen) is added in the chamber besides Ar, the reactive gas will react with target atoms, forming a compound layer on the substrate. This technique is known as reactive sputtering. If the applied potential between the cathode and anode is constant with time, the process is called DC sputtering, by which highly electrically conductive materials, like metallic targets, can be sputtered. For insulating targets, however, the glow discharge in a DC sputtering system cannot be sustained, because the surface of the target will charge up in order to neutralise the fluxes of positive ions and electrons to the surface, regardless of the potential applied to the electrode backing the insulating target. These ions and electrons then recombine on the surface. In this case, a pulsed-dc voltage is applied to the target, which avoids the charge build up on the targets. This is called pulsed-dc sputtering [158].

The electric field inside a sputtering chamber accelerates electrons, which collide with Ar atoms, producing Ar^+ ions and more electrons and a characteristic purple/blue plasma. Fig. 2.10 shows the colour of a plasma of ICMS during the deposition of TiO_2. The sputtering of the material requires that a plasma be formed. The features of plasmas are extremely complex and it is composed of numerous chemical species. Plasmas are generated by an ionized gas under the influence of an electric field. A system that is out of thermodynamic equilibrium can be considered as the fourth state of matter. It is composed of neutral particles, electrons, ions, free radicals and photons.

At the object surface a number of processes and combinations of them can occur (Fig. 2.11).

In Fig. 2.11(a) the arriving ion (or neutral) is adsorbed onto the surface, and a chemical or physical bonding is created. The incoming species may also transfer some of its momentum to one of the surface atoms, and cause it to move around on the surface (displacement) (Fig. 2.11(b)). If the energy of the incoming ion is sufficiently high, it may start to remove some of the surface atoms (sputtering) as is shown in Fig. 2.11(c), and if the energy is increased even further, the incoming ion can be implanted (Fig. 2.11(d)). In addition, there can also be a number of combinations of these processes.

Adsorption is typically a low energy process, which is dominant around a few tens of eV, or less. Sputtering is initiated when the energy of the incoming atom or ion is

Figure 2.10: Plasma colour during the deposition of TiO_2 by inverted cylindrical magnetron sputtering located at the Department of Electrical and Electronic Engineering at Stellenbosch University.

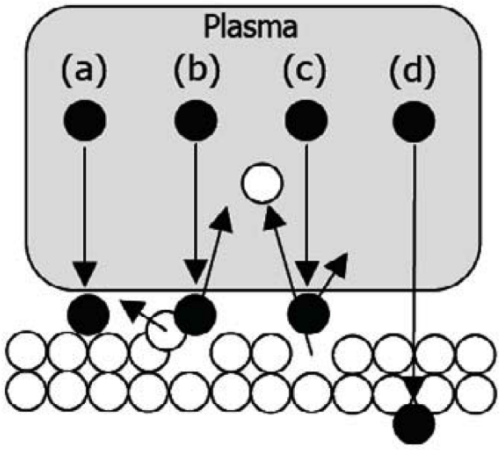

Figure 2.11: Effects of bombarding ions or neutral atoms onto a surface. (a) Adsorption, (b) displacement (momentum transfer), (c) removal of surface atom (sputtering or etching), (d) ion implantation [159].

of the order of 100 eV, while implantation occurs at ∼1 keV [159]. Naturally, there are no distinct borderlines between the different processes, but in reality they overlap each other. Also, these processes are strongly dependent on the chemical and physical properties of the involved atoms and ions.

Sputtering is the process where individual ions are impinging onto a surface. When an ion impact establishes a train of collision events in the target, leading to the ejection of matrix atoms, we speak of sputtering. Sputtering was first reported by W.R. Grove in 1852 [160]. Since sputtering is the result of momentum transfer, it has been aptly likened to "atomic pool", where the ion breaks up the closely packed rack of atoms, scattering some backward, to leave the surface. The principle processes in sputtering are illustrated in Fig. 2.12.

The exact processes occurring at the target surface is depending on the energy of the incoming ion. Three different regimes have been identified, (a) namely single knock-

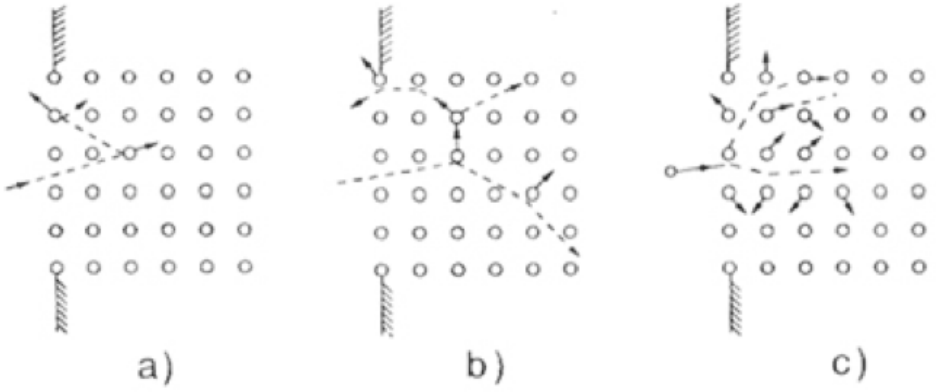

Figure 2.12: The principle of sputtering. Three energy regimes have been identified. (a) Single knock-on (energy), (b) linear cascade, (c) spike (high energy) [161].

on (low energy), (b) linear cascade, and (c) spike (high energy) [161]. The sputtered atoms then become part of the plasma, as neutral atoms or ions (if they are ionized). The sputtered atoms are then available for deposition. Sputtering is typically a high voltage, low current density, discharge (hundreds of volts and tens of mAcm^{-2}).

In magnetron sputtering, the permanent magnets placed behind the cathode produce magnetic fields. The field lines bend to give a component parallel to the target surface. Electrons from the plasma are more confined in this region due to this magnetic field component and are subjected to crossed electric and magnetic fields. As a result, they are forced to move in a cycloidal path. In the region where the confinement of electrons is more effective, the ion population also increases due to the high ionization rate. The ions hit the target gaining high energy and thereby produce sputtered atoms. This region of the target, where heavy erosion takes place, is known as the racetrack.

The resulting film properties can be controlled by adjusting the following sputter parameters:

- The sputter current (I_{SP}) mainly determines mainly the rate of the deposition process and hence the time which remains for the arriving particles during the growth process for either surface diffusion and agglomeration on existing growth centres or nucleation with other atoms.
- The applied voltage or power determines the maximum energy, with which sputtered particles can escape from the target (reduced by the binding energy). Energies of the sputtered particles show a broad distribution with a maximum of the distribution between 1 eV and 10 eV. The applied voltage also determines also the sputter yield, which is the number of sputtered particles per incoming ion.
- The pressure (P) in the sputter chamber determines the mean free path (λ) for the sputtered material, which is proportional to $1/P$. Together with the target substrate distance (T-S), the pressure controls how many collisions occur for the particles on their way from the target to the substrate. This can influence the porosity of the films, . Butbut also the crystallinity and texture can also be

affected [159]. Via the gas mixture, one can control Tthe stoichiometry of the films, which are sputtered from a metallic target, can be controlled via the gas mixture. The oxygen flow $P(O_2)$ is the parameter varied, whereas the desired total pressure is kept constant by regulation of the Ar-flow $P(Ar)$.

- The substrate temperature can have a strong impact on the growth behaviour with respect to crystallinity or density of the samples. During sputtering without external heating, the substrate temperature may rise considerably, especially during the long sputtering times required for the deposition of thick films.
- In principle a bias-voltage can be applied to the substrate, which has the effect of accelerating electrons or ions towards the substrate or keeping them away. Both may have an influence on the layer growth as reported in the literature [162]. Usually the substrate and target surface are parallel to each other. A variation of the deposition angle (i.e. sputtering under oblique incidence) can be achieved by tilting the substrate. Thereby a new preferential direction for the film growth, and potentially anisotropic films, can be produced.

The realization of thin films of TiO_2 and Ag-TiO_2 requires the mastery and control of their synthesis. The choice of the deposition method demands several criteria:

- The nature of the materials to be deposited;
- The rate of the deposition;
- The nature of the substrate to be used;
- The stoichiometry desired;
- The adhesion of the films on the substrate;
- The reproducibility and scalability of the technique;
- The cost effectiveness of the technique.

In this work, the pulsed-dc inverted cylindrical magnetron sputtering (ICMS) technique, also known as hollow cathode sputtering, was chosen for the synthesis of the thin films of TiO_2 and Ag-TiO_2 nanocomposite. This novel deposition technique presents great promises over other vapour deposition techniques. A complete description and comparison with other vapour deposition techniques are presented in the section on ICMS.

2.5 Conclusion

Based on the literature review undertaken, two approaches were chosen:

- Approach one
  - TiO_2 surface modified track-etched membranes using inverted cylindrical magnetron sputtering.
- Approach two

- ◇ Ag-TiO_2 surface modified track-etched membranes using thermal evaporation in conjunction with inverted cylindrical magnetron sputtering.

The reasons why the track-etched membrane model was chosen for the development of photocatalytic membranes for water treatment processes are:

- It is a good model with a well-defined structure;
- It is easy to explain the results of TiO_2 enhancement using Plasmon metals;
- It is possible to study p-n-junction behaviour of semiconductor layers using Hall measurements;
- TMs are optically transparent and allow for direct bandgap measurements.

12μm-thick Polyethylenetherephthalate (PET) foils will be irradiated with energetic ions at the heavy ion accelerator in Dubna (Russia) up to fluences of 107 cm^{-2} and etched to produce 0.1-0.4 μm tracks.

The workplan will entail the development of hybrid membrane photocatalytic reactor technologies, based on nanostructured semiconductors and track-etched membranes for water treatment processes:

- To modify existing sputtering infrastructure for TiO_2 deposition;
- To develop cooling system to allow for sputtering on polymeric TM surfaces;
- To modify the existing thermal evaporation unit for Ag deposition on polymeric TM surfaces;
- To develop a method of sample pre-treatment.

A process methodology for characterising the surface modification of TiO_2 and Ag-TiO_2 TM is to be developed, using:

- Standard techniques (SEM, AFM, XRD);
- Nuclear physics techniques (PIXE, RBS);
- Optical properties (Transmission UV-VIS: bandgap, Dye degradation).

The ultimate aims of the research is:

- The development of a prototype setup for Multifunctional Track-etched Membrane Hybrid water treatment processes;
- The development of a "Low- fouling" membrane with a "self-cleaning" surface;
- The development of TMs with "superhydrophilic" surfaces for permeability enhancement;
- The development of anti-microbial TMs;
- The ability for further modification by water soluble silanes.

Chapter 3

Materials and methods

This chapter gives a brief overview of the materials used and a general methodology of the experimental procedures followed in this study. It aims to explain the different techniques employed throughout the various stages of this work in order to characterise the structural, morphological and optical properties of the synthesised films surfaces.

3.1 Development of setup for metal and metal oxide layers deposition on the track-etched membrane

3.1.1 Inverted cylindrical magnetron sputter (ICMS) for TiO_2 deposition

3.1.1.1 Description

Cylindrical magnetron sputtering, described in a series of patents by Penfold and Thornton, issued in the mid-TiO_2, were among the first magnetrons [163, 164], and has long been used to coat materials at high rates onto complex shapes, such as those used in the aerospace, biomedical, and machine tool industries.

Sputter deposition allows for the production of stoichiometric films over a large area. In a sputter deposition process, the target atoms are physically ejected by the bombardment of energetic particles, such as accelerated gas ions. The sputtered atoms travel through the plasma and undergo multiple collisions with the plasma species and subsequently deposit on a substrate. There are many advantages for using sputtering, such as surface smoothness, thickness control, good adhesion, deposition of films with nearly bulk-like properties and excellent film uniformity with high deposition rates.

The growth of epitaxial thin films by sputtering depends on many deposition conditions, including the total gas pressure, O_2:Ar gas pressure ratio, substrate temperature, deposition rate, sputter power, and the substrate-to-target distance [165, 166].

The sputtering process can either employ direct current (DC), pulsed DC or radio frequency (RF) power, depending on the electrical conductivity of the target. DC power can only be used for conducting targets, while pulsed DC and RF power can be used for both conducting and insulating targets. A magnetron sputtering process

uses a magnetron source, where a magnetic field is employed to enhance the sputter efficiency.

After analysing both planar and off-axis sputter deposition, it was concluded that the off-axis deposition favoured TiO_2 epitaxial growth [167]. Other advantages are that the film shows excellent film uniformity with good adhesion and has bulk-like properties. The alternative planar system, is an on-axis method that causes re-sputtering of the deposited layer, which the off-axis deposition does not do. This chapter will focus on the design and construction of a simple Pulsed DC Inverted Cylindrical Magnetron.

3.1.1.2 ICMS features and modifications

The ICM head, as illustrated in Fig. 3.1, is mounted in a double cross-piece vacuum chamber on a standard DN 100 CF flange with a mounting depth of 120 mm. The ring magnets and cylindrical target assembly are attached to a water cooled backing plate that limits heat build-up in the target and magnets. The substrate holder is situated 5cm from the sputtering head. The temperature of the substrate cooling device is controlled by a Peltier cooler connected to an external power source. Thermal contact between the cooler and the substrates was achieved by clamping the substrate in the cooler and allowing the temperature to reach equilibrium before starting deposition.

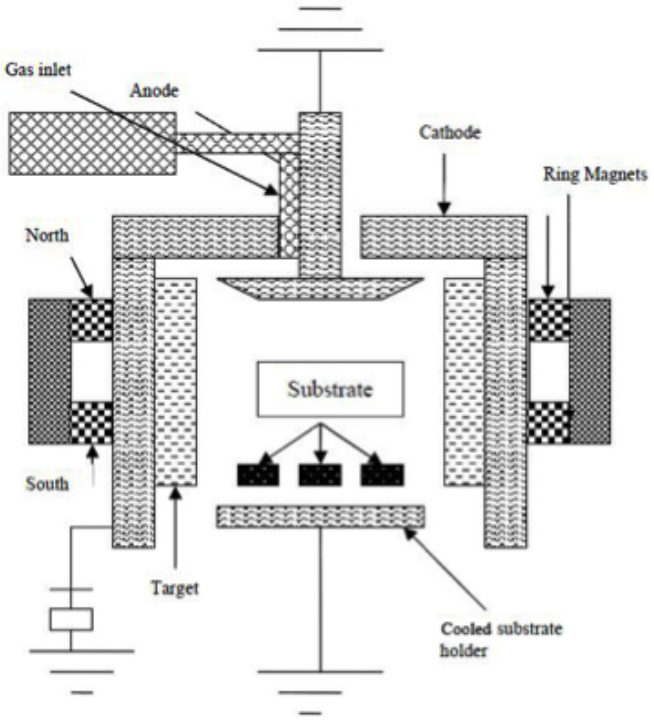

Figure 3.1: Schematic illustration of the Inverted Cylindrical Magnetron (ICM) sputter gun [168].

The vacuum chamber design entails consideration of various stages of the sputter process. The base pressure achieved before the sputter process commences and the actual sputter pressure are the two main aspects to be considered. Since the base

pressure is near 10^{-4} mbar and the working pressure at 66 mbar, there should be a bypass valve to isolate the turbo molecular pump from the deposition chamber during the actual sputter process. The use of a turbo molecular pump instead of a diffusion pump has definite advantages in terms of having potentially less carbon contamination arising from the heated oil.

The vacuum chamber is evacuated by a diffusion pump backed by a rotary pump. The vacuum system is separated from the deposition section by a gate valve. This allows for differential pumping on the upper and lower chambers, thus enabling the use of high gas pressures needed during the sputtering process, without causing damage to the diffusion pump. High purity Argon and mixture Oxygen gases are fed into the gun positioning and the vacuum components.

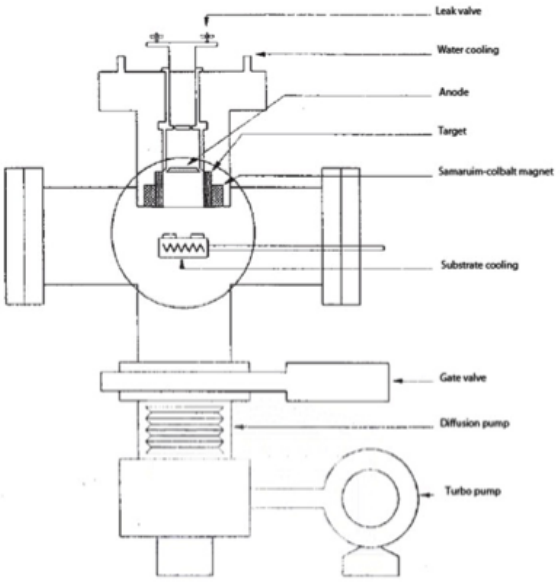

Figure 3.2: Schematic illustration of the sputter deposition system showing the ICMS.

A custom built pulsed-dc power supply is used as the power supply for the ICM. The output voltage and current capabilities of these generators are limited. The plasma impedance normally requires that a matching network is connected to the cathode to transform the cathode impedance to the power needed by the generator. When an alternating signal is applied to the cathode, a plasma is generated that acts as a rectifier, generating an average negative voltage at the smaller of the electrodes, which is generally the target. This negative voltage is called the self-bias or VDC voltage.

The next consideration is to select the diameter and type of target, so that the deposition thickness is uniform over the entire substrate. Previous literature [167] shows that an off-axis type of sputter process is ideal for stoichiometric film growth. Fig. 3.3 shows the erosion of the target at the highest magnetic field density point.

A cylindrical target with a diameter of 50.8 mm, a height of 25.4 mm and a thickness of 5 mm was chosen, as this diameter is a standard size, and will deposit a very uniform layer over a 25 mm $\times$ 25 mm substrate. There are various overseas target suppliers and targets of these dimensions are often stock items. The substrate size was chosen to be used as a standard size on all processes.

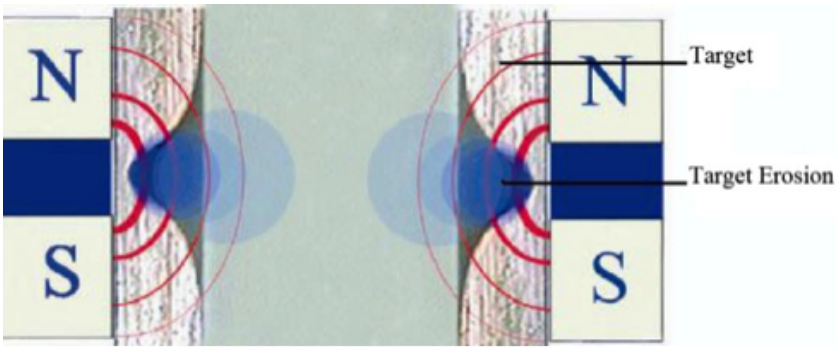

Figure 3.3: Cylindrical target displaying magnetic poles and ion confinement and target erosion.

Ideally the magnets should be custom made washer type magnets that have the North and South Pole on either side. The magnets are positioned in the same direction on top of each other with a spacer inbetween. These magnets are housed around the target and can be repositioned, so that the target erosion can be shifted up or down, in order to extend the target's lifetime.

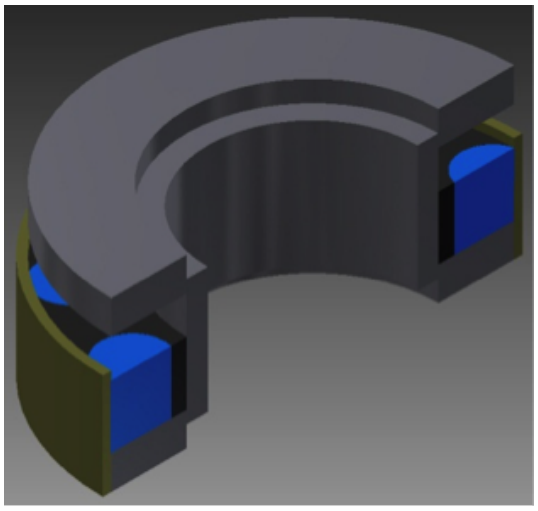

Figure 3.4: Rare earth button magnets are mounted between two mild steel rings in a copper cooling flange.

Samarium-cobalt magnets were chosen for their high temperature tolerance of around 300°C before degradation. Copper was used as contact material between the target, magnets and water cooling. Standard button magnets were used, which were stacked between mild steel rings, as shown in Fig. 3.4. This method is very cost effective and flexible, and allows for efficient cooling, as the button magnets fit into a copper flange. The copper flange also fits tightly against the target. The whole assembly is surrounded by a copper cooling pipe that fits into the outer perimeter of the copper flange. The target, copper flange and Sm_2Co_{17} button magnets are all on the same potential and are insulated from the outer housing in a vacuum tight containment.

The water-cooling method is dependent on power dissipation. The energy typically needed for the TiO_2 thin film layers was in the region of 370 mA at 385 V, which gives

an average power of 125 W. The system has been successfully tested at a maximum of 500 W. The target, being the cathode, is electrically isolated from the outer anode body of the ICM which, in turn, is earthed.

Figure 3.5: The water-cooling pipes are insulated from the outer housing and vacuum tight.

The target, magnets, copper cooling piping and copper cooling body are also vacuum sealed. For safety purposes the cathode must be electrically shielded. A copper cooling pipe is used to cool the whole cathode assembly. A copper pipe is used in a closed loop construction to prevent water leaks, as seen in Fig. 3.5.

In order to deposit on a polymeric support, it is imperative for the substrate to be cooled at all times during deposition. Otherwise, due to the prolonged high heat exposure, the TM would melt. By expanding on the water-cooling system, it was possible to build a cooling stand inside the sputter chamber. Mounting the sample holder on top of that then could act as a heat sink for the Peltier inside the holder (Fig. 3.6). This configuration enabled the Peltier-cooled sample holder to maintain the TM surface temperature at 30°C during deposition.

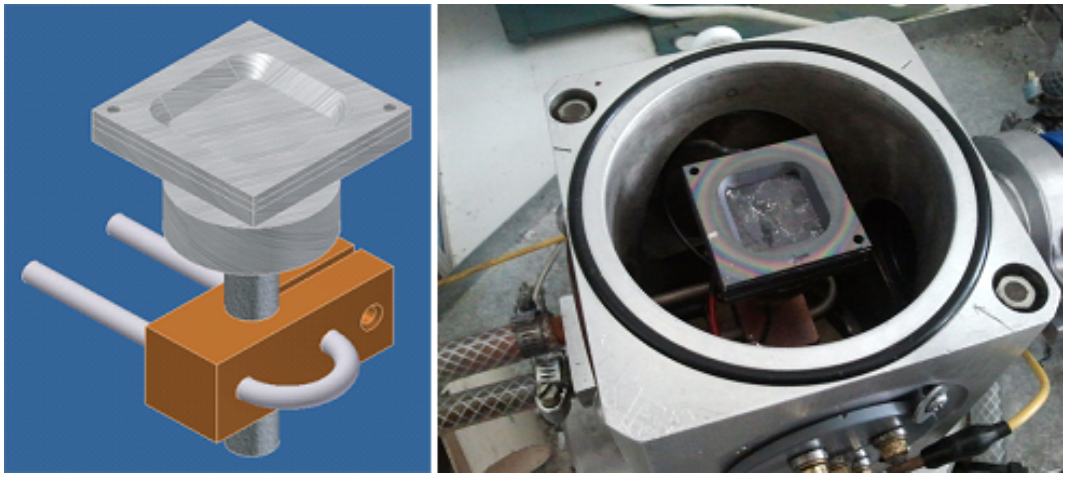

Figure 3.6: Cooling stand and sample holder. (a) Design, and (b) the actual installation.

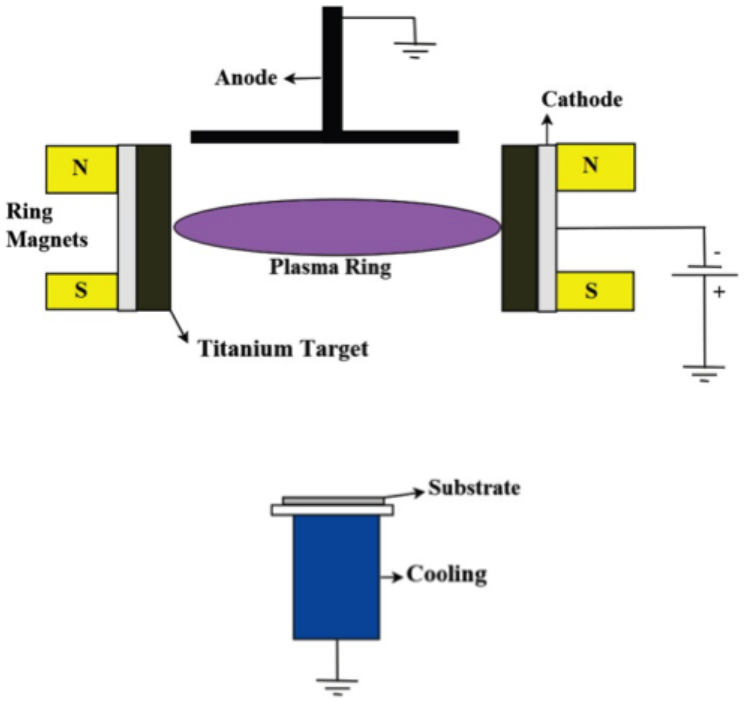

Figure 3.7: Schematic diagram of an Inverted Cylindrical Magnetron (ICM) sputtering system.

The operation of a DC magnetron sputtering process is based on the creation of a plasma discharge in the vicinity of a target, and the acceleration of the ions from the plasma to the target surface, to sputter the desired materials. The cathode, to which the target material is attached, is held at a large negative voltage relative to the substrate and walls of the chamber. Positively charged argon ions will accelerate towards the cathode, dislodging atoms from the target, leading to the build-up of a thin film on the substrate. The Argon plasma is ignited in the chamber by field emission of electrons from the cathode. The target is made from Titanium.

The secondary electrons in the plasma discharge, which are emitted from the cathode due to ion-bombardment, show cycloidal motion perpendicular to both the electrical field E (normal to the surface) and the magnetic field (B). The centre of the orbit drifts in the direction of $E \times B$. The magnetic field is oriented such that these drift paths for electrons form closed loops parallel to the cathode surface [169]. These secondary electrons lose their kinetic energy due to collisions with gas atoms (ionisation), and the net result is an extremely dense plasma in this drift ring at the cathode, which effectively increases the sputtering rate at the target surface.

The re-sputtering of the grown film by negative ions and reflected neutrals is a major problem that is encountered in the sputtering of oxide materials. It leads to morphological changes, such as ripples, pits and cones on film surfaces. The ICM configuration can significantly minimise this undesired effect.

3.1.1.3 Calibration

There was no real-time monitoring system available for calculating the sputter or deposition rate of TiO_2, thus a calibration curve had to be constructed. This was achieved by depositing TiO_2 on silicon wafers with a section enclosed with Rubylith™. After deposition on various samples in 5 min increments, and peeling off the Rubylith™, the resulting step-edge could be measure by AFM and plotted. From the resulting graph (Fig. 3.8) the average deposition rate of TiO_2 could be determined to be around 1 nm/min.

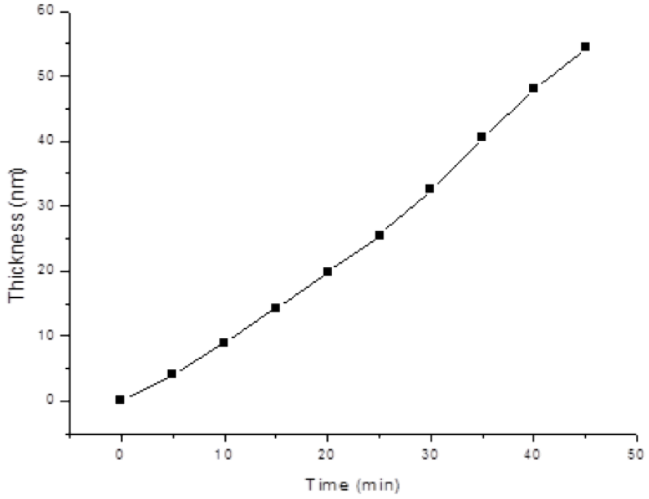

Figure 3.8: Measured TiO_2 deposition rate curve, showing an approximate rate of 1 nm/min on Ag-Si.

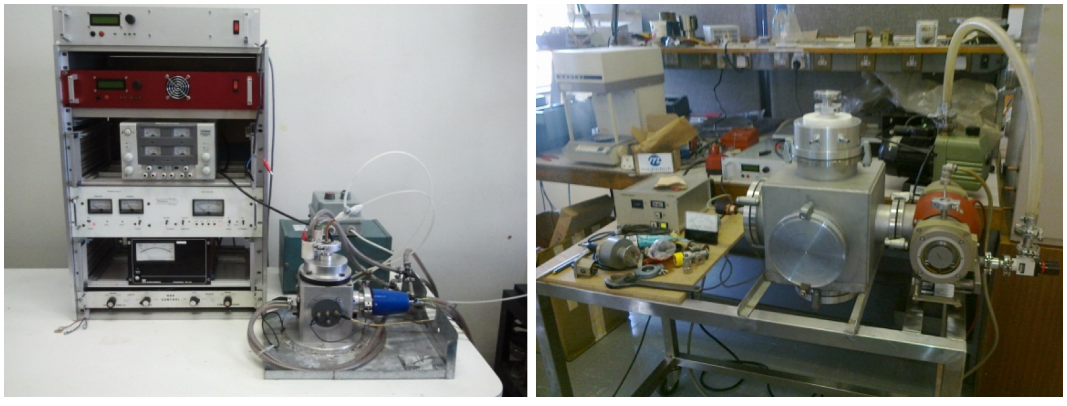

Figure 3.9: Current ICM system (left) and new ICM system nearing completion (right).

The reactive sputtering process is a widely used coating technique for the production of oxides, nitrides, carbides and nanocomposites. The main drawbacks of this process are the hysteresis behaviour, which seriously limit the stability, the poisoning of the

sputtering target, which substantially reduces the sputter erosion rate, the stability control and arcing effect. Considerable efforts have been devoted to eliminate these drawbacks, such as:

i) Increasing the pumping speed, which requires larger additional costs;

ii) Increasing the target-to-substrate distance, which requires larger chambers (hence, higher costs);

iii) Plasma emission monitoring;

iv) Pulsed reactive gas flow, which requires an amount of optimisation and a continuous monitoring and adjustment of the process;

v) Dual magnetrons or magnetron with a full target erosion;

vi) Substoichiometric ceramic target;

vii) Voltage control [170, 171].

Planar reactive magnetron sputtering suffers most of these undesirable phenomena. Planar sputtering also suffers from being a line-of-sight process and is not well suited for coating non-planar substrates. Inverted cylindrical magnetron sputtering (ICMS), also known as hollow cathode sputtering, is used to sputter from the inner surface of cylindrical targets and produce highly conformal coatings [164]. Due to its enclosed geometry, it also produces an intense and very uniform plasma next to the target surface, that results in high deposition rates [172]. Hollow cathodes also lead to excellent target erosion, because the sputtered atoms that are not deposited on the substrate get re-deposited on the cathode. An additional advantage of hollow cathodes is their lower target cost and the production of large area uniform films [173, 174].

Some technological issues have recently been addressed on hollow cathode sputtering. Lindberg et al. [175] reported the hysteresis behaviour in the target voltage while depositing Al-O films. They used a hollow cathode magnetron with low frequency AC power. Such a setup resembles dual target magnetron sputtering, rather than a hollow cathode source. Pradhan et al. [176] reported that the hollow cathode does not exhibit the hysteresis behaviour generally observed in planar reactive sputtering systems, and is stable at all operating points without any feedback control. They explained the absence of the hysteresis behaviour on the basis of the enclosed geometry, which significantly reduces the sputtered flux leaving the hollow cathode. These properties strongly indicate that hollow cathode sputtering has sufficient possibilities to prepare a "smart" class of nanocomposite films with a wide range of technological applications.

3.1.1.4 Parameters

The resulting film properties can be controlled by adjusting the following sputter parameters:

- The sputter current I_{SP} mainly determines the rate of the deposition process and hence the time which remains for the arriving particles during the growth process for either surface diffusion and agglomeration on existing growth centres or nucleation with other atoms.

TiO_2 deposition parameters	To start system	To run system
Voltage (NB start)	650 V (min)	385 V
Power (NB running)	135 W	125 W
Current	0.5 A	0.325 A
Gas cylinder Ar/O_2	350 kPa	350 kPa
Gas Ar	40 mmHg	40 mmHg
Gas O_2	0 mmHg	10 mmHg
Time	0 min	45 min
Frequency	21 kHz	21 kHz
Duty cycle	80%	80%
Substrate-to-target distance	50 mm	50 mm
Substrate temperature	17°C	30°C

Table 3.1: Titanium dioxide (TiO_2) deposition parameters using ICMS

- The applied voltage or power determines the maximum energy with which sputtered particles can escape from the target (reduced by the binding energy). Energies of the sputtered particles show a broad distribution with a maximum of the distribution between 1 eV and 10 eV. The applied voltage also determines the sputter yield, which is the number of sputtered particles per incoming ion.
- The pressure (P) in the sputter chamber determines the mean free path (R) for the sputtered material, which is proportional to $1/P$. Together with the target substrate distance ($T - S$), the pressure controls how many collisions occur for the particles on their way from the target to the substrate. This can influence the porosity of the films. The crystallinity and texture can also be affected [159]. The stoichiometry of the films, which are sputtered from a metallic target, can be controlled by the gas mixture. The parameter that is varied is the oxygen flow $P(O_2)$, whereas the desired total pressure is kept constant by regulation of the Ar-flow $P(Ar)$.
- The substrate temperature can have a strong impact on the growth behaviour with respect to the density or crystallinity of the samples. During sputtering without external heating the substrate temperature may rise considerably, especially the during long sputtering times required for the deposition of thick films.
- In principle a bias-voltage can be applied to the substrate, which has the effect of accelerating electrons or ions towards the substrate, or keeping them away. Both may have an influence on the layer growth as reported in the literature [162]. Usually the substrate and target surface are parallel to each other. A variation of the deposition angle (i.e. sputtering under oblique incidence) can be achieved by tilting the substrate. Thereby a new preferential direction for the film growth and potentially anisotropic films can be produced.

Table 3.1 lists the various parameters needed to start and run the sputter deposition process.

	Conventional PVD method	New method
Coating method	Co-sputtering, RF, DC or AC planar magnetron sputtering, Pulsed laser ablation, and other methods	Pulsed-DC Inverted Cylindrical Magnetron Sputtering (ICMS)
Coating complex shapes	Difficult	Easy
Geometry and high sputtering pressure	Do not eliminate the adverse effects of negative ion bombardment of the growing film (back sputtering)	Eliminate back sputtering
Target cost	High	Lower
Target utilization	Good	Very good
Coating efficiency	Low	Quite high
Coating flux	Anisotropic	Isotropic
Average deposition rate	High	Very high
Range of distribution of metal nanoparticles	Good	Very good
Reproducibility and scalability	Good	Very good
Thickness of nanocomposite films	Thin film	Thin- and thick film

Table 3.2: A comparison of conventional methods and the new ICMS method

3.1.1.5 Comparison of conventional methods and new method ICMS

The main limitations of conventional methods are illustrated in the table below. These properties strongly indicate that ICMS has sufficient possibilities to prepare new nanocomposite systems with a wide range of practical applications. ICMS is a promising candidate to prepare new nanocomposite films with homogeneous coatings on complex shapes which are required for a variety of applications, ranging from X-ray telescope mirrors to biomedical implants.

Table 3.2 shows a comparison of conventional methods and the new ICMS method.

3.1.2 Thermal evaporator for silver deposition

Resistive thermal evaporation is one of the most commonly used metal deposition techniques. It consists of vaporising a solid material by heating it to sufficiently high temperatures and re-condensing it onto a cooler substrate to form a thin film. As the name implies, the heating is carried out by passing a large current through a filament container (usually in the shape of a crucible, boat or basket) which has a finite electrical resistance. The choice of this filament material is dictated by the evaporation temperature and its inertness to alloying and chemical reaction with the

evaporant. This technique is also known as "indirect" thermal evaporation, since a supporting material is used to hold the evaporant.

Once the metal is evaporated, its vapour undergoes collisions with the surrounding gas molecules inside the evaporation chamber. As a result a fraction is scattered within a given distance during their transfer through the ambient gas. The mean free path for air at 25°C is approximately 45 and 4500 cm at pressures of 10^{-4} and 10^{-6} torr respectively. Therefore, pressures lower than 10^{-5} torr are necessary to ensure a linear path for most of the evaporated species and for substrate-to-source distances of approximately 10 to 50 cm in a vacuum chamber. A good vacuum is also a prerequisite for producing contamination free deposits [177, 178].

3.1.2.1 Description

Stellenbosch University's RIBER thin film coating system was used for the thermal deposition of all the metals referred to in this work. A schematic diagram of the system is shown in Figure 3.10. This system is fitted with an acoustic crystal monitor for controlling the amount of metal deposit.

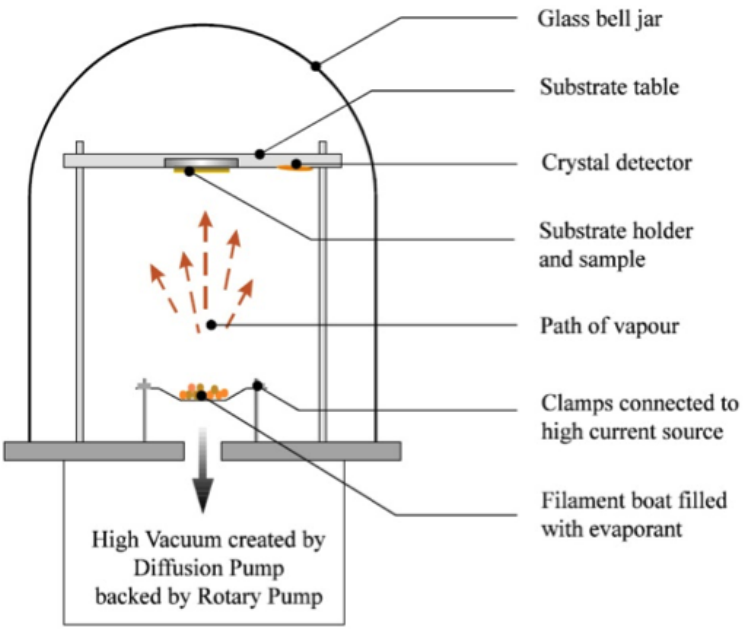

Figure 3.10: Schematic diagram of a resistive thermal evaporator system.

Because there is a lateral distance between the crystal detector used for in-situ monitoring of the deposited films and the substrate, it is necessary to determine the ratio of the respective amounts of deposit between these two surfaces. This ratio is known as the "tooling factor" and is a unique quantity for a particular evaporator, which depends on a number of factors, including the dimensions of the system and the actual evaporant. Table 3.3 lists the experimentally determined tooling factors for the metals used in this work.

All filament boats used consisted of tungsten material and unless otherwise stated, prior to commencing each evaporation, the base pressure was better than 2×10^{-6} torr.

Element	Melting point (°C)	Density (g/cm^3)	Z (Acoustic impedance)	Tooling factor	Current (A)
Silver (Ag)	961	10.49	16.69	1.61	44
Titanium (Ti)	1675	4.5	14.06	1.42	75

Table 3.3: List of metals used in the fabrication of devices in this study and their properties relevant for resistive thermal evaporation. The ambient pressure is below 2×10^{-6} torr

Typical values for the minimum current required to evaporate each of these metals are also listed in Table 3.3.

A material placed in the crucible sublimates and deposits on the waiting sample. Before depositing a new material, a crucible must first be prepared. This entails cleaning it with acetone and then annealing it in the thermal evaporator.

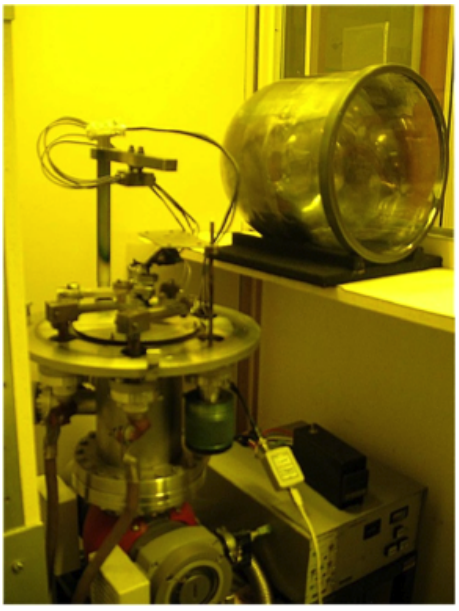

Figure 3.11: RIBER thermal evaporator used at Stellenbosch at the Faculty of Engineering.

The annealing process requires the crucible to be placed into the thermal evaporation unit without material in it (Fig. 3.12). The unit is then sealed, as for a normal deposition, and then turned up to maximum current. This burns the crucible clean and expunges any latent gas in the crucible. A crucible being annealed in a dark room can be seen in Figure 3.13.

Once the crucible is annealed, it is loaded with a suitable material and a sensor is placed in the Quartz Crystal Microbalance (QCM). The sample is also placed in the thermal evaporator. The glass dome is put in place and the vacuum is allowed to reach 2×10^{-6} torr. The current is then slowly increased until the required deposition temperature is reached.

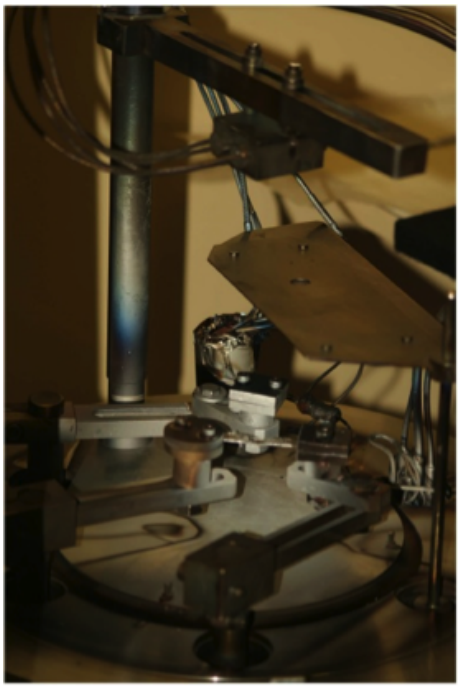

Figure 3.12: Thermal evaporation unit crucible.

Figure 3.13: Thermal evaporation unit during annealing process.

No vacuum is perfect and therefore the heat caused by the evaporating metal particles does affect the substrate. When depositing only a few nanometres and working with a membrane only a few micrometres thick, a good heat sink goes a long way. Taking this into account and trying to avoid thermal shock, the first sample holder designed contained a Peltier cooler and was made interchangeable between the thermal evaporator and the inverted magnetron sputtering unit to optimise deposition and reduce contamination (Fig 3.14).

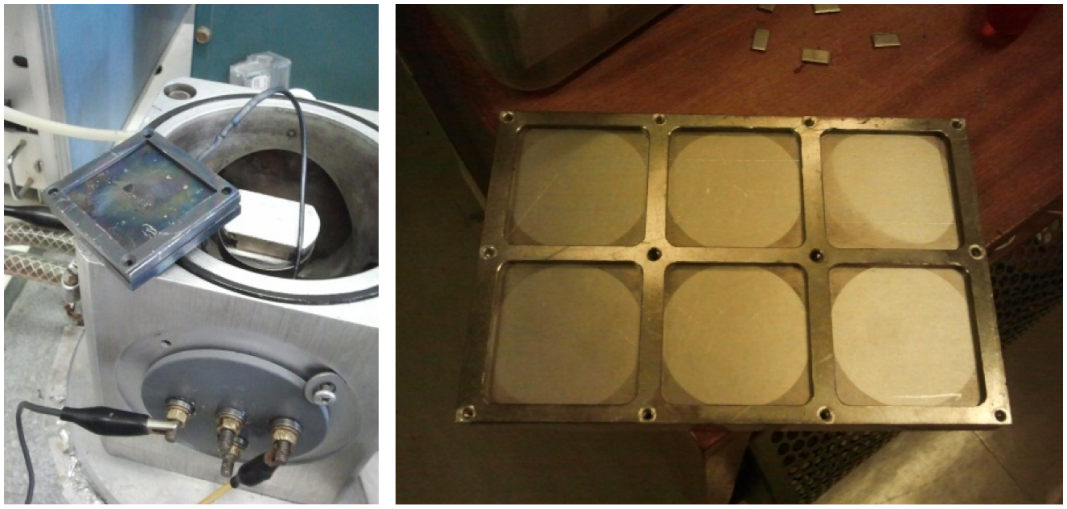

Figure 3.14: Interchangeable Peltier cooled sample holder (left), and six-sample holder (right).

Thereafter, it was decided that it would be more efficient to do the thermal evaporation part in bulk, as a lot of silver goes to waste in the process. A large solid aluminium sample holder was thus constructed to house 6 samples simultaneously, which could also act as a heat sink at the same time (Fig 3.14).

3.1.2.2 Calibration

The QCM is used to control the deposition rate and thickness of the deposited material. Having completed this phase, the current is turned down and the vacuum is vented. This completes the deposition process. It should be noted that the sensor needs to be calibrated for the first deposition and again for every 10% loss of sensor life. For even more accurate depositions a calibration sample can be placed in the unit, along with every deposition, for continuous calibration. Slow heating and cooling of the crucible is important, since heating it too quickly can destroy the crucible. This should be avoided due to material loss and the waste of the 2 hours required for a deposition.

The components of the QCM are shown in Fig. 3.15. For the accurate operation of the QCM the Z-factor, tooling factor and the density of the material to be deposited must be known.

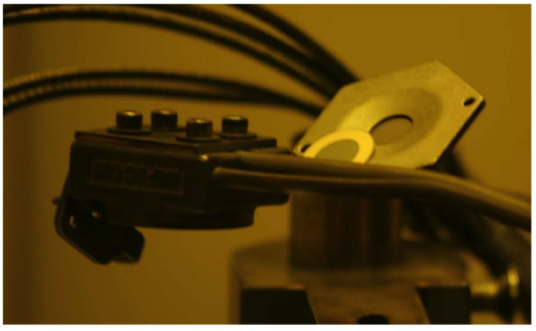

Figure 3.15: QCM sensor and housing.

The Z-factor is the ratio between the acoustic impedance of quartz and the deposition material. Acoustic impedance is a measure of how quickly sound travels through a material. The Z-factor is defined as

$$Z - \text{factor} = \frac{\text{Acoustic impedance of quartz}}{\text{Acoustic impedance of material}}. \tag{3.1.1}$$

The tooling factor is a parameter that correlates the position of the sensor to that of the sample. Different positions in the thermal evaporator result in different degrees of deposition. By compensating for the positional difference, a thickness reading is received relative to the QCM sensor. This means that, when the configuration of the unit is changed, the tooling factor needs to be re-calibrated.

The calibration is done by depositing a sample and then measuring a step height on the sample with the Atomic Force Microscope (AFM). From these 2 readings the tooling factor is then modified according to

$$\text{Tooling factor} = \frac{\text{Thickness AFM}}{\text{Thickness QCM}} \times \text{Old tooling factor}. \tag{3.1.2}$$

By modifying the sample holder within the glass dome one can further optimise the sample position, size, deposition rate and overall efficiency of the process. Initially there was no sample holder to support track-etched membranes inside the thermal evaporator (see previous section, Fig. 3.14).

3.1.3 Cold plasma gun for TM pretreatment

A big hindrance to physically handling small sections of track-etched membranes in the laboratory is their predisposition for static electricity. They literally have an affinity for every surface they come in contact with. Secondly, before depositing anything on the substrate surface, it first needs to be cleaned and sterilised.

Initially a combination of acetone, ethanol, deionised water and a lot of patience was standard practice. In the course of time, the idea of using cold plasma as a pre-treatment was conceived. A cold plasma gun was developed as a temporary TM de-static-tiser, which also inactivates contaminating microbes and removes dust particles (see Fig. 3.16).

Contact angle before 72°
Contact angle after 5 minutes 56°

Argon gas was used for the plasma formation. After cold plasma treatment the membranes were clean and no longer had any residual static charge, making them easily manageable during the consecutive steps.

See Appendix D for CAD drawings.

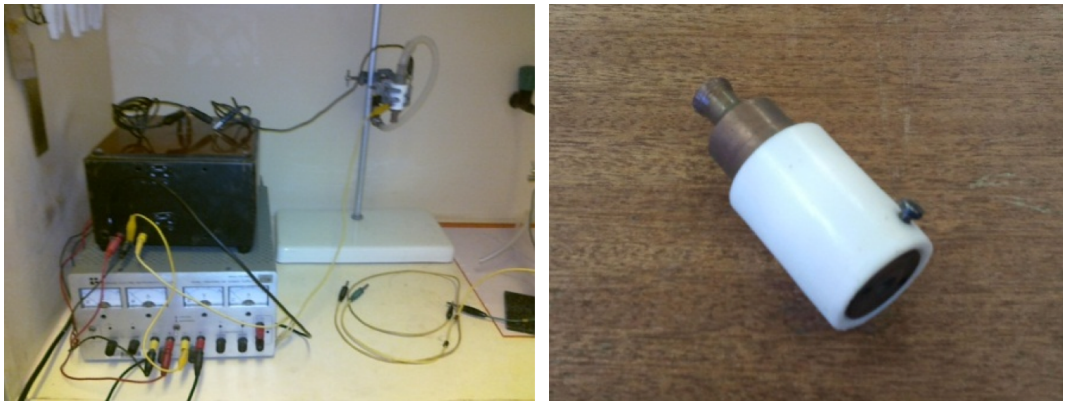

Figure 3.16: Installation (left) and plasma gun (right).

3.2 Methods for surface analyses of composite track-etched membranes

3.2.1 General methods used for composite track-etched membrane characterisation

3.2.1.1 Scanning Electron Microscopy

In light microscopy, a sample is viewed through a series of lenses that magnify the visible-light image. However, the scanning electron microscope (SEM) does not actually view a true image of the specimen, but rather produces an electronic map of the surface of the sample that is displayed on a LCD monitor. Fig. 3.17 below shows a generic SEM schematic.

Electrons from a filament in an electron gun are beamed at the specimen in a vacuum chamber. The beam forms a line that continuously sweeps across the specimen at high speed. This beam irradiates the sample, which in turn produces a signal in the form of either x-ray fluorescence, secondary or backscattered electrons. SEM usually images conductive or semi-conductive materials. The sample examined by SEM must be able to withstand the strong electric currents produced by the electron beam. Samples that do not conduct electricity can be damaged by the charges that can build up. Non-conductive samples must first be coated with a thin layer of conductive material. This coating is accomplished using sputtering equipment. However, this process may damage delicate samples. It should also be mentioned that the specimen might be damaged by the electron-beam focussed for a long time on a small spot. The Phenom bench-top Scanning Electron Microscope (SEM) unit used in the Faculty of Engineering is shown in Fig. 3.18.

3.2.1.2 Atomic Force Microscopy

Atomic Force Microscopy (AFM) provides a number of advantages over conventional microscopy techniques. AFMs probe the sample and make measurements in three dimensions, x, y, and z (normal to the sample surface), thus enabling the presentation of three-dimensional images of a sample surface. This provides a great advantage over any microscope available previously. With good samples (clean, with no excessively large

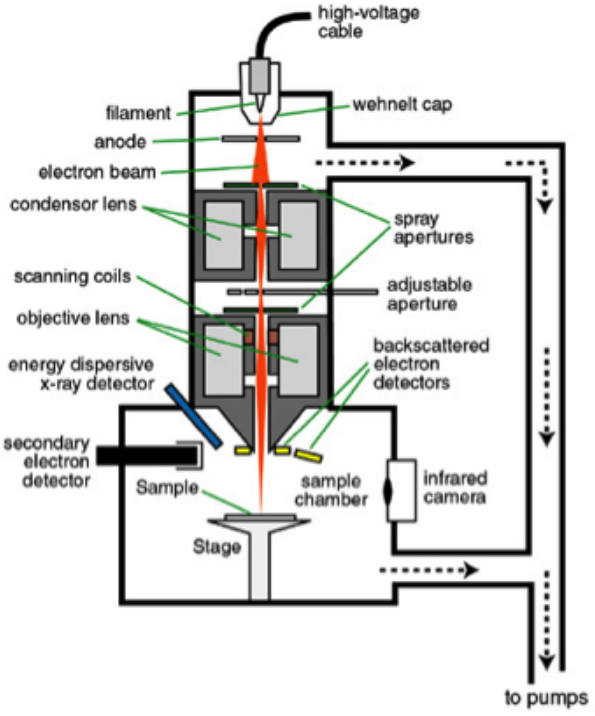

Figure 3.17: Generic SEM schematic.

Figure 3.18: Phenom bench-top Scanning Electron Microscope (SEM).

surface features), resolution in the $x-y$ plane ranges from 0.1 to 1.0 nm, and 0.01 nm in the z-direction (atomic resolution). AFMs require neither a vacuum environment nor any special sample preparation, and they can be used in either an ambient or liquid environment. With these advantages the AFM has significantly impacted the fields of material science, chemistry, biology, physics, and the specialized field of semiconductors. AFMs operate in three different modes, namely Contact-mode; Tapping-mode and Lift-mode. Contact-mode is one of the more widely used scanning probe modes, and operates by rastering a sharp tip (made either of silicon or Si_3N_4, attached to a low spring constant cantilever) across the sample. An extremely low force ($\sim 10^{-9}$ N, interatomic force range) is maintained on the cantilever, thereby pushing the tip against the sample as it rasters. Either the repulsive force between the tip and sample, or the

actual tip deflection, is recorded relative to spatial variation and then converted into an analogue image of the sample surface. The AFM tip is first (manually) brought close to the sample surface, and then the scanner makes a final adjustment in tip-sample distance, based on a setpoint determined by the user. The tip, now in contact with the sample surface through any adsorbed gas layer, is then scanned across the sample under the action of a piezoelectric actuator, either by moving the sample or the tip relative to the other. A laser beam, aimed at the back of the cantilever-tip assembly, reflects off the cantilever surface to a split photodiode, which detects the small cantilever deflections. A feedback loop maintains constant tip-sample separation by moving the scanner in the z-direction to maintain the setpoint deflection. Without this feedback loop, the tip would "crash" into a sample with even small topographic features (although this phenomenon can happen even with careful AFM operation). By maintaining a constant tip-sample separation and using Hooke's Law ($F = -kx$, where F is force, k is the spring constant, and x is the cantilever deflection), the force between the tip and the sample is calculated. Finally, the distance that the scanner moves in the z-direction is stored in the computer, relative to spatial variation in the $x - y$ plane, to generate the topographic image of the sample surface.

Recent advances in the development of AFM technology have led to a number of useful imaging modes, including Tapping-mode and Lift-mode AFM. Although operating in the contact mode has proven successful, it suffers from a number of drawbacks that limit its use on a number of sample types. Firstly, the constant downward force on the tip often damages (and thus changes) many softer surfaces (polymers and biological samples) and even some hard surfaces such as silicon. Also, many samples, such as small particles or biological samples like DNA and cells must be placed on a substrate for imaging purposes. In contact mode, the sample is often destroyed or even pushed out of the field of view by the rastering tip. These complications have been addressed through the development of Tapping-mode AFM. In Tapping-mode, the AFM tip-cantilever assembly oscillates at the sample surface, while the tip is scanned the tip thus lightly taps the sample surface while rastering and only touches the sample at the bottom of each oscillation. This prevents damage to soft samples and avoids the "pushing" around of samples on the substrate.

By using a constant oscillation amplitude, a constant tip-sample distance is maintained until the scan is complete. Tapping-mode AFM can be performed on both wet and dry sample surfaces. Lift-mode AFM provides the operator with a tool to record dual information about a sample surface at one location, such as topography and magnetic gradients (obtained in the magnetic force microscopy or MFM mode), thereby allowing the useful association of the two images. The AFM images presented in this work were acquired by Tapping-mode at the SAND research group of Stellenbosch University. Lift-mode AFM operates by first scanning a line on the sample surface in Tapping-mode to obtain the topographical information. Then, the tip is lifted to a distance above the sample, set by the operator, and the same line is retraced in non-contact mode to obtain (for example) near surface magnetic field information. The process is repeated until the scan is complete, and both images are saved. To perform MFM, a ferromagnetic tip and a ferromagnetic or paramagnetic sample are required. Lift-mode AFM can also be used to record topography and electric fields or phase imaging data. The continuing development of AFM technology provides scientists with a powerful tool to characterize a variety of sample surfaces. Minimal sample

preparation, use in ambient conditions, and the ability to image non-conducting specimens at the atomic scale (in some cases) make AFM an extremely versatile and useful form of microscopy. Recent advances in AFM have allowed the successful imaging of soft polymeric and biological samples and the imaging of magnetic microstructures.

The laboratory setup for the AFM shown in Figure 3.19 includes the scanner, sample display screen, control screen, processor, and image display screen. A special table to isolate mechanical and acoustical vibrations is also usually necessary to perform high-resolution (atomic scale) work.

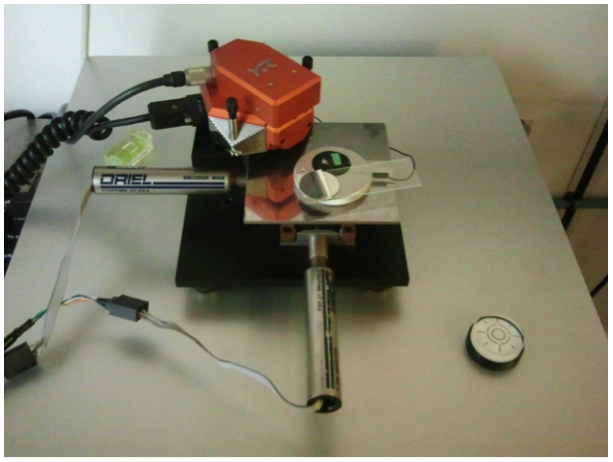

Figure 3.19: AFM unit used for the imaging of the surface morphology and roughness of the samples.

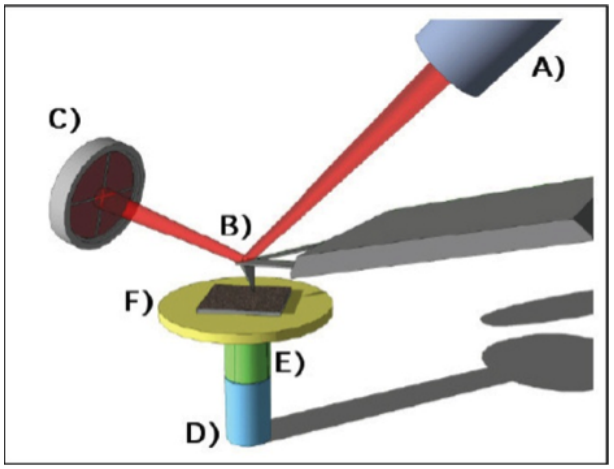

Figure 3.20: An explicative cartoon of the AFM working principle [179].

Figure 3.20 illustrates the working principle of an AFM. It is possible to recognize the laser (A) focusing a laser beam at the top end of a cantilever (B), from where it is reflected at the centre of a 4 quadrant photodiode (C). Every cantilever deformation (bending or torsion) will be easily detected as spot movements on the photodiode. At the end of cantilever there is a very sharp tip in close proximity with the sample

surface (F). The sample surface is moved below the tip using an x and y piezoscanner (E). During the rastering process the tip bends (or changes its resonant frequency) as a function of surface morphology. A z piezoscanner (D) approaches or moves the surface (F) away from the tip, in order to maintain constant bending or resonant frequency. The voltages rerquired to do these corrections are used to reconstruct the surface topography.

3.2.1.3 X-Ray Diffraction Technique

X-ray diffraction techniques are the principal source of information about the crystallographic structure of materials, despite the complementary information allowed by electron and neutron diffraction. Typical interatomic distances in a crystalline solid are of the order of one Ångström (0.1 nm). An electromagnetic probe of the microscopic structure of a solid must therefore have a wavelength close to this short value, corresponding to an energy value of $h\nu = hc/\lambda = hc/10^{-8}$ cm $\approx 12.3 \times 10^3$ eV. Energy values like this are characteristic of X-rays (1 keV-120 keV). Therefore, a crystal may be seen as a three-dimensional diffraction grating for such electromagnetic radiation. W.L. Bragg accounted for this by regarding a crystal as made out of parallel planes of atoms, spaced a distance d apart (lattice planes). The conditions for a sharp peak in the intensity of the scattered radiation are the following:

- The X-rays should be specularly reflected by the ions in one plane, and
- The reflected X-rays from successive planes should interfere constructively.

X-rays specularly reflected from adjoining planes are schematically shown in Fig. 3.21.

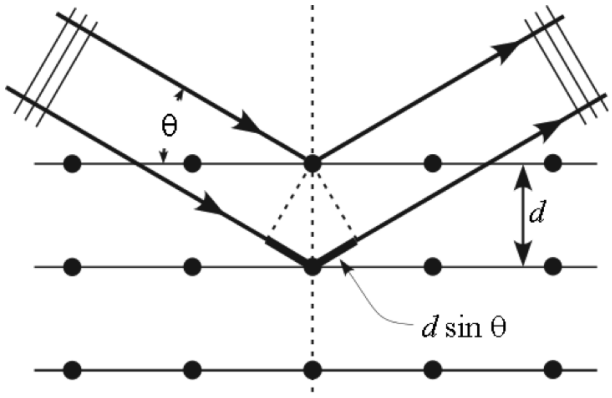

Figure 3.21: A Bragg reflection from a particular family of lattice planes, separated by a distance d. Incident and reflected rays are shown for two neighbouring planes. The path difference is given by $2d_{hkl}\sin(\theta)$ [180].

The path difference between the two rays is just $2d_{hkl}\sin(\theta)$, where θ is the angle of incidence[1]. For the rays to interfere constructively, this path difference must be an

[1]The angle of incidence in X-ray crystallography is conventionally measured from the plane of reflection, rather than from the normal to that plane, as in classical optics. It should be noted that θ is just half the angle of deflection of the incident beam, which is 2θ.

integral number of wavelengths, leading to the well-known Bragg law,

$$2d_{hkl}\sin(\theta) = n\lambda \tag{3.2.1}$$

where n defines the order of the reflection, d the interplanar spacing and λ the wavelength of the incident radiation.

Modern X-ray crystal analysis is usually done with X-ray diffractometers. A diffractometer has a radiation counter (detector) to detect the angle and the intensity of the diffracted beam. In particular, when using the Bragg-Brentano or $\theta - 2\theta$ configuration, the detector is rotated at double the angular speed of the sample.

A recorder automatically plots the intensity of the diffracted beam as the counter moves on a goniometer circle which is in synchronization with the specimen over a range of 2θ values. In this way, both the angle of the diffracted beam and the intensity can be recorded at the same time. An X-ray diffraction pattern is thus a plot of the intensity of the diffracted beam versus the diffraction 2θ angle, the peak intensities and their 2θ angular positions giving information about the crystallographic structure of the material. The 2θ angular positions are related to certain lattice plane distances d_{hkl} and thus to certain lattice planes (hkl).

Bragg's law states the condition for a sharp-diffraction peak (Fig. 3.22(a)) from an infinite crystal with a perfect 3D order. Typically, the diffraction peak has a finite width, which is induced either by instrumental broadening (due to non-ideal X-ray optics, wavelength dispersion, sample transparency, axial divergence, flat sample effect, and detector resolution) or with deviations from ideal crystallinity, such as finite crystallite size, extended defects (stacking faults and antiphase boundaries) and lattice strain (microstrain).

By analysing this broadening it is possible to extract information about the microstructure of a material, in particular the average crystallite size can be inferred using the Scherrer equation [180], given by

$$< t >= \frac{K\lambda}{B\cos(\theta_B)} \ , \tag{3.2.2}$$

where $< t >$ stands for the average crystallite size, K is a constant whose value depends on the shape(s) of the crystallites (typically between 1 and 0.9) and B is the peak breadth (in radians $2\theta_{hkl}$) centred at the Bragg angle θ_{hkl}, corresponding to the (hkl) reflection (see Fig. 3.22(b)). It is worth noting here that crystallite size should not be confused with particle size, which can be associated with the presence of polycrystalline aggregates.

All samples were examined using a Bruker axs D8 ADVANCED X-ray Diffractometer and Cu K_α radiation (λ=0.15418 nm) at 40 KV and 30 mA in $\theta - 2\theta$ coupled mode (Bragg-Brentano configuration) [181]. The diffraction patterns were recorded in the range 18°-60° with a step size of 0.02° and a time per step of 15 seconds. While recording XRD spectra, the samples were rotated to homogenize the measurements.

3.2.1.4 FTIR-spectroscopy

Infrared spectroscopy is an essential and crucial characterisation technique to elucidate the structure of matter at the molecular scale. The chemical composition and the bonding arrangement of constituents in a homo-polymer, co-polymer, polymer composite

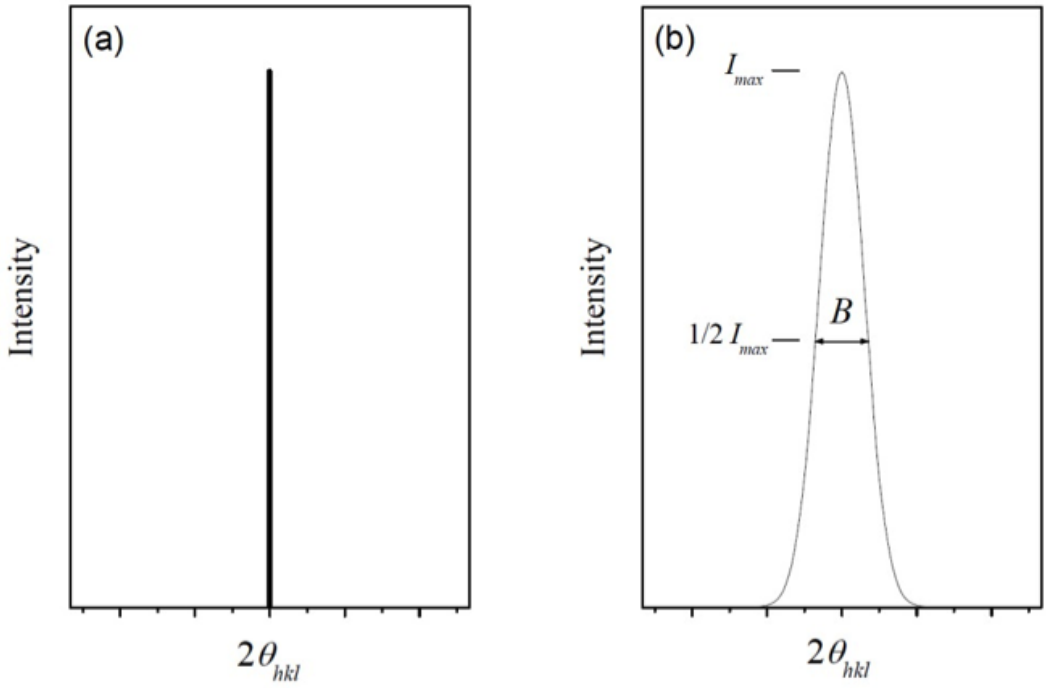

Figure 3.22: Effect of fine crystallite size on diffraction lines. a) (hkl) diffraction peak from an infinite crystal with a perfect 3D order (hypothetical case); b) peak broadening due to small crystallite size.

and polymeric materials in general, can be obtained using Infrared (IR) spectroscopy [182].

FTIR spectrometers obtain the IR spectrum by Fourier transformation of the signal from an interferometer with a moving mirror to produce an optical transform of the infrared signal. Numerical Fourier analysis gives the relationship between intensity and frequency, that is the IR spectrum. The FTIR technique can be used to analyse gases, liquids and solids with minimal preparation [183].

Fourier transform infrared spectroscopy (FTIR) gives information about the vibrational energy of the molecules in a sample, i.e. absorbance in the infrared region. By a complex array of mirrors and lenses, a result is received as an interferogram, which, by applying a Fourier transform (FT), is converted into a spectrum with absorbance versus wavelength [184], as can be seen in Fig. 3.23.

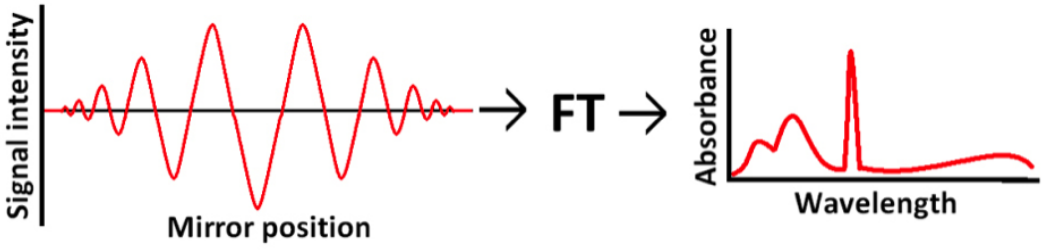

Figure 3.23: Illustration of the FTIR raw data to spectrum procedure.

Changes involving groups with strong absorbance in the IR-region, e.g. carboxylic groups, can easily be seen in an FTIR experiment. If the carboxylic group binds to another species, the vibration energy would change and intensity in the carboxylic range would decrease proportional to the ratio of bound functional groups.

The spectrometer may operate in transmission or reflection mode, but also in attenuated total reflection (ATR) mode, which have been widely used during the last two decades. The transmission mode is very suitable for quantitative analysis, since the main parameters to apply on the Beer-Lambert law are known, or easily estimated. The reflection mode is used when a polymer is not well dissolved at room temperature, and films or pellets of the sample are characterized. That is also the case for polyolefins and some engineering polymers like PET.

The ATR objective has a polished face of diamond, germanium or zinc selenide (ZnSe) that is pressed into contact with the sample [185]. Infrared reflection is attenuated by absorption within a surface layer a few micrometres deep. In this case, a good contact is required, but that is easy for most polymers, and the advantage is that no sample preparation is required. Therefore, powders, films, gels and even polymer solutions can be characterized.

The absorption versus frequency characteristics of light transmitted through a specimen irradiated with a beam of infrared radiation provides a fingerprint of molecular structure. Infrared radiation is absorbed when a dipole vibrates naturally at the same frequency in the absorber. The pattern of vibrations is unique for a given molecule, and the intensity of absorption is related to the quantity of absorbance. In the IR region, each group has several and different patterns of vibration such as stretching, bending, rocking, etc. The absorbance of these bands is proportional to their content, based on the Lambert-Beer law.

Thus, infrared spectroscopy permits the determination of components or groups of atoms that absorb in the infrared range at specific frequencies, permitting identification of the molecular structure [186, 187].

3.2.2 Advanced nuclear methods for composite track-etched membrane characterisation

3.2.2.1 Particle-induced X-ray emission spectroscopy

Particle-induced X-ray emission, commonly abbreviated PIXE, is a technique for multi-elemental analysis. A beam of accelerated protons or, on occasion, heavier ions, excites characteristic X-rays in the atoms of a specimen. The X-ray spectrum is recorded in energy-dispersive mode by a semiconductor X-ray detector. This fully quantitative technique allows for determining elemental concentrations down to part-per-million detection limits. With highly focused proton beams, there is the additional option of both one- and two-dimensional imaging of element distributions in a specimen.

PIXE provides a non-destructive procedure for the simultaneous analysis of 72 inorganic elements (ranging from Sodium to Uranium on the Periodic Table) for solid, liquid, and thin film materials. PIXE offers the advantage of analysis, without needing time consuming sample preparation, thereby minimising the potential for error [188].

There are four main physical processes of importance to PIXE:

i) When a charged particle (proton or heavier ion) enters the material, it encounters numerous inelastic collisions by sample atoms;

ii) The energy of the ion along its trajectory decreases according to the specific energy loss (stopping power);

iii) From some of the numerous ionised atoms along the particle path, characteristic X-rays are emitted with a probability given by the X-ray production cross section;

iv) X-rays emerging from the sample are attenuated in the material.

Particle Induced X-Ray Emission (PIXE) is usually performed as an ancillary analytical method to RBS, using the same ion beam accelerator. In addition to the backscattering of ions, the interaction of the ion beam (He^+, H^+; 0.3 to a few MeV energy) with the sample also results in X-ray emission, as a decay process from excited states, analogous to that produced by X-ray impact, or electron beam impact. The elements present in the sample can be identified from the characteristic X-ray energies emitted and the composition can be obtained from the relative intensities.

Absolute quantification (number of atoms/cm^2) is easier than for either X-ray Fluorescence Spectroscopy (XRF) or Energy-dispersive X-ray spectroscopy (EDX), because of precise knowledge concerning the flux of the impinging ion beam and the cross-sections for X-ray emission.

The depth probed is dependent on the ion energy used and the material, but is less than 10 μm and so is more similar to EDX than XRF (a bulk measurement). Detection limits are much better than in EDX, however, because of a much lower background signal. They are in the 0.1 to 100 ppm range, being highest for the light elements, where the competing Auger process is least effective [189].

3.2.2.2 Rutherford backscatter spectroscopy

Rutherford Backscattering Spectrometry (RBS) is a widely used nuclear method for the near surface layer analysis of solids. A target is bombarded with ions at an energy in the MeV-range (typically 0.5-4 MeV), and the energy of the backscattered projectiles is recorded with an energy sensitive detector, typically a solid state detector. RBS allows for the quantitative determination of the composition of a material and depth profiling of individual elements. RBS is quantitative without the need for reference samples, non-destructive, has a good depth resolution of the order of several nm, and a very good sensitivity for heavy elements of the order of parts-per-million (ppm). The analysed depth is typically about 2 μm for incident He-ions and about 20 μm for incident protons. Detection of the scattered particles is done for scattering angles larger than 90°, the energy spectra holding information about the target composition and the in-depth distribution of the constituent elements.

The physical quantities and concepts that enable one to analyse the RBS spectra are the same that characterise the interactions between beam ions and target atoms:

- The kinematic factor, K, which allows for mass analysis, i.e. the identification of the constituent elements in the target, through the conversion of features in the energy spectra in mass spectra;

- The scattering cross-section, σ, which allows for a quantitative analysis of composition, by establishing a correspondence between spectral intensities and the density of the corresponding scattering nuclei;
- The target stopping power, S, which allows for depth analysis, i.e. the conversion of energy intervals in the spectra to depths - the energy scale thus becomes a depth scale for each element in the target material;
- Energy straggling, the fluctuations in the energy losses of the incoming ions through the target, limits the possible depth resolution.

The scattering cross-section and stopping power concepts give the technique the unique ability of converting a spectrum into a depth profile, i.e. in a concentration versus depth curve, for each element identified in the spectrum by its kinematic factor [190].

The energy width (ΔE) of the particles scattered at the front and back surfaces of the film is related to the number of atoms per unit area (Nd) of the film through the equation

$$\Delta E = [\epsilon_0] N d \ , \tag{3.2.3}$$

where $[\epsilon_0]$ is the surface approximation for the stopping cross section factor, N is the atomic density and d the thickness of the film [191].

3.2.3 Optical methods used composite track-etched membrane characterisation

3.2.3.1 Optical spectroscopy

Optical spectroscopy is a means of studying the properties of physical objects based on measuring how an object emits and interacts with light. A spectrophotometer is an instrument which measures the absorption, transmission and reflectivity of a variety of materials. Instrument design necessitates that the wavelength of radiation to be studied must be a narrow "window". Accordingly, the predetermined electromagnetic radiation wavelengths for ultra-violet (UV), visible (VIS) and near-infra-red (NIR) radiation are defined as follows:

- UV radiation - 300 to 400 nm
- VIS radiation - 400 to 765 nm
- NIR radiation - 765 to 3200 nm

UV-VIS-NIR spectroscopy is useful to characterise the absorption, transmission and reflectivity of materials such as thin films and coatings. Optical characterisation of thin films involves the determination of many properties such as:

- Film thickness;
- Complex index of refraction;
- Absorption coefficient (α);

- bandgap, etc.

In this study UV-VIS-NIR spectroscopy will mainly be used to determine transmittance and the film's energy bandgap, E_{gap}, which represents the minimum photon energy needed for a direct electronic transition from the valence band to the conduction band. The measurement of the absorption coefficient for various energies gives information about the bandgaps of materials. Knowledge of these bandgaps is extremely important for understanding the electrical properties of semiconductors, and is therefore of great practical interest.

Optical analysis thus provides a good way of examining the properties of semiconductors and is usually the preferred method for measuring thin films, because it is accurate, non-destructive, and requires little or no sample preparation. The transmission/absorption spectrophotometry technique was used to investigate the manufactured modified TiO_2 and Ag-TiO_2 thin films [192].

For transmission/absorption spectrophotometry a commercial spectrophotometer (CECIL 2000 Series, Aquarius) was used, allowing to record spectra in the UV-VIS-NIR range, from 200 to 1100 nm. In practice, the transmission/absorption measurements are limited to wavelengths at which samples have medium absorption coefficients. For high absorption there is virtually no transmission. However, if α is too low, thin film interference effects will appear, because light waves that are reflected on the two sides of the film will be superimposed on one another[193].

A short description will now be given of the architecture of the optical system and of the general principles governing its function. To compensate for the complicated intensity distribution of the light source, the spectrophotometer does not measure absolute values, but instead, the signal from the sample is compared to a reference beam. Additionally, a baseline is recorded prior to the measurements to calibrate the instrument.

Fig. 3.24 shows a typical schematic for a spectrometer. The functioning of this instrument is relatively straightforward. A beam of light from a visible and/or UV light source (coloured red) is separated into its component wavelengths by a prism or diffraction grating. Each monochromatic (single wavelength) beam, in turn, is split into two equal intensity beams by a half-mirrored device. One beam, the sample beam (coloured magenta), passes through the compound being studied (sample). The other beam, the reference (coloured blue), passes through the reference compound (air or sample skeleton). The intensities of these light beams are then measured by electronic detectors and compared.

Using the approximation for a transparent sample, we obtain Beer's law, the well-known relationship between extinction coefficient and transmittance, given by

$$\alpha = \left(\frac{1}{d}\right) \ln\left(\frac{1}{T}\right) \qquad k = \frac{\alpha\lambda}{4\pi} \ , \tag{3.2.4}$$

where d is the thickness of the film, T is the transmittance and k extinction coefficient. This relationship can only be used when reflection can be neglected and the sample is sufficiently transparent.

TiO_2 is a sufficiently transparent material, thus this relation has been used to calculate the absorption coefficient and the bandgap of the film, using the relationship known as the Tauc-plot and given by

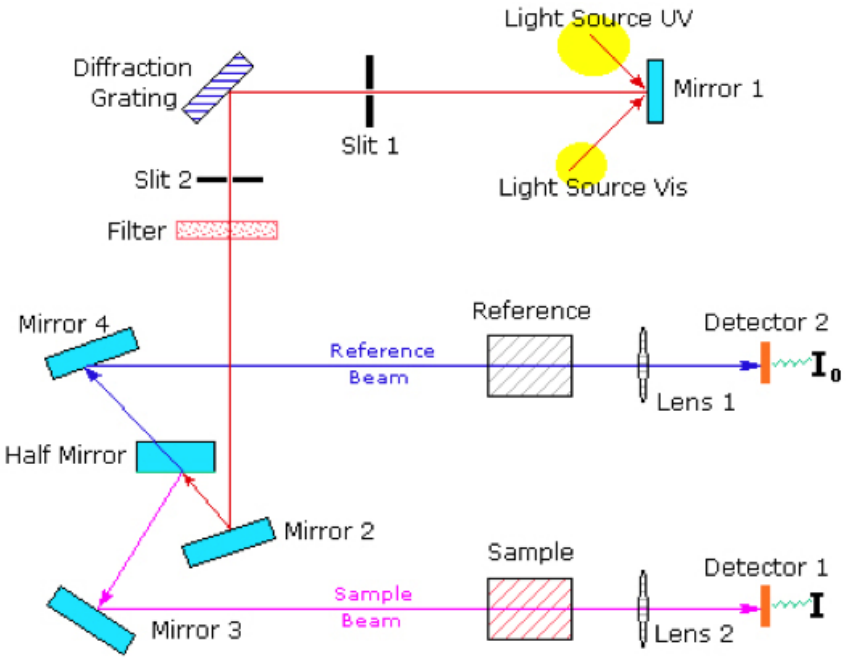

Figure 3.24: Schematic of a typical spectrometer.

$$(\alpha h\nu) = A(h\nu - E_g)^2, \tag{3.2.5}$$

where A is a constant, E_g is the optical bandgap in eV and $h\nu$ is the photonic energy in eV [194].

In order to calculate the optical bandgap energies of the thin films, a plot of $(\alpha h\nu)^{1/2}$ as a function of photon energy $(h\nu)$ is made, and by extrapolating the linear portion near the onset of the absorption edge to the energy axis (at α=0).

Alternatively the bandgap can be estimated from Planck's relationship using

$$E = \frac{hc}{\lambda}, \tag{3.2.6}$$

where h= Planck's constant $\approx 6.626 \times 10^{-34}$ J-s, c = Speed of light $\approx 3.0 \times 10^8$ m/s, λ = Cut-off wavelength in nm [195], and 1eV $\approx 1.6 \times 10^{-19}$ J (conversion factor).

Albeit a much faster approach, the margin of error is much larger.

3.3 Reactor design and analyses of dye degradation in water

Membrane filtration can be a very efficient and economical way of separating components that are suspended or dissolved in a liquid. The membrane is a physical barrier that allows certain compounds to pass through, depending on their physical and/or chemical properties.

Microfiltration (MF) is the process of removing particles or biological entities in the 0.025 μm to 10.0 μm range from fluids by passage through a microporous medium such as a membrane filter. Although micron-sized particles can be removed by use

of non-membrane or depth materials, such as those found in fibrous media, only a membrane filter having a precisely defined pore size can ensure quantitative retention. Membrane filters can be used for final filtration or pre-filtration, whereas a depth filter is generally used in clarifying applications where quantitative retention is not required or as a pre-filter to prolong the life of a downstream membrane. Membrane and depth filters offer certain advantages and limitations. They can complement each other when used together in a microfiltration process system or fabricated device. The retention boundary defined by a membrane filter can also be used as an analytical tool to validate the integrity and efficiency of a system. For example, in addition to clarifying or sterilizing filtration, fluids containing bacteria can be filtered to trap the micro-organisms on the membrane surface for subsequent culture and analysis. Microfiltration can also be used in sample preparation to remove intact cells and some cell debris from the lysate. Membrane pore size cut-offs used for these types of separation are typically in the range of 0.05 μm to 1.0 μm.

Two different configurations of operating a filtration process were considered in this study, namely dead-end filtration and cross-flow filtration

3.3.1 Dead-end Filtration

The most basic form of filtration is dead-end filtration. The complete feed flow is forced through the membrane and the filtered matter is accumulated on the surface of the membrane. The dead-end filtration is a batch process as accumulated matter on the filter decreases the filtration capacity, due to clogging. A next process step to remove the accumulated matter is required. Dead-end filtration can be a very useful technique for concentrating compounds. Fig. 3.25 and 3.26 shows both the schematics of how such a system works and the physical reactor designed and built for this study.

See Appendix D for CAD drawings of the system.

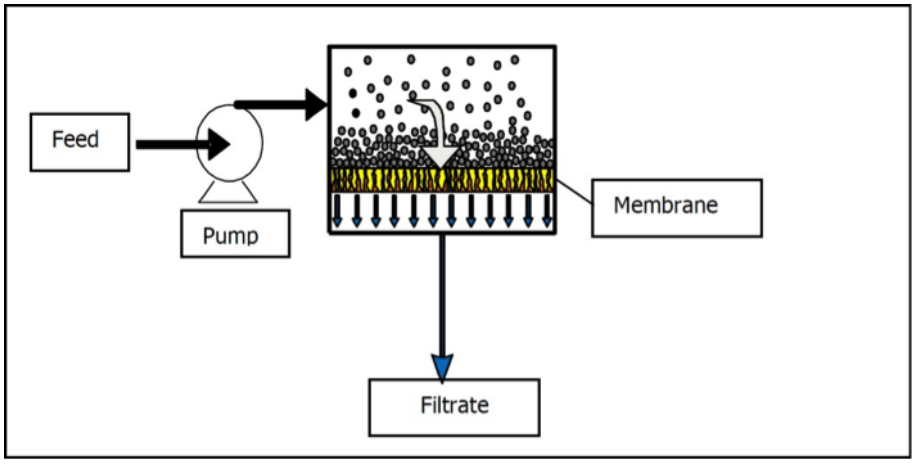

Figure 3.25: Dead-end process schematics.

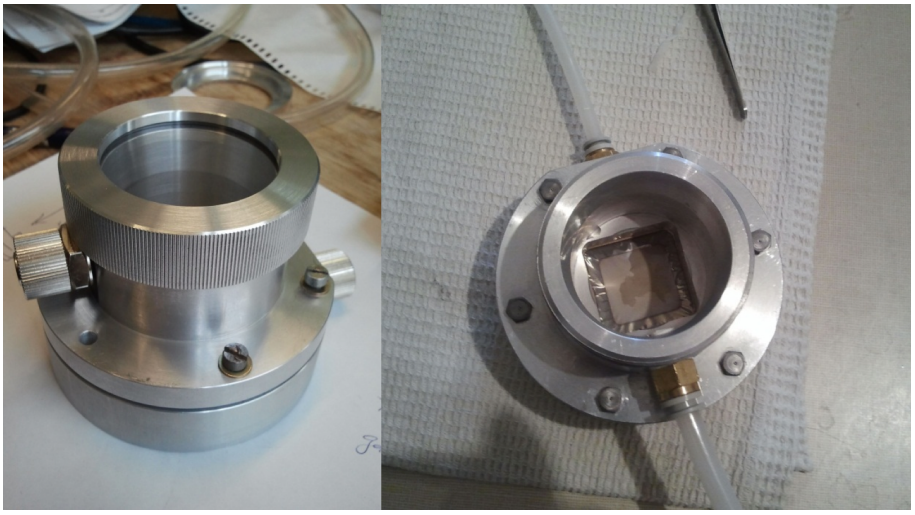

Figure 3.26: Dead-end reactor.

3.3.2 Cross-flow Filtration

With cross-flow filtration a constant turbulent flow along the membrane surface prevents the accumulation of matter on the membrane surface. The feed flow through the membrane reactor has an elevated pressure as driving force for the filtration process and a high flow speed to create turbulent conditions. The process is referred to as "cross-flow", because the feed flow and filtration flow direction have a 90 degrees angle. Cross-flow filtration is an excellent way to filter liquids with a high concentration of filterable matter. Fig. 3.27 and 3.28 both show the schematics of how such a system works and the physical reactor designed and built for this study.

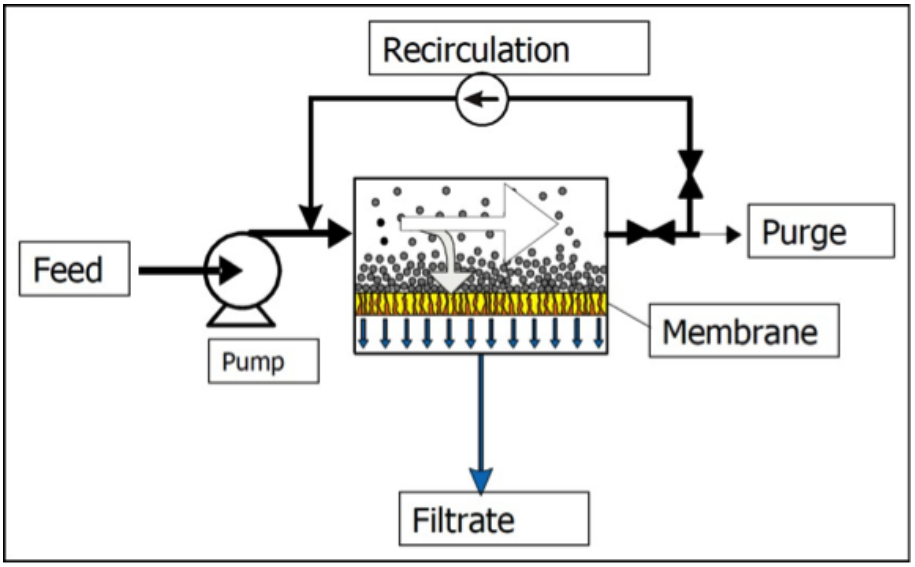

Figure 3.27: Cross-flow process schematics.

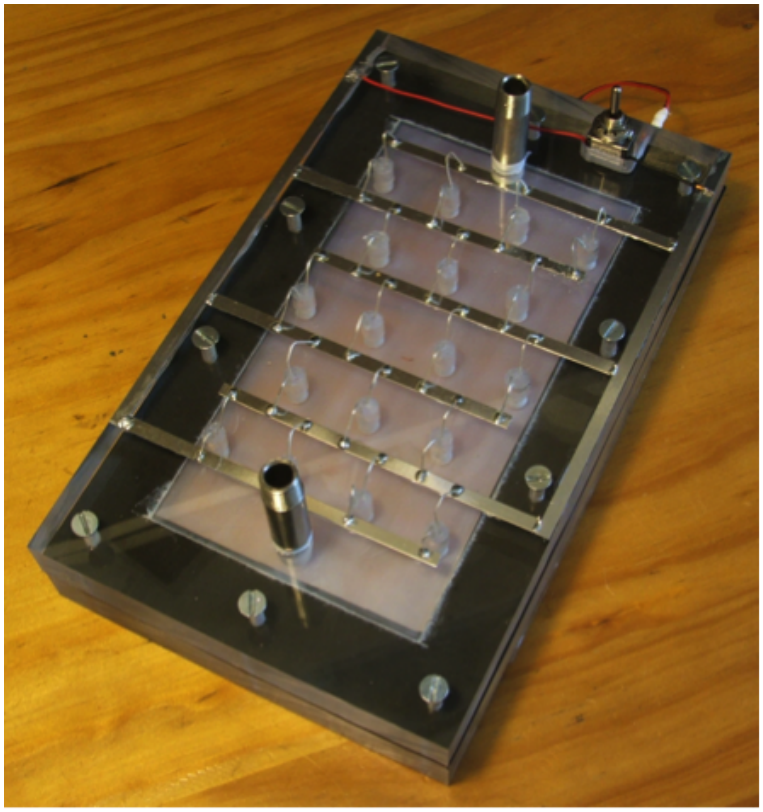

Figure 3.28: Cross-flow reactor.

3.3.3 Experimental Conditions

In order to test the effectiveness of the modified TiO_2 and Ag-TiO_2 TMs, both a cross-flow and dead-end reactor was constructed. The aim thereof, to filter out Rhodamine 6G dye from deionised water at a pre-defined concentration of 100 ppm. As the dye accumulates on the membrane surface, theoretically caking would cause the system efficiency to drop to a point of stand still, as the pores are clogged, should a standard TM be used. However with the TiO_2 and Ag-TiO_2 TM modifications, "dye-degradation" should take place when exposed to UV light. The light frequency chosen was 355 nm.

PET TM is optically transparent, thus it was decided to make use of UV-VIS-NIR spectroscopy to measure the change in transmittance of the samples used during the experiments. As the caking layer increases, the transmittance is expected to decrease, due to the reduction in transparency. Similarly, as the photocatalytic layer oxidises the cake formation, the transparency is expected to increase again, leading to higher levels of transmittance. Fig. 3.29 shows the dead-end reactor busy oxidising the Rhodamine 6G dye contaminated water sample.

See Chapter 4 for further elaboration on the results of these experiments.

Figure 3.29: Experimental setup. (Top left) Glass reservoir containing water/dye mixture with gravity feed, (Top right) system in operation and (Bottom) system in idle state.

Chapter 4

Results and discussions

This chapter describes the approaches in the surface modification of TMs by inverted cylindrical magnetron sputtering (ICMS) and thermal evaporation. Sputtering is a low cost coating technology for the production of uniform thin films on large-scale. This thesis reports on the synthesis and feasibility of reproducible high quality titanium dioxide (TiO_2) by ICMS. Structural, morphological, interfacial analysis and optical properties of synthesized TiO_2 as well as nanocomposite Ag-TiO_2 thin films are reported.

4.1 First Approach - TiO_2 surface modified TM using the ICM sputtering technique

Fig. 4.1 shows a virtual cross-section of how the TM looks like before and after sputtering.

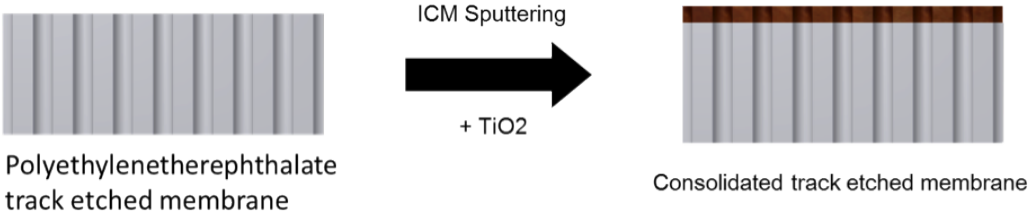

Figure 4.1: TiO_2 surface modified track etched membrane using inverted cylindrical magnetron sputtering.

However, before sputtering the TM with TiO_2, certain parameters needed to be fixed, thus securing the future repeatability of any additional experiments. The film properties can be regulated by adjusting various sputter parameters. The following parameters need to be considered when sputtering:

- The current mainly influences deposition rate;
- The voltage determines yield;

TiO_2 deposition parameters	To start system	To run system
Voltage (NB start)	650 V (min)	385 V
Power (NB running)	135 W	125 W
Current	0.5 A	0.325 A
Gas cylinder Ar/O_2	350 kPa	350 kPa
Gas Ar	40 mmHg	40 mmHg
Gas O_2	0 mmHg	10 mmHg
Time	0 min	45 min
Frequency	21 kHz	21 kHz
Duty cycle	80%	80%
Substrate-to-target distance	50 mm	50 mm
Substrate temperature	17°C	30°C

Table 4.1: Sputter parameters

- Pressure determines the mean free path and, together with the target-substrate distance,largely influences crystallinity and film porosity;
- The composite gas mixture influences target poisoning and film stoichiometry;
- The substrate temperature influences the deposited films' crystallinity.

For depositing TiO_2 a large initial power surge is required for starting the process and, as the target undergoes poisoning throughout deposition, each new run would require a higher initial energy input and similarly a higher running voltage as the oxide layer encapsulating the target grows.

Therefore, proper maintenance of the sputter system, especially the cleaning of the chamber and target after every 10 hours of use is vital, otherwise it would result in inconsistent thin film formation and problems with the plasma formation. Worst case scenario, the magnetron sputter head itself could be damaged.

After some experimentation the following parameters, shown in Table 4.1, were decided upon.

The reason for choosing these specific parameters is as follows:

- During the sputtering process the substrate gets exposed to very high temperatures. Keeping the glass transition point and the melting point of PET TMs in mind, a cooling system was designed and developed. The cooling system ran at 17°C when the system was in idle or vacuum mode, and maintained the TM surface temperature at 30°C during deposition. The target to substrate distance was fixed at 50 mm to allow for the desired deposition area (spot size).
- Experimenting with Argon-Oxygen gas mixtures showed that the more oxygen is used, the faster the deposition rate, but the quicker target poisoning takes place. This target poisoning results in a decrease in deposition rate and shortens the intervals between machine maintenance. The current infrastructure does not allow for precise gas measurements, but it was found that, when using less than 10% oxygen, the TiO_2 deposition rate was very low. However, using more than

30% oxygen resulted in the target oxidising too fast. Therefore a 80:20 percentage ratio of Ar-to-O_2 mixture was decided upon.

- The "smart" pulsed-dc power supply used allows limits to be set for voltage, current and power. At the start of deposition it was found that the voltage was the limiting factor, as the initial energy burst required to ignite the plasma for Ti is rather high. A voltage of 650 V was chosen as not to inhibit plasma formation. However, when in operation, the power was the limiting factor. During ICM sputtering, the more power applied to the system, the more heat is produced in the head (or gun) housing the target.
- Magnetron sputtering makes use of permanent magnets to increase the ionisation efficiency and provide a uniform magnetic field in the interaction space between the cathode and the anode. Therefore, the cooling of the system is vital. When depositing TiO_2, the deposition rate was estimated to be around 1.1 nm per minute. At this rate the process would take approximately 45 min to deposit 50 nm of TiO_2. The water cooling system available is very old and it was found that, when depositing for an hour, the cooling would fail if more than 125 W were supplied to the magnetron.

4.1.1 General methods used for composite track-etched membrane characterisation

4.1.1.1 Morphological properties (SEM & AFM)

Fig. 4.2 shows a typical SEM image, taken at the *Joint Institute for Nuclear Research* (JINR) in Russia, of the unmodified polyethylene terephthalate track-etched membranes used in this study. Under thirty thousand times magnification it is easy to see the pores and their distribution over the membrane. Due to the way they are produced, no two track-etched membranes are identical.

As a result of this unique property TMs have, quality control is crucial. As seen in Fig. 4.2, some pores are larger than others. That is in part due to the somewhat random paths taken by the heavy ions used to produce the tracks.

Keeping this in mind, an Excel program was written to monitor these deviations in pore size by making use of basic statistics and probability distributions. The bell-shaped probability density function can be derived from the Student's t-distribution. By measuring the pore sizes of randomly selected pieces of TM from the same batch, it was possible to approximate the boundaries that the pores will fall in for that batch. Fig. 4.3 shows an example of 10 measurements.

At the beginning of the study, the first problem encountered was that of dealing with "how to sputter on a polymer". The initial design and calibrations were done on silicon wafers and glass slides. However, the first few TMs did not survive deposition. They were simply destroyed by the heat generated during the sputtering process. Before the Peltier was added to the cooling system, a layer was tested just using the water cooled copper base. The resulting Fig. 4.4 shows the SEM image of that deposition, taken at the Engineering Faculty of Stellenbosch University, RSA.

The track-etched membrane showed signs of degradation, but it was the first membrane to survive deposition. However, instead of growing a thin film of TiO_2, nanopar-

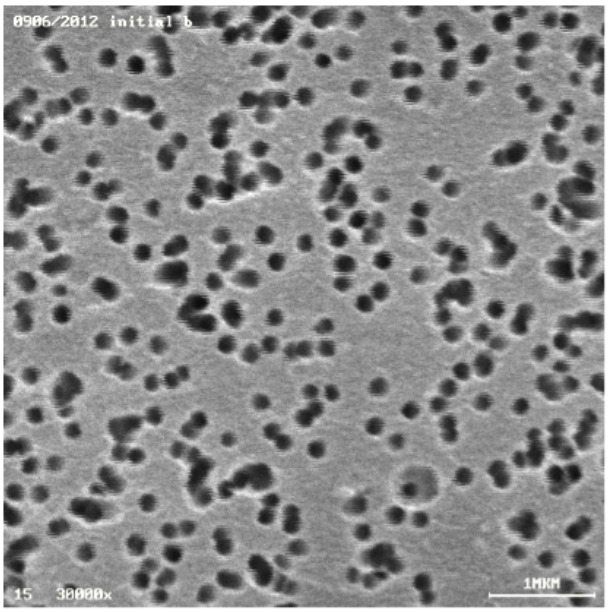

Figure 4.2: PET track membrane with pore diameter of 0.1 μm and 12 μm thick.

Samples	Sample Size	Sample Mean	Sample Standard Deviation	Sample Standard Error
	10	0.808	0.110634533	0.034985711
	Degrees of Freedom	Level of Significance	Level of Confidence	t Value
	9	5%	95%	2.262157163
	Width of Half the Confidence Interval		Confidence Interval Boundaries	
	0.079143178		0.728856822	0.887143178
0.91				
0.84				
0.88				
0.62				
0.83				
0.64				
0.79				
0.75				
0.86				
0.96				

Figure 4.3: Pore size statistics.

ticles were produced, and island cluster formation could be seen. The cooling was still insufficient and the design had to be improved. That is where the idea of using the water-cooled base as a heat sink for a sample holder, housing a Peltier cooler, originated, thus allowing for the creation of the planar layer, as shown in Fig. 4.5.

The result of the surface morphology study of the TiO_2 films clearly proved that proper cooling not only affected the growth of TiO_2, but also helped to maintain the TM surface integrity during deposition.

In this study the main use of the AFM was for calibration purposes, by calculating deposition rate and to approximate surface roughness. TMs are rather delicate and most tests are destructive. In order to calibrate the system, a more rugged substrate

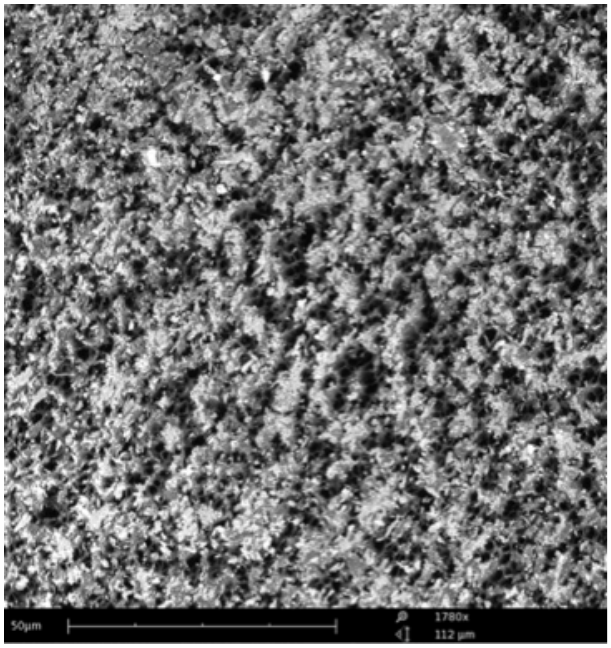

Figure 4.4: TM with TiO_2 and insufficient cooling.

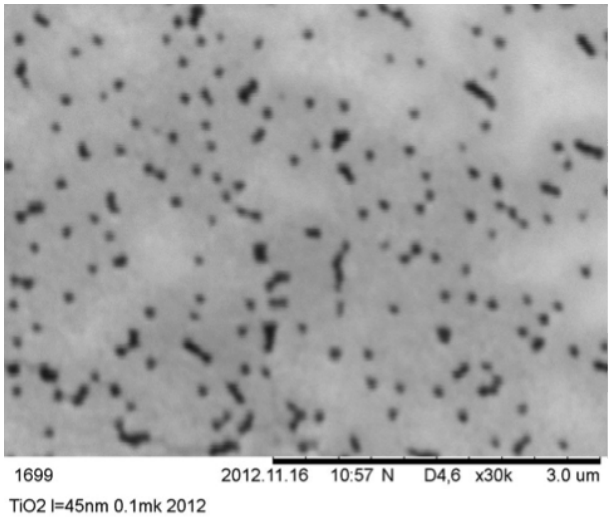

Figure 4.5: TM with TiO_2 and proper cooling.

was needed, thus silicon was chosen instead of the TM. Two methods were applied to calibrate the deposition rate of TiO_2:

- The first was the photoresist method. A drop of photoresist was placed on a 10×10 mm silicon disk and then hard baked. Once dry, the silicon wedge was placed inside the sputtering chamber and TiO_2 was deposited at 5 minute intervals from 0 to 50 minutes on various disks. After deposition the silicon wedges were washed in acetone to dissolve the photoresist, thereby forming a "step-edge" that could be measured by an AFM in tapping-mode, with a non-contact tip.
- The biggest problem with the photoresist test is that it is time consuming and that

the sample had to be washed in acetone in an ultrasonic bath to remove the photoresist after deposition. An alternative test was devised by using Rubylith™instead, as a piece can be stuck on the silicon and peeled off afterwards. This method was much faster and did not require any post-deposition processing, other than just removing it from the sample with tweezers.

Taking into account that these tests only give an average deposition rate, there is always the possibility that some of the TiO_2 can come off in the washing process or that peeling off the Rubylith™can tear the TiO_2 layer. The final thickness of theTiO_2 deposited on TM itself may vary due to different growth or cooling patterns and bonds on different surfaces. RBS measurements, discussed in the advanced nuclear methods section of this chapter, will be considered for the determination of TiO_2 layer thickness again.

Fig. 4.6(a) and (b) shows one of the topographical scans done during the calibration process. By measuring the steps formed, we were able to plot Fig. 4.6(c). The rate of deposition was determined to be in the range of 1 to 1.2 nm per minute.

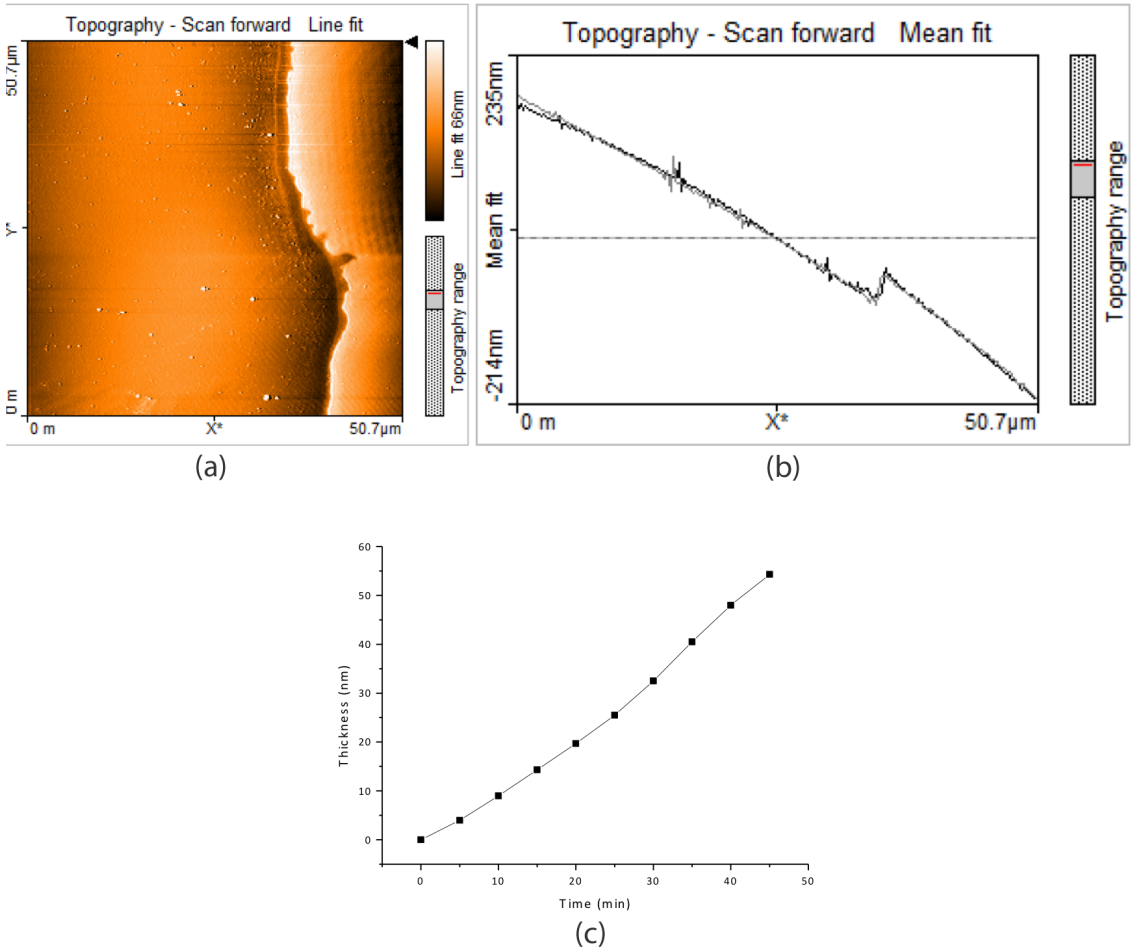

Figure 4.6: AFM results from a TiO_2 thin film morphological study. (a) 3D surface view, (b) step-edge formed, and (c) deposition rate of approximately 1.2 nm / min on TM.

4.1.2 Structural properties (XRD, IR & FTIR)

4.1.2.1 IR and FTIR (For chemical bond analysis)

The infrared spectrum of a sample is recorded by passing a beam of infrared light through the sample. When the frequency of the IR is the same as the vibrational frequency of a bond, absorption occurs. Examination of the transmitted light reveals how much energy was absorbed at each frequency (or wavelength). This can be achieved by scanning the wavelength range using a monochromator. Alternatively, the whole wavelength range is measured at once using a Fourier transform instrument and then a transmittance or absorbance spectrum is generated using a dedicated procedure. Analysis of the position, shape and intensity of peaks in this spectrum reveals details about the molecular structure of the sample.

This technique works almost exclusively on samples with covalent bonds. Simple spectra are obtained from samples with few IR active bonds and high levels of purity. More complex molecular structures lead to more absorption bands and more complex spectra.

The IR studies were done at the *Joint Institute for Nuclear Research* (JINR) in Russia. Fig. 4.7 shows the full range scan and all of the peaks absorbed. Most peaks are for the TM itself. For TiO_2 the 100 to 800 cm^{-1} range is of interest.

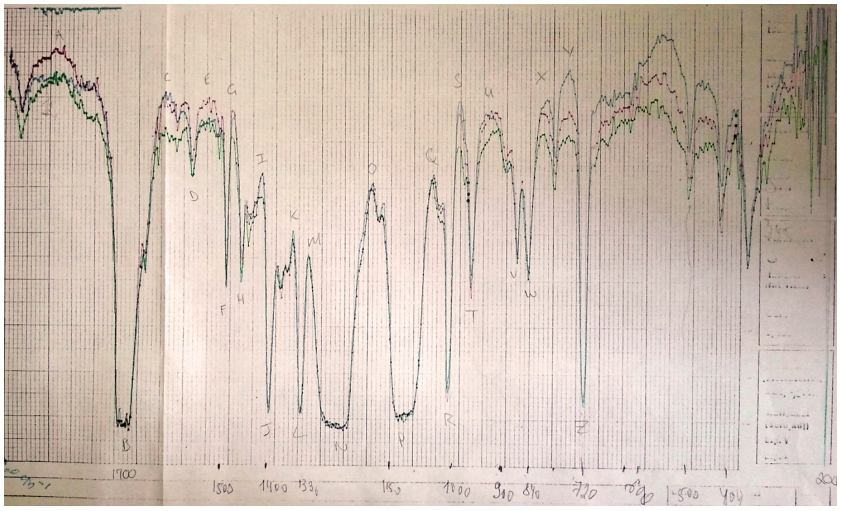

Figure 4.7: Full-range scan.

4.1.2.2 XRD (For crystallinity study)

In the initial XRD studies of the TiO_2 thin film development, before depositing on silver and improving the substrate cooling, the resulting deposition yielded mostly amorphous TiO_2, as can be seen in the XRD spectrum given in Fig. 4.8, with what seems like a possible peak around 25°, which could indicate some formation of brookite TiO_2, but this is just speculation. A more thorough XRD analysis will be done in the following section, where crystalline TiO_2 was obtained.

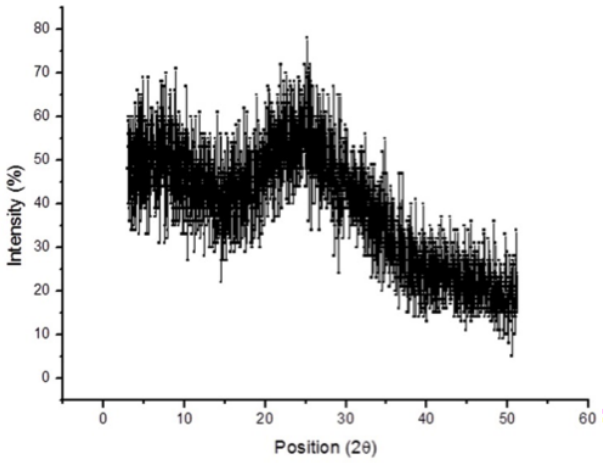

Figure 4.8: Amorphous and possible Brookite TiO_2 peak.

4.1.3 Advanced nuclear methods for material for composite track-etched membrane characterisation

4.1.3.1 PIXE (For elemental zoning of composite membranes)

Particle induced X-ray emission (PIXE) analysis is based on the ejection of inner shell electrons from the target atoms as high-energy particles interact with them. When the vacancies are filled by outer shell electrons, the energies involved in the transitions fall in the X-ray region of the electromagnetic spectrum. The X-ray energies are characteristic for the elements and the X-ray intensities are proportional to the number of atoms present in the sample. Hence, the sample elements may be identified and their concentration deduced from a characteristic X-ray spectrum

From the PIXE scan (Fig. 4.9) and the resulting elemental map (Fig. 4.10) it was possible to identify the Titanium (Ti) component in the Titanium dioxide (TiO_2), as well as see its distribution over the TM.

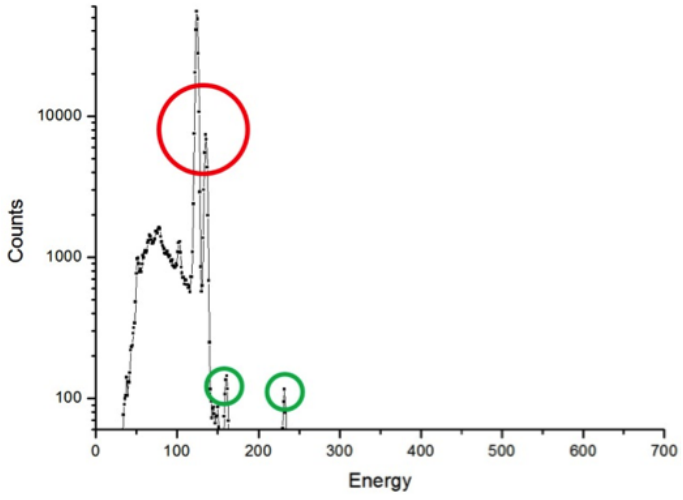

Figure 4.9: PIXE scan of TiO_2-TM.

The red ring indicates a double Ti peak. However, this is only due to the k-alpha and k-beta X-rays. The green rings indicate trace elemental contamination from previous experiments. PIXE cannot give the elemental crystal structure, but it is extremely sensitive to the presence of the elements.

Molar mass of TiO_2 is 79.8658 g/mol. TiO_2 consists of 1 atom of Ti with an atomic mass of 47.867 u and two atoms of O_2 with an atomic mass of 15.9994 u each, resulting in a Ti mass percentage of 59.934%. Therefore, it is necessary to look around the 60% mark on the PIXE elemental map for Ti.

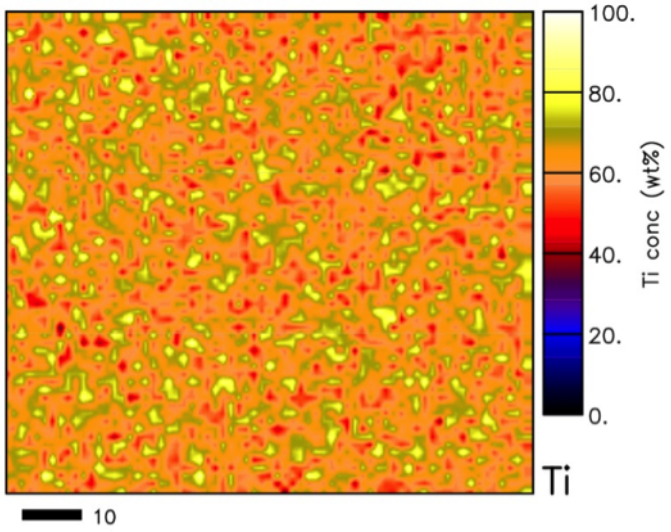

Figure 4.10: PIXE elemental map for the Ti in TiO_2.

From the PIXE elemental map in Fig. 4.10 it is possible to see that the Ti component is located in the orange region. A rather homogeneous particle spread was obtained over the TM. A 10 μm scale is indicated in the bottom left hand corner. This PIXE data was obtained from using accelerated hydrogen protons.

4.1.3.2 RBS (For layer thickness and composition analysis)

Some of the TiO_2 films were analysed by RBS in order to obtain another measurement of the thickness of the samples, besides their chemical composition (stoichiometry). Samples were bombarded with helium ions in order to obtain the data. The depth profiles of the elements were extracted and from the data it was possible to simulate those depth profiles using SIMNRA [196], as can be seen in Fig. 4.11.

The RBS spectra and the way in which the graphs fit indicates that the films were homogeneous along depth, as shown by the plateau in the Ti distribution profile. The thickness of the films, d, was determined from the number (Nd) of atoms per unit area of the film (3.2.3), for which we can calculate the atomic density as

$$N = N_{av}\frac{\rho}{M}, \tag{4.1.1}$$

where N is the number of molecules/cm^3, ρ is the density in g/cm^3, M is the molecular mass in g/mol and N_{av} is Avogadro's constant (6.022×10^{23}/mol).

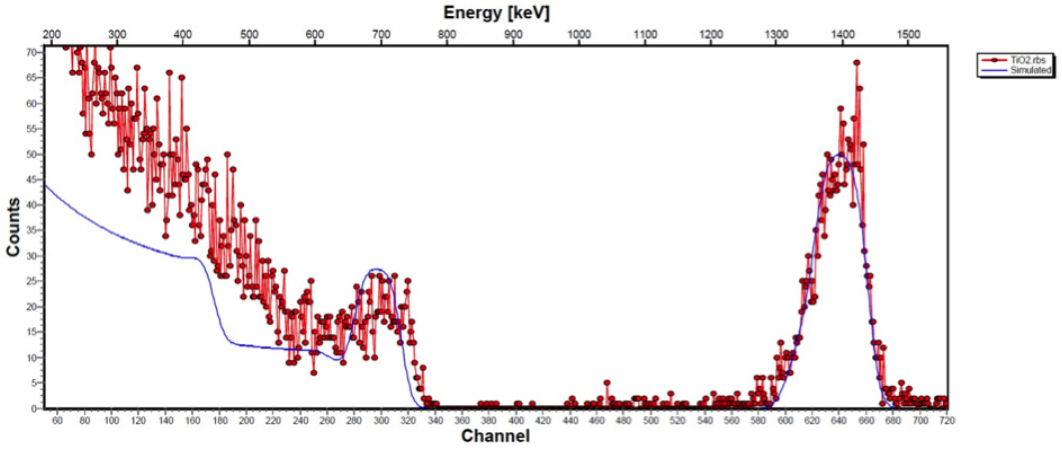

Figure 4.11: RBS spectrum and SIMNRA simulation of TiO_2-TM.

For ρ=4.12 g/cm^3 the atomic density is calculated as N=3.106×10^{22} molecules/cm^3. Since the TiO_2 molecule contains 3 atoms, we can calulate that N_{total}=9.319×10^{22} atoms/cm^3.

The composition of the films show a slight oxygen excess and the data collected was from the last run before the RBS machine was shut down for maintenance, due to some vibrations and minor variations in charge collection measurements. The results of the simulations are summarised below:

$$\begin{aligned} \text{[Ti]:[O]} &= 0.25 : 0.75 \\ Nd &= (1160 \times 10^{15}\ \text{cm}^2).d \\ d &= 31.1\ \text{nm} \end{aligned}$$

The best fit of the spectra recorded was obtained by considering an interfacial layer. However, this makes the simulation exponentially more complicated as there is an excess of unknown variables. It was not possible to identify the chemical composition of this layer with 100% accuracy, therefore its origin remains unknown.

4.1.4 Optical methods used for composite track-etched membrane characterisation

4.1.4.1 UV-VIS (For bandgap analysis)

The transmission and optical bandgap of the TiO_2 films were investigated. Transmittance spectra in the UV-VIS-NIR range (250 to 1100 nm) were measured. One set of the results are illustrated in Figures 4.12 and 4.13.

The optical bandgap energy was investigated by using the transmittance curves and the procedure described in Chapter 3.

Method 1

From (3.2.6), the bandgap energy should have been calculated from the optical absorbance measurements, but in this work, the maximum transmittance and the minimum absorbance are considered at the same wavelength, because the semiconductor

reflectivity is constant at this wavelength. As is evident from Fig. 4.12, the transmittance of the TiO_2 covered TM is much lower than that of the TM on its own. This makes it hard to plot along the exponential transmission line, however, these graphs were only superimposed after measurements were taken to illustrate the difference in transmittance. This will be discussed further in the following section.

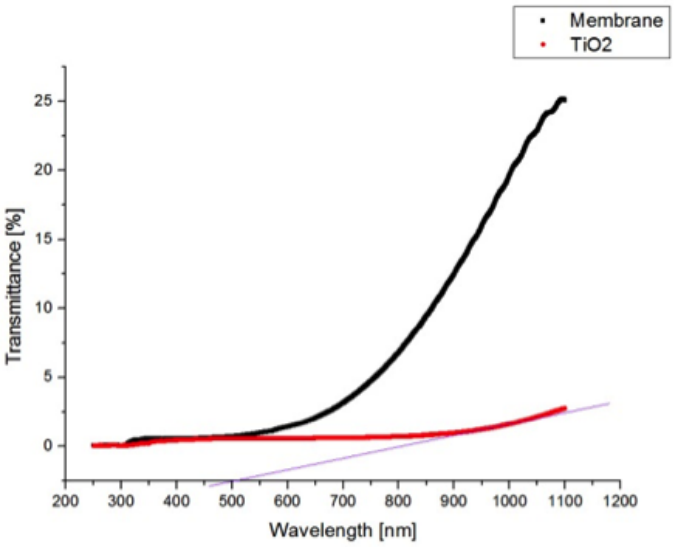

Figure 4.12: Method 1 (basic).

By making use of a linear fitting method the intersection with the abscissa at λ=500 nm is obtained, which corresponds to E_g=2.48 eV. This method was initially only applied to give a rough estimate of the bandgap, whilst measuring the spectra. It is known from the literature that the most recorded bandgap values lie in the 2.7 to 3.4 eV range.

Method 2

A more accurate bandgap approximation can be derived by transforming the measured optical transmittance curve by using (3.2.5). By extrapolating the linear part of the exponential region to zero, the value of the bandgap energy is obtained, as shown in Fig. 4.13. This gives E_g=3.05 eV, which corresponds to a wavelength of approximately 407 nm. This shows just how sensitive these measurements can be as the results from method 1 and 2 are of the same sample..

4.2 Second Approach - Ag-TiO_2 surface modified TM using thermal evaporation in conjunction with ICM sputtering

Fig. 4.14 shows a virtual cross-section of how the TM looks like before and after modification.

The first step in Approach 2 is that of thermal evaporation, in which a thin layer of silver gets deposited over the TM surface. However, before Ag deposition could

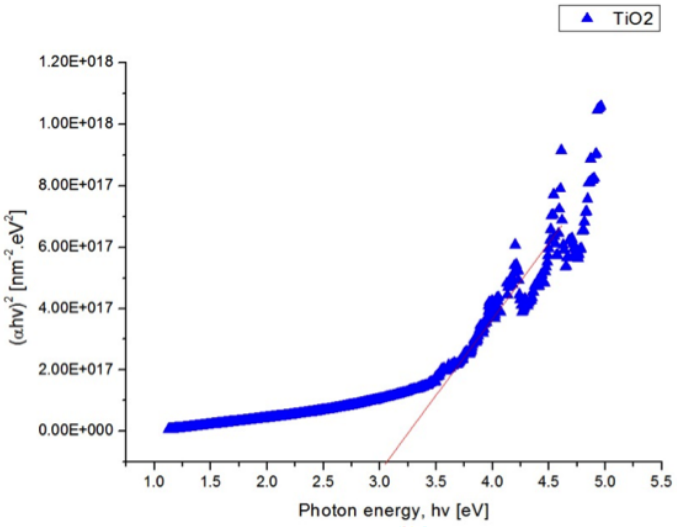

Figure 4.13: Method 2 (advanced).

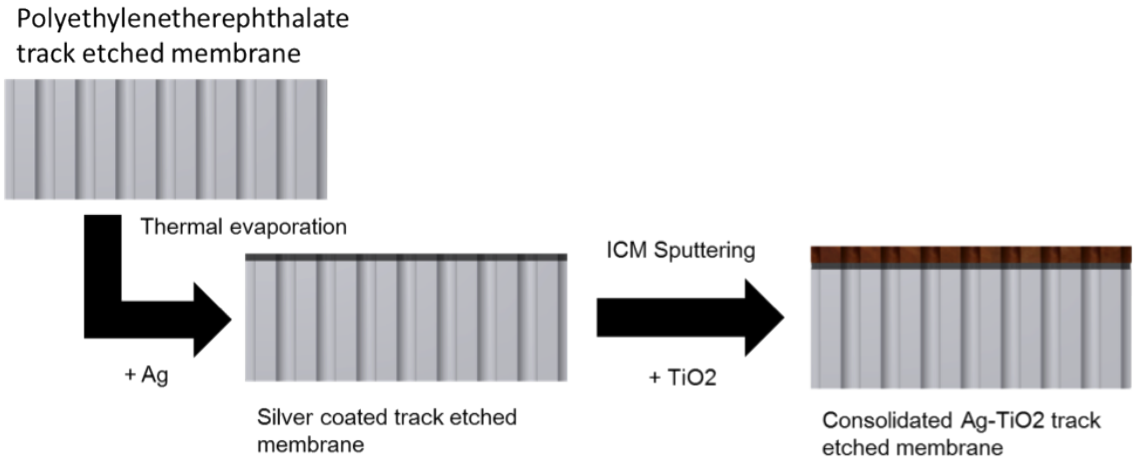

Figure 4.14: Ag-TiO_2 surface modified track-etched membrane, using thermal evaporation in conjunction with inverted cylindrical magnetron sputtering.

commence, as in Approach 1, certain parameters needed to be fixed in order for future experiments to be repeatable.

The film properties can be regulated by adjusting various deposition parameters. The following aspects need to be considered when evaporating:

- The purity of the film is directly proportional to the purity of the source material;
- Pressures below 10-5 torr are required to ensure a straight line path for evaporated species;
- A good vacuum is required for contaminate free deposition;
- The substrate temperature influences a film's crystallinity;
- Quartz Crystal Microbalance calibration determines the measured deposition rate.

Ag deposition parameters	To start system
Vacuum	2×10^{-6} torr
Z-factor (Acoustic impedance)	16.69
Tooling factor	1.61
Sensor life	¿76%
Current	44 A (min)
Cooling	On

Table 4.2: Thermal evaporator parameters

Finally, after some experimentation, the following parameters, shown in Table 4.2, were determined. The reason for choosing these specific parameters was as follows:

- The better the vacuum, the better the layer quality when thermally evaporating. The best operating vacuum that was obtained, after an hour of pre-deposition vacuum pumping, was 2×10^{-6} torr.
- The QCM was used to control the deposition rate and thickness of the deposited material inside the thermal evaporator in real time. From (3.1.1) and (3.1.2) the Z-factor, according to the systems acoustic impedance, and the t-factor, relating to the internal positioning, could be calculated and used to calibrate the QCM. Sensor life decreases over time as more depositions get done. After every 5% to 10% loss of sensor life, the system needs to be re-calibrated. For sensor lifetimes below 75%, they are used for qualitive rather than quantitive analysis.
- The current needs to be applied slowly in order not to damage the tungsten boat housing the silver. By slowly heating the silver and using a low deposition rate (2 Å per second) one gets a better layer surface finish. Rule of thumb, for every 1 nm deposited, one should load the boat with 1 mg of silver. By making use of a Peltier cooler or large aluminium sample holder to act as a heat sink, the chance of thermal shock during deposition is reduced and layer quality thus improved.

A big hindrance to physically handling small sections of track-etched membranes in the laboratory is their predisposition for static electricity. They literally have an affinity for every surface they come in contact with. Secondly, before depositing anything on the substrate surface, it first needs to be cleaned and sterilised. Initially sample preparation consisted of a combination of acetone, ethanol and deionised water wash. After some investigation regarding the properties of plasma and sputtering, an experimental hand held cold plasma gun was built. The idea of using cold plasma as a pre-treatment was conceived. Cold plasma not only worked as a temporary de-static-tiser, but inactivates contaminating microbes and removes dust particles. The designed cold plasma gun eliminated the need for the time consuming acetone, ethanol and deionised water wash. (See materials and methods for more detail on cold plasma gun).

4.2.1 Morphological properties (SEM & AFM)

Fig. 4.15 shows a SEM image, taken at the *Joint Institute for Nuclear Research* (JINR) in Russia, of the silver coated polyethylene terephthalate track-etched membranes used

in this study. Under thirty thousand times magnification it is easy to see the pores and their distribution over the membrane. In comparison with the untreated TM shown in Fig. 4.2, it is clearly visible that the pore size has reduced slightly, and as Ag is conductive, there is less charge build-up visible in the SEM image.

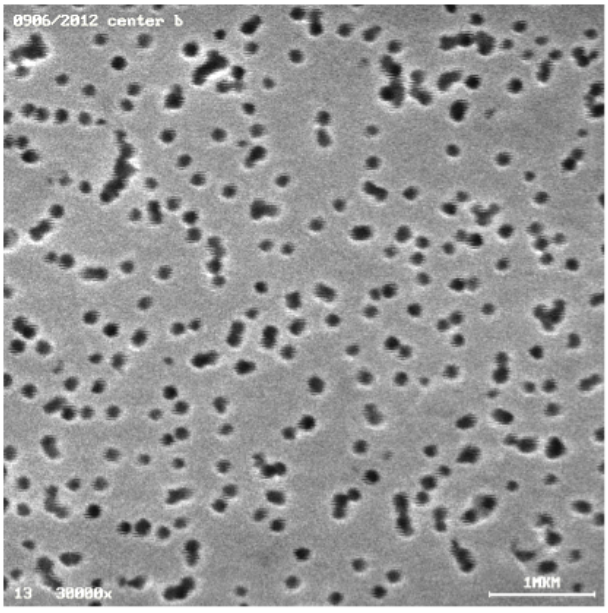

Figure 4.15: Silver coated TM.

It is important to note that even though a layer of around 185 Å of silver was deposited on top of the TM, the pores are not being blocked. The permeability of the TMs will be discussed at the end of the chapter.

For this part of the study, the main use of the AFM was to calibrate the quartz crystal microbalance. By solving for the tooling factor one can easily determine the evaporated silver deposition rate in real time, through the QCM monitoring.

The Rubylith method, as previously described in Approach 1, was applied to form a "step-edge" that could be measured by an AFM in tapping-mode, with a non-contact tip, as seen in Fig. 4.16. From this data the tooling factor, as defined by (3.1.2), can be calculated as 1.61, thereby completing the QCM calibration.

4.2.2 Advanced nuclear methods for material for composite track etched-membrane characterisation

4.2.2.1 PIXE (For elemental zoning of composite membrane)

During the first part of Approach 2 a thin film of pure silver was thermally evaporated over the entire TM surface. PIXE was applied to determine the actual silver distribution and uniformity of this layer.

Silver is a metallic chemical element, and although the intention was only to thermally evaporate pure silver, trace elements such as copper, lead and zinc might be present due to the quality of the silver metal received from the suppliers. This is

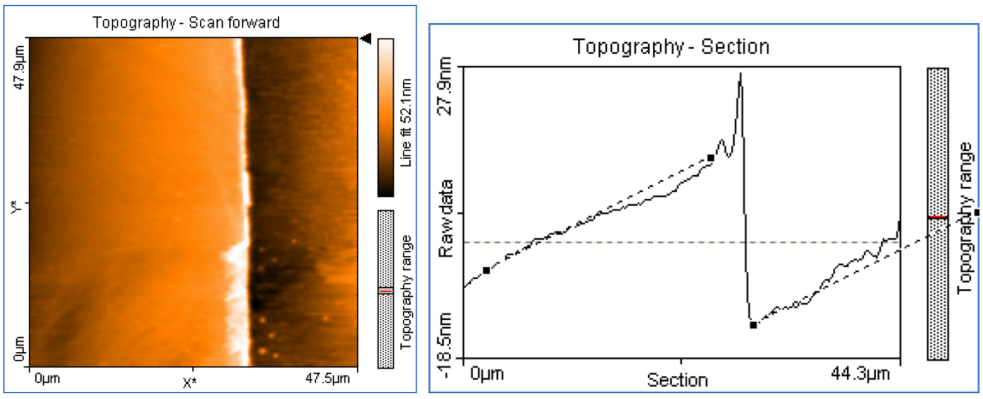

Figure 4.16: Rubylith™step-edge calibration method - Ag on Si.

confirmed in Fig. 4.17, where the red ring indicates Ag and the green ones the trace element contaminants.

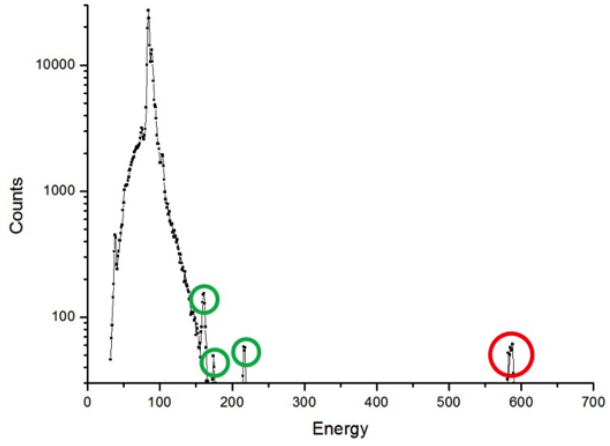

Figure 4.17: PIXE scan of Ag-TM.

The molar mass of Ag is 107.8682 g/mol. Pure Ag consists of 1 atom, therefore it is necessary to look around the 100% mark on the PIXE elemental map for Ag.

From the PIXE elemental map in Fig. 4.18 it can be seen that the Ag concentration is highest in the yellow/white region. The particle spread looks to be rather homogeneous over the layer. However, small defects are visible, but seeing that the TM support is full of pores, it could be that the PIXE is merely identifying some of those pores as a reduction in Ag concentration. A 10 μm scale is indicated in the bottom left hand corner. The PIXE data was obtained from using accelerated hydrogen protons.

4.2.2.2 RBS (For layer thickness and composition analysis)

Some of the Ag films were analysed by RBS in order to obtain another measurement of the thickness of the samples, in order to compare with the results obtained by QCM. Samples were bombarded with helium ions to obtain this data. The depth profiles of the elements were extracted from the data using the simulation program RUMP [197], as can be seen in Fig. 4.19.

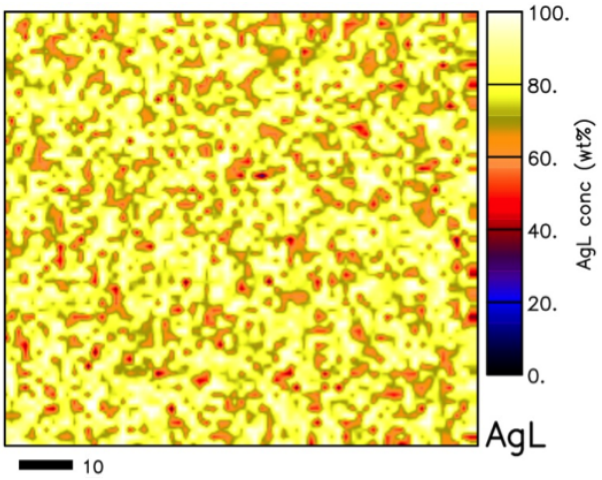

Figure 4.18: PIXE elemental map for silver.

The RBS spectra and their fits indicate that the films are homogeneous with regard to depth. The thickness of the films (d) was determined from (3.2.3) and (4.1.1).

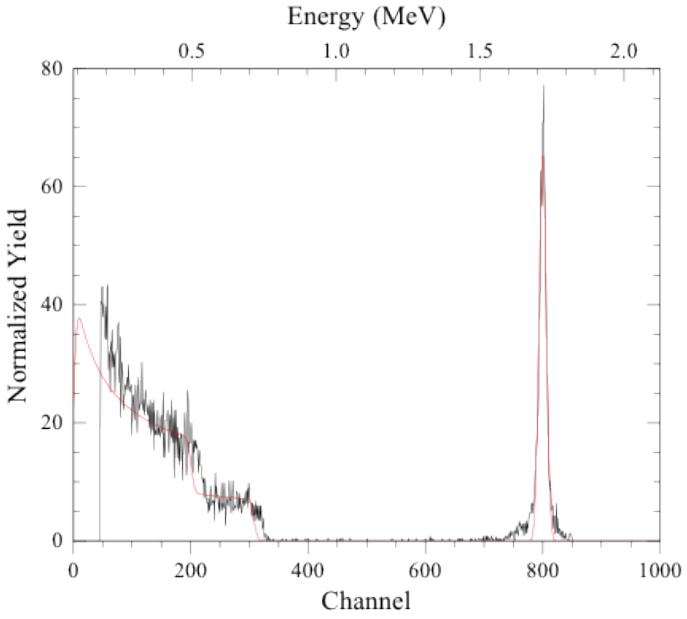

Figure 4.19: RBS spectrum (black) and RUMP simulation (red) for Ag-TM.

For ρ=10.49 g/cm^3, the atomic density is calculated as N=5.856×10^{22} atoms/cm^3. The results of the simulations are summarised below:

$$\begin{aligned} [\text{Ag}] &= 1 \\ Nd &= (110 \times 10^{15}\ \text{cm}^2).d \\ d &= 18.7\ \text{nm} \end{aligned}$$

The thickness of the silver is 1.3 nm less than QCM prediction.

TiO_2 deposition parameters	To start system	To run system
Voltage (NB start)	650 V (min)	385 V
Power (NB running)	135 W	125 W
Current	0.5 A	0.325 A
Gas Ar/O_2 (from cylinder)	350 kPa	350 kPa
Gas Ar (in sputter chamber)	40 mmHg	40 mmHg
Gas O_2 (in sputter chamber)	0 mmHg	10 mmHg
Time	0 min	45 min
Frequency	21 kHz	21 kHz
Duty cycle	80%	80%
Substrate-to-target distance	50 mm	50 mm
Substrate temperature	17°C	30°C

Table 4.3: Sputter parameters

When looking closely at the silver peak in Fig. 4.19, one notices a fringing around its base. This is most likely due to silver particles impregnating the TM pores during deposition. The best fit of the spectra recorded was obtained by considering an interfacial layer. This would also explain why the calculated layer thickness is less than that measured by the QCM. However, this makes the simulation exponentially more complicated, as one has an excess of unknown variables. It was not possible to identify the chemical composition of this layer with 100% accuracy, therefore its origin remains unknown.

4.3 PET + Ag + TiO_2 - Second step in Approach 2

The second step in Approach 2 is the TiO_2 deposition by inverted cylindrical (ICM) sputter on top of the silver coated TMs. As in Approach 1, certain parameters needed to be fixed in order for future experiments to be repeatable (see Table 4.3). The film properties can be regulated by adjusting various sputter parameters (see Approach 1 for detailed description).

4.3.1 General methods used for composite track-etched membrane characterisation

4.3.1.1 Morphological properties (SEM & AFM)

Fig. 4.20 shows a SEM image, taken at the *Joint Institute for Nuclear Research* (JINR) in Russia, of the modified polyethylene terephthalate track-etched membranes used in this study. Under thirty thousand times magnification it is easy to see the pores and their distribution over the membrane, even though they have been coated with both silver and TiO_2. In comparison with the untreated TM shown in Fig. 4.2, it is clearly visible that the pore size has reduced, but not constricted.

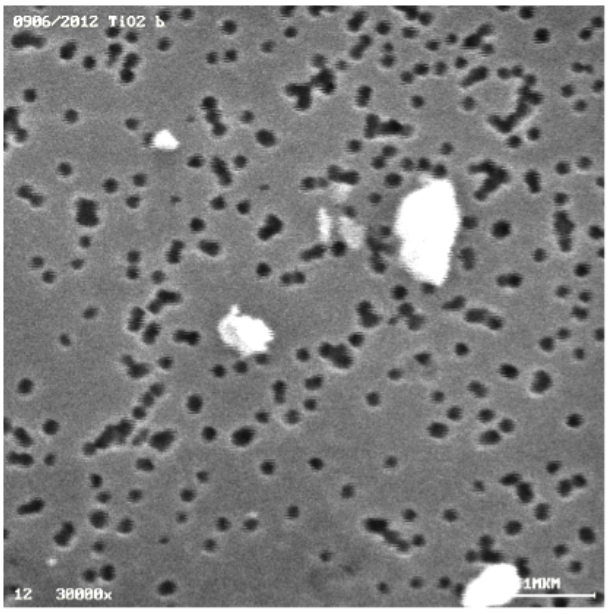

Figure 4.20: Ag-TiO_2-TM track membrane with pore diameter of 0.1 μm and 12 μm thick.

After irradiating the membrane for 48 hours under UV light, it became almost glass-like. The silver layer was not enough to protect the polymer against such intense UV irradiation. Figure 4.21 shows the cross section of the Ag-TiO_2 TM that was made possible by snapping this over-irradiated sample and placing it under the SEM for inspection.

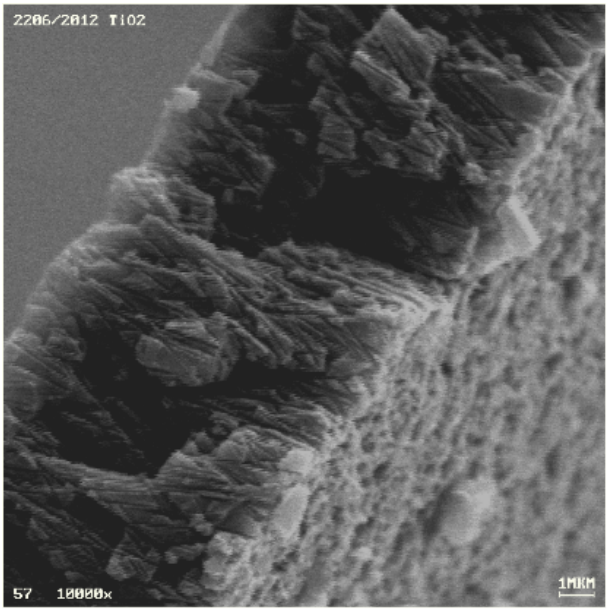

Figure 4.21: Ag-TiO_2-TM track-membrane cross section.

As the AFM was already used to compile a calibration curve for TiO_2 in the previous method, only surface roughness was considered in this section. The average surface roughness obtained was in the 10 nm range, Fig. 4.22 shows one such AFM view.

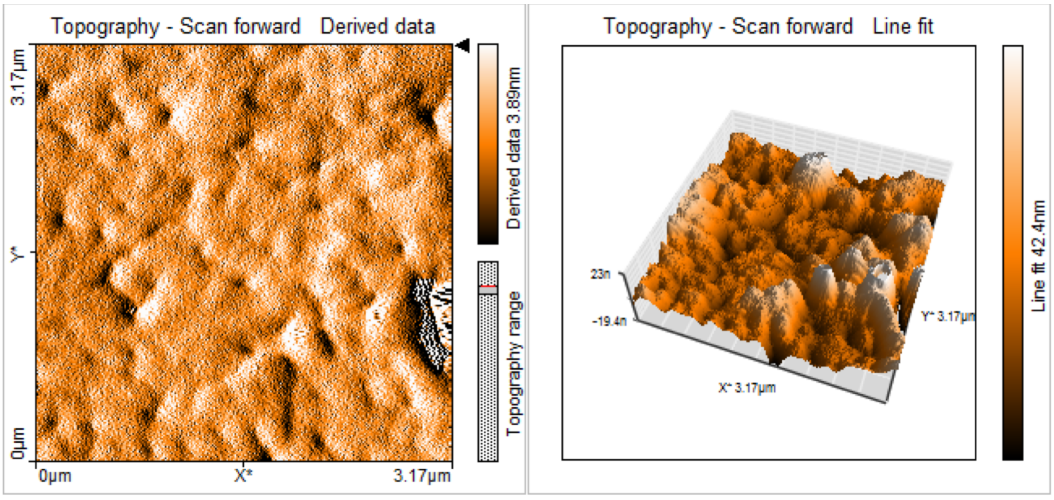

Figure 4.22: AFM Ag-TiO_2-TM surface view.

4.3.2 Structural properties (XRD, IR & FTIR)

4.3.2.1 IR, FTIR (For chemical bond analysis)

Fourier transform infra-red spectroscopy (FTIR) gives information about the vibrational energy of the molecules in a sample, i.e. absorbance in the infrared region. Changes involving groups with strong absorbance in the IR-region, e.g. carboxylic groups, can easily be seen in an FTIR experiment. If the carboxylic group binds to another species, the vibration energy would change and intensity in the carboxylic range would decrease proportional to the ratio of bound functional groups.

The FTIR study shows the bonds between elements in the structure of materials. For TiO_2 it is necessary to test between 80 cm^{-1} and 1500 cm^{-1} (especially the 100 - 850 cm^{-1} region), as shown in Fig. 4.23. During this stage of the study we were only interested in the presence of the bonds. For future analysis in distinguishing the TM, absorption of water and TiO_2, it would be advised to use Raman Spectroscopy instead of FTIR.

4.3.2.2 XRD (For crystallinity study)

A typical XRD pattern of the Ag-TiO_2 films measured by a $2\theta/\theta$scan is shown in Fig. 4.24. The data shows one large wide peak around (111), that possibly masks a second weaker peak at (210), with diffraction indices at angles of 25.75° and 25.4° respectively.

The grain size (D) of the samples was determined from the peak positions and full width at half maximum (FWHM), shown in Fig. 4.24, of the XRD peaks, by using the Scherrer equation (3.2.2).

The FWHM can be measured from Fig. 4.24 (195 in this instance), as well as $2\theta'$ (25.393°) and $2\theta''$ (26.667°), by choosing k=0.94 (for spherical particles) and λ = 1.505Å (for CuK_α radiation). The grain size for the sample is calculated as 6.5 nm, which is consistent with the literature (Fig. 3.22).

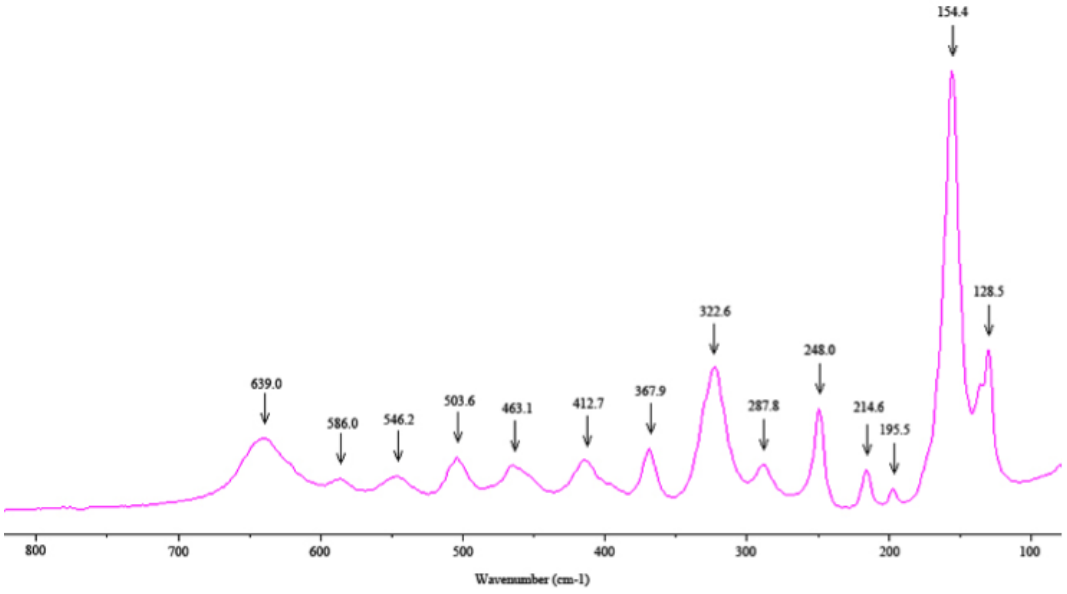

Figure 4.23: Bottom end of FTIR spectrum.

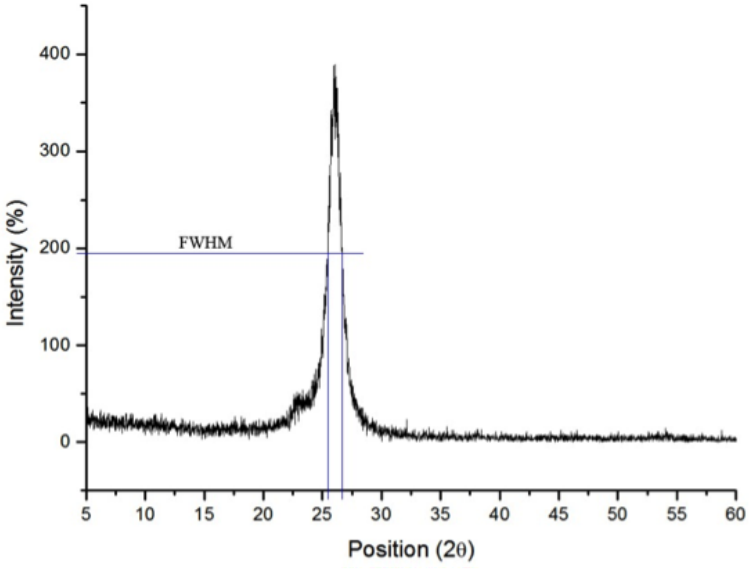

Figure 4.24: Ag-TiO_2-TM XRD showing the Scherrer equation FWHM.

4.3.3 Advanced nuclear methods for material for composite track-etched membrane characterisation

4.3.3.1 PIXE (For elemental zoning of composite membrane)

During the second part of Approach 2 a thin film of TiO_2 was sputtered over the silver coated TM surface. PIXE was applied to determine the actual silver and TiO_2 distribution and uniformity of this nanocomposite layer.

From the PIXE scan and the resulting elemental map, the Silver (Ag) can be identified. The particle distribution over the TM that has been thermally evaporated can also be observed, as well as the Titanium (Ti) component in the Titanium dioxide

(TiO_2), that was sputtered over the silver.

Even though pure metallic silver was thermally evaporated, trace element contaminants found in the source material will show up in the PIXE analysis. Figure 4.25 indicates these contaminants in green. The big double peaks circled in red identify the Titanium (Ti) component in the Titanium dioxide (TiO_2), as well as the much smaller silver peaks further down the spectrum.

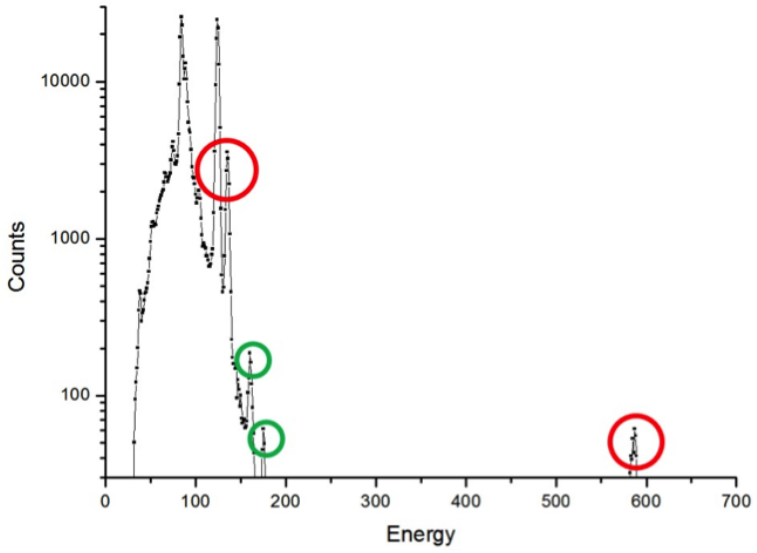

Figure 4.25: PIXE elemental map for the Ag and Ti in Ag-TiO_2.

The molar mass of Ag is 107.8682 g/mol. Pure Ag consists of 1 atom, therefore we need to look around the 100% mark on the PIXE elemental map for Ag. On the other hand, the molar mass of TiO_2 is 79.8658 g/mol. TiO_2 consists of 1 atom of Ti, with an atomic mass of 47.867 u, and two atoms of O_2, with an atomic mass of 15.9994 u each, resulting in a Ti mass percentage of 59.934%. Therefore, we need to look around the 60% mark on the PIXE elemental map for Ti.

From the PIXE elemental map in Fig. 4.26 we can see that the Ag is located in the yellow/white region. The particle spread looks to be a rather homogeneous over the layer. However, small defects are visible, but seeing that the TM substrate is full of pores, it may well be that the PIXE is merely identifying some of those pores as a reduction in Ag concentration.

From the PIXE elemental map in Fig. 4.27 we can see that the Ti component is located in the orange region. We can see a rather homogeneous particle spread over the layer. Comparable to the previous map, a few small defects are visible. Once again, it is most likely that the PIXE is merely identifying some of those pores as a reduction in Ti concentration. A 10 μm scale is indicated in the bottom left hand corner. The PIXE data was obtained from using accelerated hydrogen protons.

4.3.3.2 RBS (For layer thickness and composition analysis)

Some of the Ag-TiO_2 nanocomposite films were analysed by RBS in order to obtain another measurement of the thickness of the samples, for comparison with the results

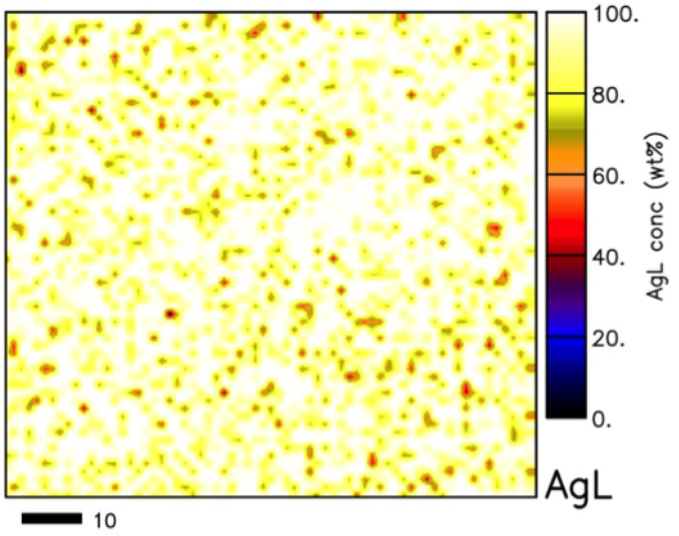

Figure 4.26: PIXE elemental map for the Ag in Ag-TiO_2.

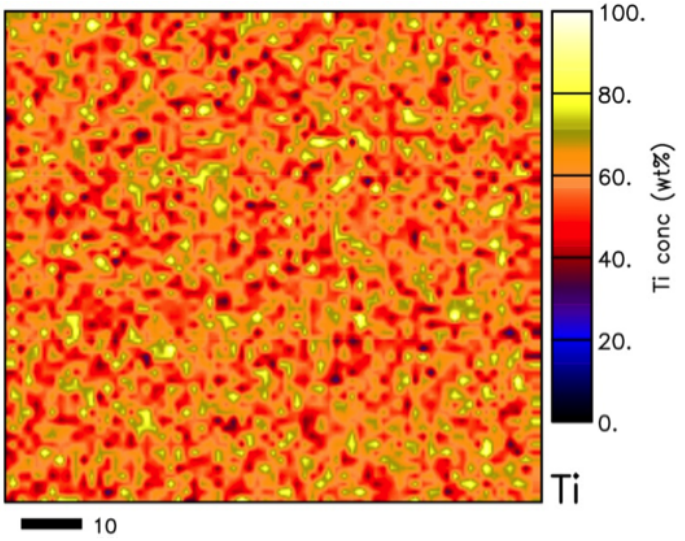

Figure 4.27: PIXE elemental map for the Ti in Ag-TiO_2.

obtained by QCM and the rubylity calibrated ones. Secondly, the sample thinness could be compared with the previous single layer Ag and TiO_2 deposited films. This will give an indication whether the sputter of TiO_2 affected the initial Ag layer, or if the Ag had an effect on the TiO_2 deposition. Samples were bombarded with helium ions in order to obtain the data. The depth profiles of the elements were extracted from the data using the simulation program RUMP [197], as can be seen Fig. 4.28.

The RBS spectra and their fits indicate that the films are homogeneous with regard to depth. The thickness of the films (d) was determined from (3.2.3) and (4.1.1).

Unlike the previous layer, where an approximate fit could be found with individual layers, the nanocomposite Ag-TiO_2 films required that interfacial layers had to be added. This makes the simulation much more complicated due to the large number of unknown variables.

The results of the simulations are summarised below, with ρ_{silver}=10.49 g/cm^3, giv-

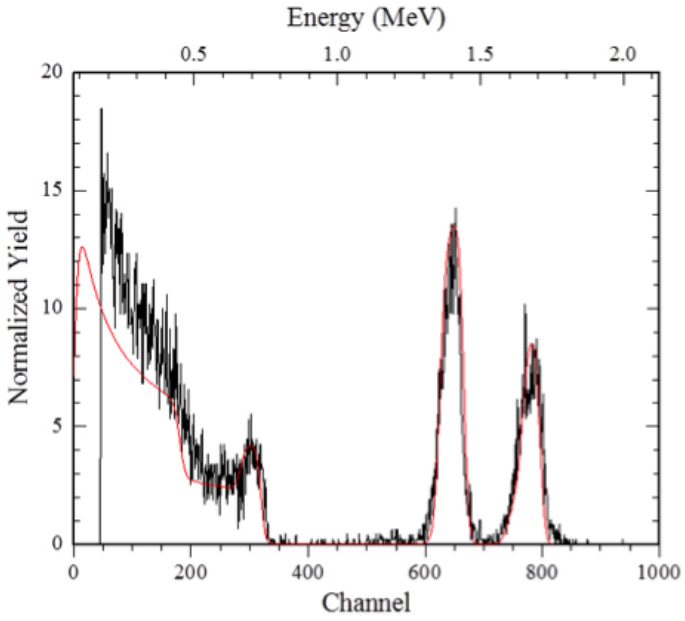

Figure 4.28: RBS spectrum (black) and RUMP simulation (red) for Ag-TiO_2-TM.

ing N=5.856×10^{22} atoms/cm^3, and ρ_{TiO_2}=4.12 g/cm^3, giving N= 9.319×10^{22} atoms/cm^3:

Layer 1

[Ti]:[O]=1:2
Nd=(235×10^{15} cm^2).d
d=25.2 nm

Layer 2

[Ti]:[O]:[Ag]=0.87:2:0.13
Nd=(669×10^{15} cm^2).d
d=62.5 nm

Layer 3

[Ag]:[O]:[C]:[H]=0.1:4:10:8
Nd=(1098×10^{15} cm^2).d
d=18.8 nm

From this data, it is difficult to tell how thick the individual layers are, however, it can be said that a small outer TiO_2 film exists, with a much larger amount of the TiO_2 imbedded into the encapsulated Ag layer. The Ag layer is imbedded into the underlying substrate.

4.3.4 Optical methods used composite track-etched membrane characterisation

4.3.4.1 UV-VIS (For bandgap analysis)

The transmission and optical bandgap of the TiO_2 films were investigated. Transmittance spectra in the UV-VIS-NIR range (250 to 1100 nm) were measured. One set of the results are processed in Fig. 4.29 and Fig. 4.30.

The optical bandgap energy was investigated by using the transmittance curves and the procedure described in Chapter 3.

Method 1

From (3.2.6), the bandgap energy should have been calculated from the optical absorbance measurements, but in this work, the maximum transmittance and the minimum absorbance are considered at the same wavelength, because the semiconductor reflectivity is constant at this wavelength. As is evident from Fig. 4.29 the transmittance of the Ag-TiO_2 covered TM is much higher than that of TiO_2 on its own, shown in Fig. 4.12. However, it is still lower than that of the untreated TM.

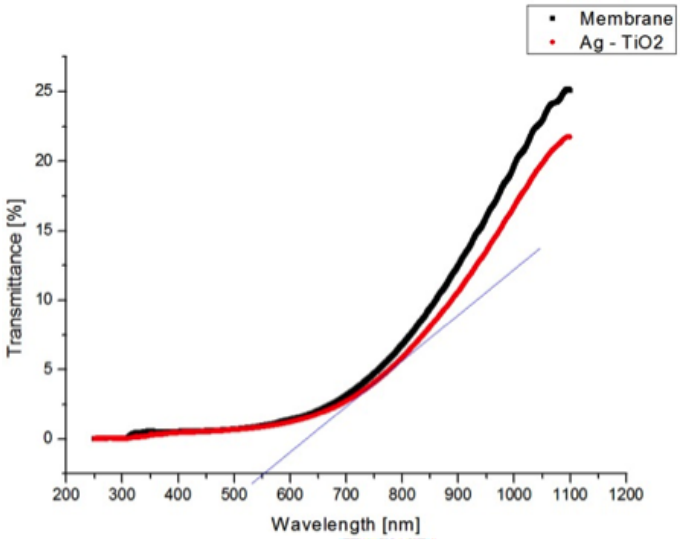

Figure 4.29: Method 1 (basic).

By making use a linear fitting method, an intersection with the abscissa at λ=550 nm is obtained, which corresponds to E_g=2.257 eV. This method only gives a rough estimate of the bandgap during the measurement of the spectra. It is known from the literature that the most recorded bandgap values lie in the range from 2.7 to 3.4 eV range.

Method 2

A much more accurate bandgap approximation can be derived by transforming the measured optical transmittance curve by using (3.2.5). By extrapolation of the linear

part of the exponential region to zero, the value of the bandgap energy is obtained, as shown in Fig. 4.30. The bandgap is approximated as E_g=3.05 eV, which corresponds to a wavelength of 407 nm.

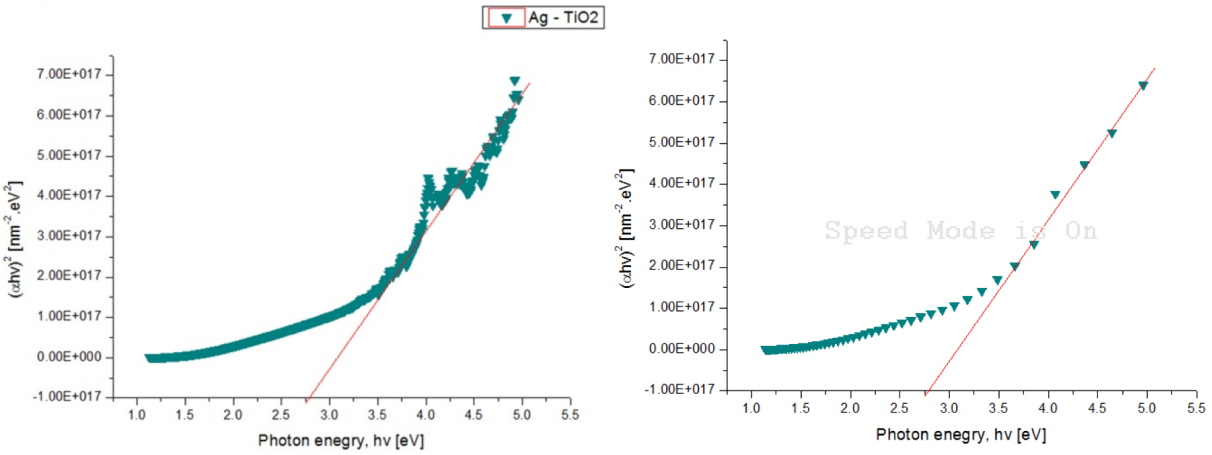

Figure 4.30: Method 2 (advanced).

4.3.4.2 Self-cleaning properties of Ag-TiO_2 TM (Dye degradation)

For the self-cleaning test 100 ppm Rhodamine 6G dye was allowed to degrade over an hour under UV irradiation at 355 nm. Transmittance measurements were taken every 10 minutes at the 550 nm peak that Rhodamine 6G shows under UV-VIS. Both the cross-flow (Fig. 4.31) and dead-end (Fig. 4.32) reactors were used for the analysis. The dead-end reactor seemed to give slightly better results.

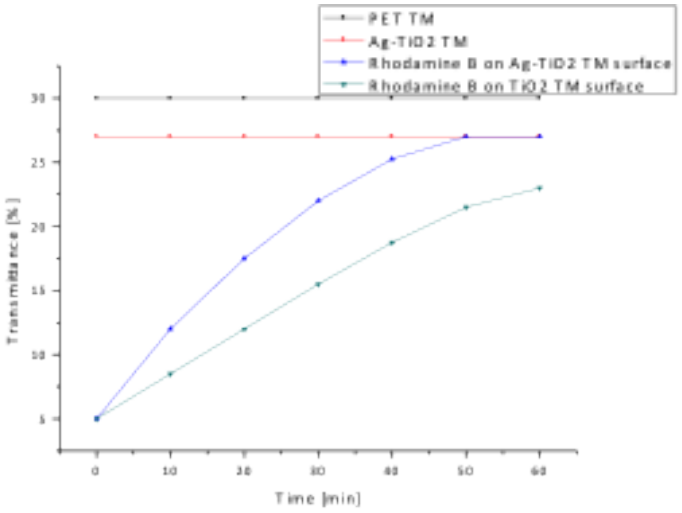

Figure 4.31: Cross-flow reactor results.

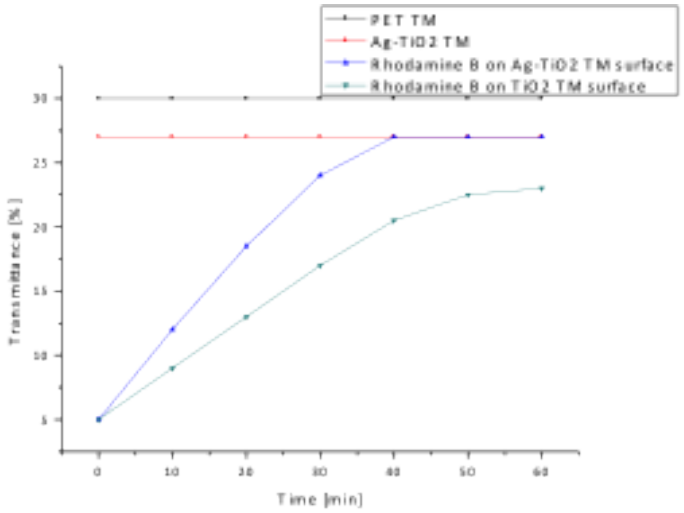

Figure 4.32: Dead-end reactor results.

Parameters	Modified membrane (Ag+TiO_2)	Modified membrane (Ag+TiO_2) + UV	Standard membrane	Standard membrane + UV
Permeability ($ml/min/cm^2$)	0.64	0.8	0.56	0.6

Table 4.4: Increased efficiency of 0.1 μm modified TM with pore density of the order F=10^7 cm^{-2}

100% of the Rhodamine 6G dye that collected on the Ag-TiO_2 TM surface was degradated after 40 min of UV irradiation, proving the modified TM's regenerative ability.

4.4 Flow rate tests

The flow rate of the unmodified TMs was finally compared to the modified TMs. Upon completion of the analyse, it was clear that there was a definite reduction in the average pore size due to the layers deposited on top of the TM surface. However, due to the superhydrophilic surface generated during UV irradiation, the permeability of the TMS was increased. The average values of a batch of tests are given in Table 4.4.

Chapter 5

Conclusions

The overall conclusions of the thesis are consolidated in this chapter. Recommendations for future research are presented thereafter.

The purpose of this study was to develop modified track-etched membranes, using photocatalytic semiconductors for advanced oxidation water treatment processes. To achieve this goal, two approaches were followed.

The first approach in photocatalytic membrane development was to directly modify the PET TM surface with TiO_2, using inverted cylindrical reactive magnetron sputtering for TiO_2 thin film deposition. In parallel with this approach it was to try a second approach, by first coating the TM surface with Ag through thermal evaporation, followed by TiO_2 inverted cylindrical reactive magnetron sputtering to produce a noble metal-titania nanocomposite thin film layer on top of the TM surface.

Therefore, a system for TiO_2 deposition on polymeric films were developed. This system was based on the adopted components of the original dc-magnetron sputtering setup, that was constructed at the Department of Electrical and Electronic Engineering at Stellenbosch University for thin film YBaCuO research. This system could initially not deposit TiO_2.

For TiO_2 deposition on polymers the dc-magnetron was modified:

- The dc power supply was replaced by a pulsed-dc power source, which allowed for the deposition of non-conductive oxides and provided a large enough output voltage to ignite the TiO_2 plasma.
- A cooling system was created, utilising both water and Peltier cooling to keep the TM at 30°C during deposition, thereby preventing the polymer from melting.

A method of reactive magnetron sputtering of TiO_2 on TM was developed:

- The Ar:O_2 gas mixture in the reactive chamber was optimised.
- It was found that the percentage of O_2 in the mixture had to be in the range from 10-30%.

TiO_2 films ranging from 35 to 55 nm was deposited on the surface of TM with 0.1 to 0.4 μm pores. Average pore diameters across the TM foils were confirmed with an

Excel-program, based on the student-t-distribution.

The physicochemical properties of the TiO_2 films were studied:

- Scanning Electron Microscope studies revealed that the surface finish of Ag-TiO_2 layers were much smoother than the TMs covered in TiO_2 only.
- The Atomic Force Microscope was used to calibrate the deposition rates and showed that surface roughnesses for Ag-TiO_2 layers were of the order 6-10 nm.
- X-ray Diffraction crystalinity studies showed that the initial TiO_2 layer was of an amorphous consistency, but subsequent Ag-TiO_2 layers resulted in a brookite structure, with a crystallite size of 6.5 nm.

For Ag deposition calibration of Ag-thin films were done using a "step-edge" technique. By replacing the previous photoresist method by Rubylith™, and measuring the deposition step formed by AFM, it became much faster and easier to calibrate the quartz crystal microbalance for real time deposition monitoring. According to QCM readings the Ag films ranged between 12 and 20 nm.

From optical analysis the bandgap of the TiO_2 modified TM was calculated (by inserting the Transmission UV-VIS results into an Excel-program) to be 3.05 eV at a wavelength of 407 nm, whereas the Ag-TiO_2 modified TM resulted in an improved bandgap of 2.76 eV at a wavelength of 450 nm.

Two reactors for dye degradation studies of the TM surfaces were designed, namely a cross-flow- and a dead-end reactor. Thereafter, the UV-VIS technique for TM transmittance studies was applied. Rhodamine 6G at 100 ppm was used as a model dye, and measurements were taken round its 550 nm absorption peak.

A technique of using the change in transmission of the TiO_2-TM was used to study the dye degradation on its surface. The changing transmittance values of the modified TMs were studied and showed that, after irradiating by UV (at approximately 350 nm), the percentage transmittance reversed from 5% to 80% in 40 minutes.

Exactly the same techniques were used in studying the dye degradation on the Ag-TiO_2 modified TMs, resulting in a percentage transmittance reversal from 5% to 100% in 40 minutes.

Two methods from nuclear physics were used:

- Firstly, from Proton Induced X-ray Emission (PIXE), the elemental presence in each layer, as well as the composite consistency, were identified, showing individual elemental layers with an even spread across the sample.
- Secondly, from helium ion Rutherford backscattering spectroscopy (RBS), the layer thickness and atoms per cm^2 of each element present in their respective layers were calculated. This was done, because the calibration methods used during deposition did not allow for 100% accuracy. It was found that TiO_2 deposition was slightly faster than originally predicted, but only by 5-10 nm. As for silver, the layer thickness was found to be slightly thinner after TiO_2 sputtering, but once again only by 2-3 nm. It was concluded that sub- or interfacial layers play a vital role in magnetron deposition on polymeric supports.

Recommendations for future research are as follows:

- Investigate the replacement of Physical Vapour Deposition (PVD) techniques with Atomic Layer Deposition (ALD).
- The formation and effect of interfacial layers during both physical vapour and atomic layer deposition should be studied.
- Consider the replacement of Polyethylene terephthalate (PET) with UV-resistant Polyethylene naphthalate (PEN) and experiment with TM protective alumina layers.
- Study the Hall-effect, and the electrical and semiconductor properties of the layers.
- Study super-hydro-philicity of TiO_2 and Ag-TiO_2 layers.
- Study the degradation of proteins, viruses and bacteria on modified polymeric TM surface.

Appendices

Appendix A

ICM Operating Procedures

A.1 Chamber Preparation and Sample Mounting

The same vacuum system is used for the ICM and the Argon ion mill, so the start-up procedures are identical.

1. Close the valves to both the roughing and diffusion pumps and vent the ICM system.
2. Remove power supply cable connections from the ICM-head.
3. Do a physical check of the target. If necessary, use fine sand paper to clean cylindrical target.
4. Check that thermocouple is in place and the temperature controller is set to the correct temperature profile.
5. Clean substrate heater surface before mounting clean MgO substrate.
6. Check that the heater assembly is firmly mounted on the water-cooled base. Centre the heater, using the chamber walls as a reference.
7. Ensure that the heater temperature is below 30°C. Apply a thin layer of silver paste and place the substrate firmly onto the substrate heater.
8. Position the sample on the substrate heater and apply pressure to the edges of the substrate for even coverage of the silver paste.
9. Clean O-rings between chamber and ICM head. Apply a thin layer of vacuum grease.
10. Position the ICM-head onto the deposition chamber.

A.2 Starting a Deposition Process

1. Close the gas valves between the argon and oxygen gas cylinders and open the gas valves on the workbench. This opens up the gas feeds to the vacuum chamber, allowing one to test if there are any leaks in the gas lines.
2. Change the roughing valve to backing position, switch on the diffusion pump and its water-cooling, and wait for 15 minutes.

3. Turn the valve to roughing and switch on vacuum pump. When the pressure has reached 20 Torr, open the diffusion pump valve.
4. Switch high vacuum gauge on. Wait (15 minutes) until vacuum reaches 8×10^{-6} mbar.
5. Close the workbench gas inlet valves and open the primary and secondary valves on both gas cylinders.
6. The diffusion pump is closed during deposition (diffusion pump may be switched off if only one deposition is done). Return the valve position to roughing. The chamber pressure should stabilize at 1×10^{-6} mbar.
7. Set both gas mixtures by adjusting the workbench gas inlet valves (typically 2:1 oxygen to argon) reaching a total pressure of between 150-225 mm Hg.
8. Switch water cooling to ICM, by using the in-line valves, and switch on the water cooling. This cools the magnets and heater. Also check that there are no water leaks.
9. Switch on the temperature controller and wait until a temperature of 740°C has been reached.

A.3 ICM Operation

1. Connect the negative terminal to the copper water cooling pipes, which are the ICM cathode. The positive terminal to the ICM anode, which is the aluminium housing, can also be grounded.
2. Switch on the constant current power supply, and set the voltage to 350 V DC and 40 mA until plasma ignition, thereafter lower the voltage to 200 V DC and slowly increase the current to 400 mA.
3. Sputtering has started and the deposition rate is between 2 nm to 4 nm, depending on the final pressure setting. The deposition thickness is a function of the deposition time.

A.4 Ending a Deposition Process

1. After the deposition, switch off sputtering power supply.
2. Close only the argon workbench gas inlet valve.
3. The temperature profile is set to anneal at 500°C at 3°C per minute.
4. Slowly increase the oxygen flow to the chamber by adjusting the oxygen workbench inlet valve. At 550°C, change the rouging pump valve to backing or forline pump setting. This disables the pump and the oxygen can reach atmospheric pressure.
5. Keep at 500°C during the annealing process. The chamber pressure should now be about 1 bar.
6. The temperature is kept at 500°C for 1 h, thereafter the heater is turned off.

7. Once the heater temperature has reached 300°C, the oxygen workbench gas feed valves, as well as at the gas cylinder, can be closed.
8. Remove DC power supply cable connections from the ICM, and lift off the ICM-head, after substrate heater is at room temperature.

A.5 System Shutdown

1. Replace ICM head on the top vacuum chamber.
2. Turn the main valve to the roughing position. The ICM should always be kept under vacuum if not in use.
3. Close the main valve by positioning either to the forline, or centre position, once sufficient vacuum (100-50 Torr) has been reached.
4. Switch the diffusion pump off, also the roughing pump and the workbench gauges.
5. Return the roughing pump exhaust pipe into the room, and close the window.
6. Wait 20 minutes before turning off the water cooling to the diffusion pump.

Appendix B

Thermal Evaporator Operating Procedures

B.1 Loading Samples

- Set the Vent valve switch to open ("O"). Green LED is on.
- Wait approx. 10 minutes for system to vent (Dome will become loose).
- Carefully place the dome on the black stand next to the machine.
- Set the Vent valve switch to close ("C"). Green LED is off.
- Load the desired material's source boat and sensor crystal.
- Place samples upside down on sample holder and cover source boat with the swing-arm shield.
- Carefully replace the dome, centred on the platform.
- Make sure the Vent valve is closed ("C"). Green LED is off.
- Push "Pumping Unit" button once to start vacuum pump.
- Switch on "Pirani Cold Cathode Gauge" after approx. 10 minutes. **NB: Never switch gauge on if system is not under vacuum!!**
- Wait until system pressure is 2.5×10^{-5} mbar. (Approx. 30 minutes).
- Open water valve for sensor cooling.

B.2 Evaporation procedure

- Open the QPod.exe software and load the desired source material's profile.
- Check that sensor frequency reading is not "XTFAIL". Sensor crystal is not mounted correctly if "XTFAIL" signal is displayed.
- Slowly increase the supply current until material starts evaporating. The current is dependent on the source material.
- Click the "Start button" on the QPod.exe program and turn away the swing-arm shield.

- Evaporate at a rate of approx. 0.5 Å/s for good uniform films
- When desired film thickness (given in kÅ) is achieved, return swing-arm shield to centre position and click "Stop" on the QPod.exe program.
- Slowly reduce the supply current to zero.
- Push "Pumping Unit" button again to stop vacuum pump.
- Switch off the pressure gauge ("Pirani Cold Cathode Gauge").
- Close water valve for sensor cooling.
- Wait until the vacuum turbo pump comes to a complete stop. **NB: Pump must stop completely before opening Vent valve!!**

B.3 Unloading Samples

- Wait until the vacuum turbo pump comes to a complete stop. **NB: Pump must stop completely before opening Vent valve!!**
- Set Vent valve switch to open ("0"). Green LED is on.
- Wait approx. 10 minutes for system to vent. (Dome will become loose).
- Carefully place the dome on the black stand next the machine.
- Set the Vent valve switch to close ("C"). Green LED is off.
- Carefully remove samples without touching the films' surfaces. **NB: Remove the source boat and sensor crystal and store in its labelled container.**
- Carefully replace the dome and store the system under vacuum. (Switch on vacuum pump for approx. 5-10 minutes).

Appendix C

Deposition Materials

Element	Symbol	Melting Point °C	Density (bulk, g/cm3)	Z-ratio	Temperature °C @ Vapor Pressure (Torr)			Evaporation Method	Crucible Key	Boat	Remarks
					10^{-8}	10^{-6}	10^{-4}				
Silicon Monoxide	SiO	1702	2.1	--	--	--	850	eBeam (Fair)	Ta	W, Ta	Baffle box source best for resistance evaporation. Low rate suggested. n = 1.6.
					sublimes						
Silicon Nitride	Si3N4	--	3.44	--	--	--	~800	eBeam, sputter	--	--	n = 2.1
		sublimes									
Silicon Selenide	SiSe	--	--	--	--	--	550	--	Quartz	--	--
Silicon Sulphide	SiS	--	1.85	--	--	--	450	--	Quartz	--	--
		sublimes									
Silicon Telluride	SiTe2	--	4.39	--	--	--	550	--	Quartz	--	--
Silver	Ag	961	10.49	0.529	847	958	1105	eBeam (xlnt), Thermal	Al2O3, Mo	Mo, Ta	Evaporates well from any source.
Silver Bromide	AgBr	432	6.47	--	--	--	~380	--	Quartz	Ta	n = 2.25
Silver Chloride	AgCl	455	5.56	--	--	--	~520	--	Quartz	Mo, Pt	n = 2.07
Silver Iodide	AgI	558	5.67	--	--	--	~500	--	--	Ta	n = 2.21
Silver Iodide	AgI	558	5.67	--	--	--	~500	--	--	Ta	n = 2.21
Sodium	Na	97	0.97	--	74	124	192	--	Quartz	Ta, S.S.	Use gentle preheat to outgas. Metal reacts violently in air.
Sodium Bromide	NaBr	755	3.2	--	--	--	~400	--	Quartz	--	Use gentle preheat to outgas. n = 1.64
Sodium Chloride	NaCl	801	2.16	--	--	--	530	ebeam (Good)	Quartz	Ta, Mo, W	Cu ovens, little decomposition. Use gentle preheat to outgas. n = 1.54
Sodium Cyanide	NaCN	563	--	--	--	--	~550	--	--	Ag	Use gentle preheat to outgas. n = 1.45
Sodium Fluoride	NaF	988	2.79	--	--	--	~700	ebeam (Good)	BeO	Mo, Ta, W	Use gentle preheat to outgas. No decomposition n = 1.30 @ .55µ
Sodium Hydroxide	NaOH	318	2.13	--	--	--	~470	--	--	Pt	Use gentle preheat to outgas. n = 1.36
Spinel	MgO3	--	8	--	--	--	--	ebeam (Good)	--	--	n = 1.72
	5Al2O3										
Strontium	Sr	769	2.6	--	239	309	403	ebeam (Poor)	VC	W, Ta, Mo	Wets but does not alloy with refractory metals. May react violently in air.
Strontium Fluoride	SrF2	1190	4.24	--	--	--	~1000	--	Al2O3	--	n = 1.44
Strontium Oxide	SrO	2460	4.7	--	--	--	1500	--	Al2O3	Mo	Reacts with Mo, and W; n = 1.87
					sublimes						
Strontium Sulphide	SrS	Above 2000	3.7	--	--	--	--	--	--	Mo	Decomposes. n = 2.11
Sulphur	S8	115	2	--	13	19	57	ebeam (Poor)	Quartz	W	Poisons vacuum system.
Supermalloy	Ni/Fe/Mo	1410	8.9	--	--	--	--	ebeam (Good)	--	--	Sputtering preferred; co-evaporate from 2 sources, Permalloy and Mo.
Tantalum	Ta	2996	16.6	--	1960	2240	2590	ebeam (Xlnt)	--	--	Forms good films.
Tantalum Boride	TaB2	3000	12.38	--	--	--	--	--	--	--	--
Tantalum Carbide	TaC	3880	14.65	--	--	--	~2500	--	--	--	JVST 12, 811 (1975)
Tantalum Nitride	TaN	3360	16.3	--	--	--	--	--	--	--	Reactive; evaporate Ta in 10-3N2.
Tantalum Pentoxide	Ta2O5	1800	8.74	--	1550	1780	1920	ebeam (Good)	VC	W, Ta	Slight decomposition; evaporate in 10-3 Torr of O2. n = 2.0 @ 1.5µ App. Opt. 19, 1737 (1980)
Tantalum Sulphide	TaS2	1300	--	--	--	--	--	--	--	--	--

Element	Symbol	Melting Point °C	Density (bulk, g/cm3)	Z-ratio	Temperature °C @ Vapor Pressure (Torr)			Evaporation Method	Crucible Key	Boat	Remarks
					10^{-8}	10^{-6}	10^{-4}				
Technetium	Tc	2200	11.5	--	1570	1800	2090	--	--	--	--
Teflon	PTFE	330	2.9	--	--	--	--	--	--	W	Baffled source. Film structure doubtful.
Tellurium	Te	452	6.25	--	157	207	277	ebeam (Poor)	Al2O3, Quartz	W, Ta	Wets without alloying. Toxic.
Terbium	Tb	1357	8.27	--	800	950	1150	ebeam (Xlnt)	Al2O3	Ta	--
Terbium Fluoride	TbF3	1176	--	--	--	--	~800	--	--	--	--
Terbium Oxide	Tb2O3	2387	7.87	--	--	--	1300	--	--	Ir	Partially decomposes.
Terbium Oxide	Tb4O7	--	--	--	--	--	--	--	--	Ta	Films TbO.
Thallium	Tl	302	11.85	--	280	360	470	ebeam (Poor)	Al2O3, Quartz	W, Ta	Wets freely, very Toxic.
Thallium Bromide	TlBr	480	7.56	--	--	--	~250	--	Quartz	Ta	Toxic n = 2.3
					sublimes						
Thallium Chloride	TlCl	430	7	--	--	--	~150	--	Quartz	Ta	Toxic n = 2.25
					sublimes						
Thallium Iodide (B)	TlI	440	7.09	--	--	--	~250	--	Quartz	--	Toxic n = 2.78
					sublimes						
Thallium Oxide	Tl2O3	717	9.65	--	--	--	350	--	--	--	Toxic, Goes to Tl2O @ 850° C.
Thorium	Th	1875	11.7	--	1430	1660	1925	ebeam (Xlnt)	W	W, Ta, Mo	Toxic, radioactive.
Thorium Bromide	ThBr4	--	5.67	--	--	--	--	--	--	Mo	Toxic n = 2.47 @ 5µ
					sublimes						
Thorium Carbide	ThC2	2773	8.96	--	--	--	~2300	--	Carbon	--	Radioactive.
Thorium Dioxide	ThO2	3050	10.03	--	--	--	~2100	ebeam (Good)	--	--	Radioactive. n = 1.86 @ 2.2µ
Thorium Fluoride	ThF4	1110	6.3	--	--	--	~750	ebeam (Fair)	VC	Mo	Radioactive. n = 1.52 Heat substrate to above 150° C. JVST 12, 919, (1975)
Thorium Oxyfluoride	ThOF2	900	9.1	--	--	--	--	--	--	Mo, Ta	Radioactive. n = 1.52
Thorium Sulphide	ThS2	--	6.8	--	--	--	--	--	--	--	Sputtering preferred; co-evaporate from 2 sources.
Thulium	Tm	1545	9.32	--	461	554	680	ebeam (Good)	Al2O3	Ta	--
					sublimes						
Thulium Oxide	Tm2O3	--	8.9	--	--	--	1500	--	--	Ir	Decomposes.
Tin	Sn	232	7.75	0.724	682	807	997	eBeam (Xlnt), Thermal	Al2O3, Ta	Mo	Wets Mo; use Ta liner in EB guns.
Tin Oxide	SnO2	1127	6.95	--	--	--	~1000	ebeam (Xlnt)	Al2O3, Quartz	W	Films from W oxygen deficient, oxidize in air. n = 2.0
					sublimes						
Tin Selenide	SnSe	861	6.18	--	--	--	~400	ebeam (Good)	Quartz	--	JVST 12, 110 (1975)
Tin Sulphide	SnS	882	5.08	--	--	--	~450	--	Quartz	--	--
Tin Telluride	SnTe	780	6.44	--	--	--	~450	--	Quartz	--	--
Titanium	Ti	1675	4.5	0.628	1067	1235	1453	eBeam (Xlnt), Thermal	TiC	W	Alloys with refractory metals. Evolves gas on first heating.
Titanium Boride	TiB2	2980	4.5	--	--	--	--	ebeam (Poor)	--	--	--
Titanium Carbide	TiC	3140	4.93	--	--	--	~2300	--	--	--	JVST 12, 851, (1975)
Titanium Dioxide (rutile)	TiO2	1640	4.29	--	--	--	~1300	ebeam (Fair)	--	W, Mo	Evaporate in 10-4 of O2 onto 350° substrates. n = 2.4 App. Opt. 15, 2986 (1976)
Titanium Monoxide	TiO	1750	4.93	--	--	--	~1500	ebeam (Good)	VC	W, Mo	Use gentle preheat to outgas. Films TiO2 if evaporated like TiO2; n = 2.2

Appendix D

Technical Diagrams

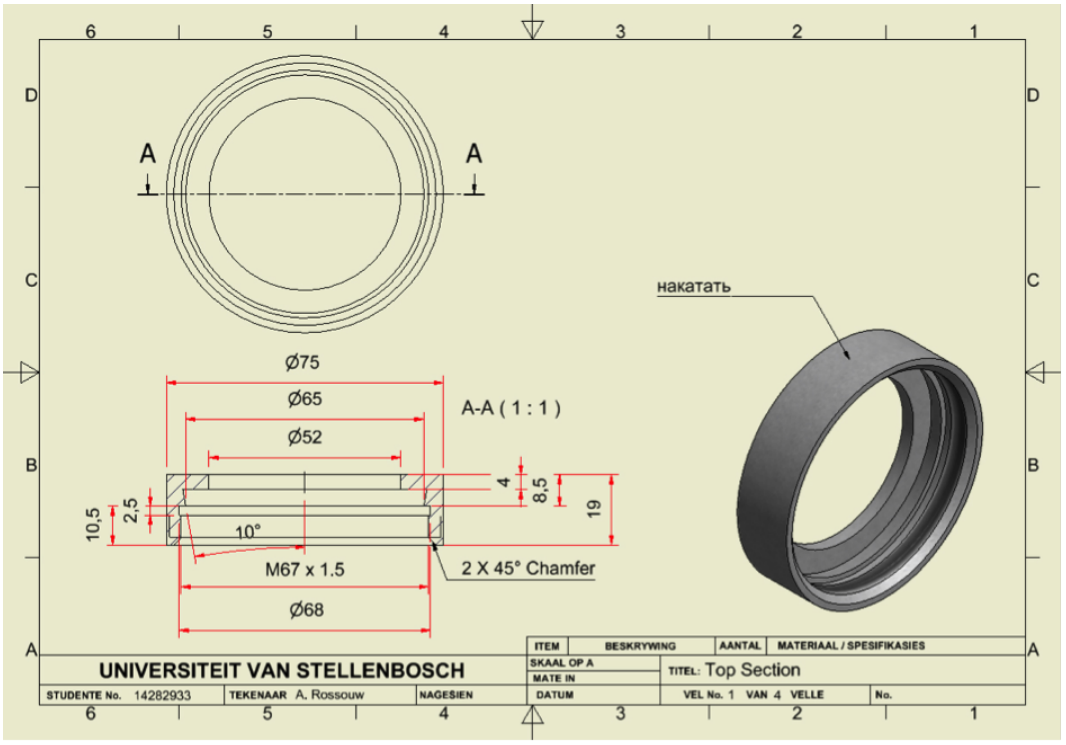

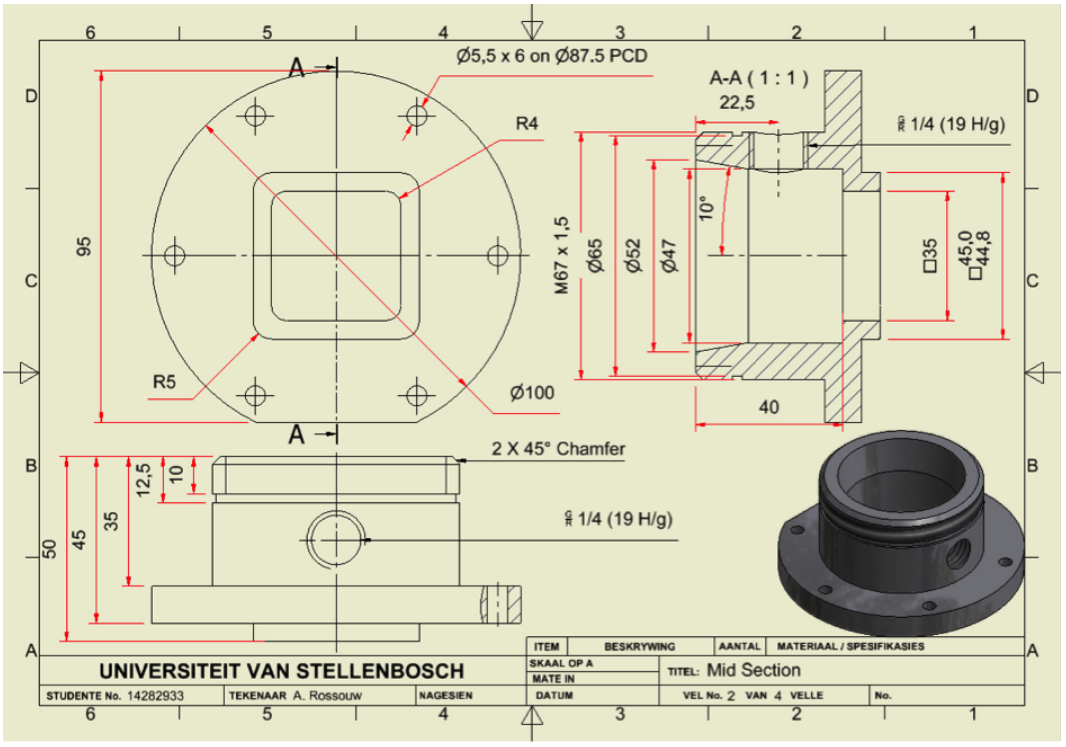

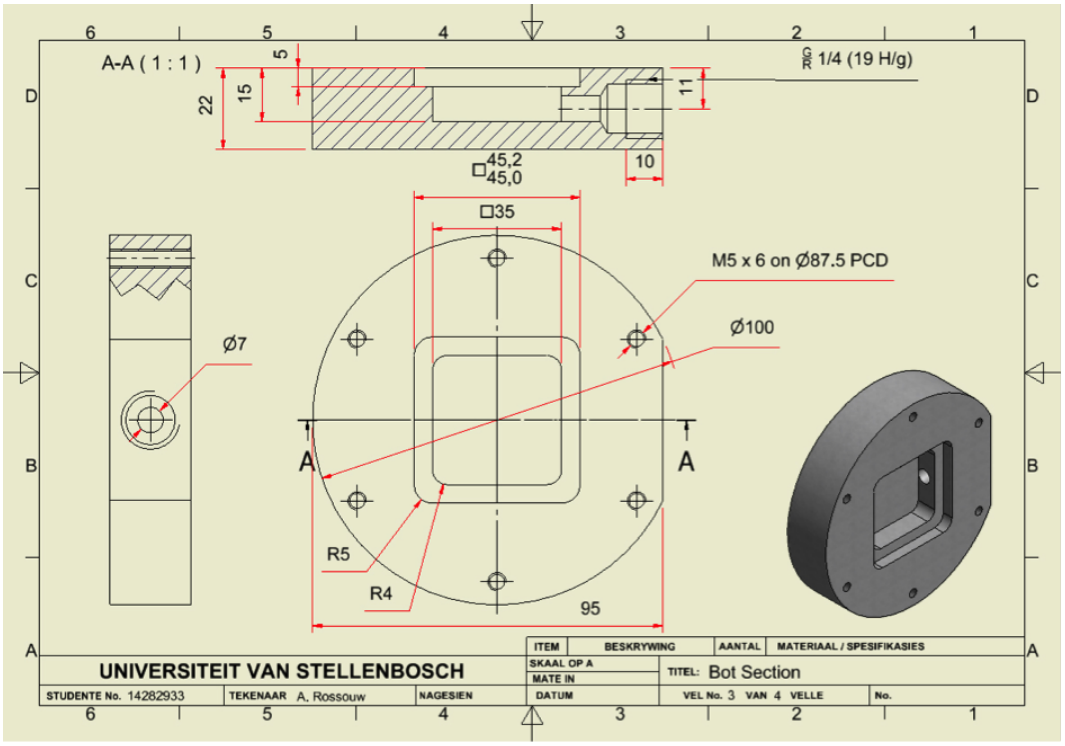

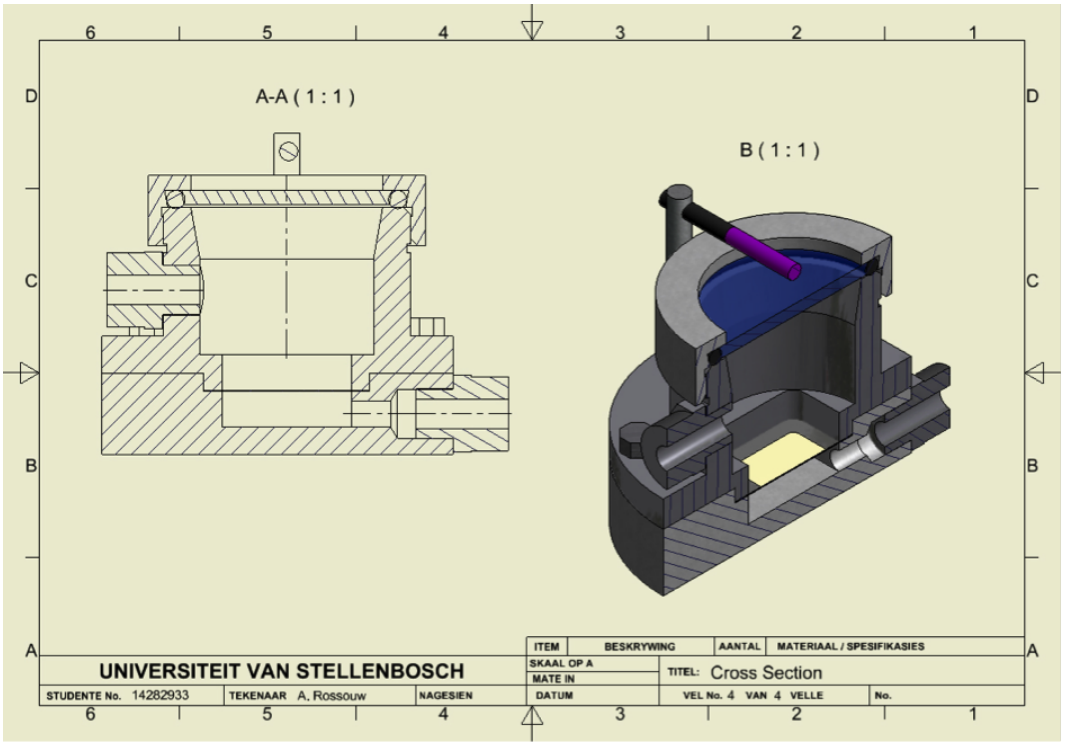

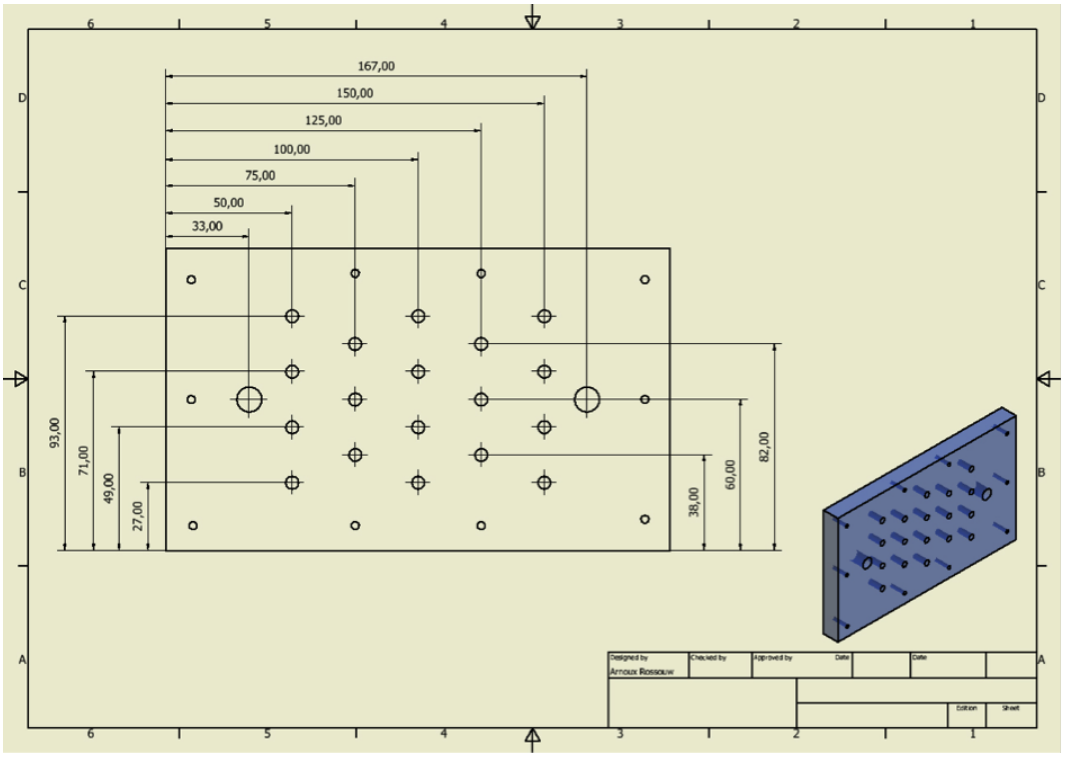

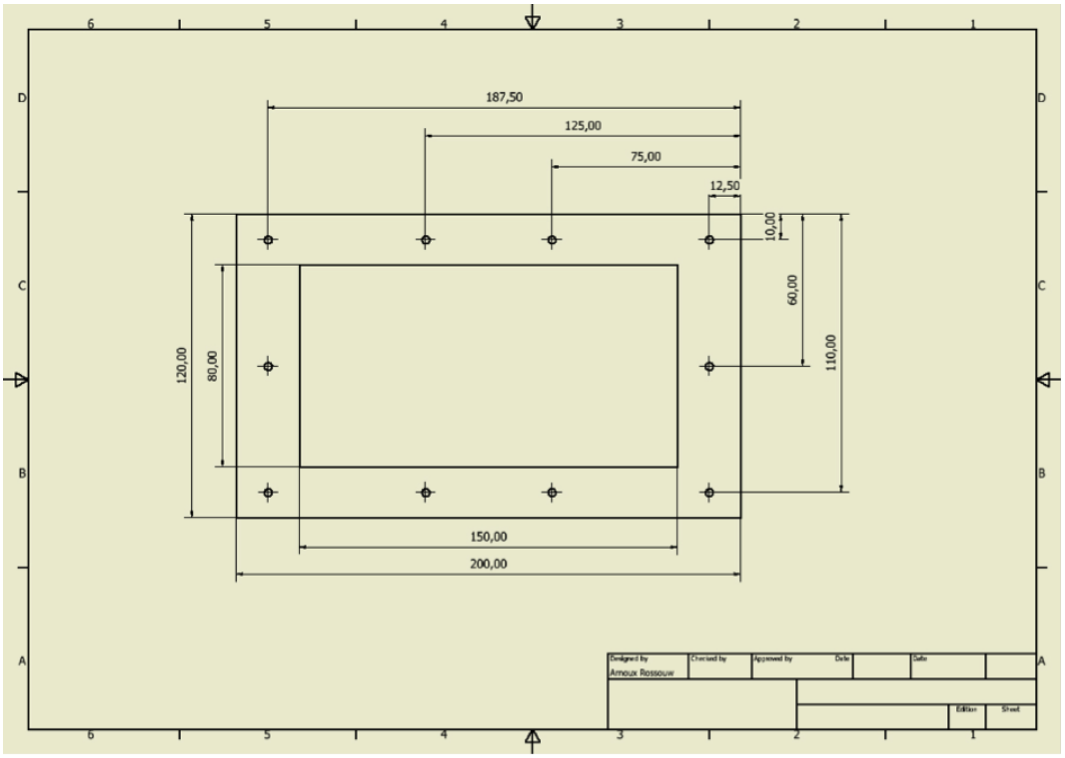

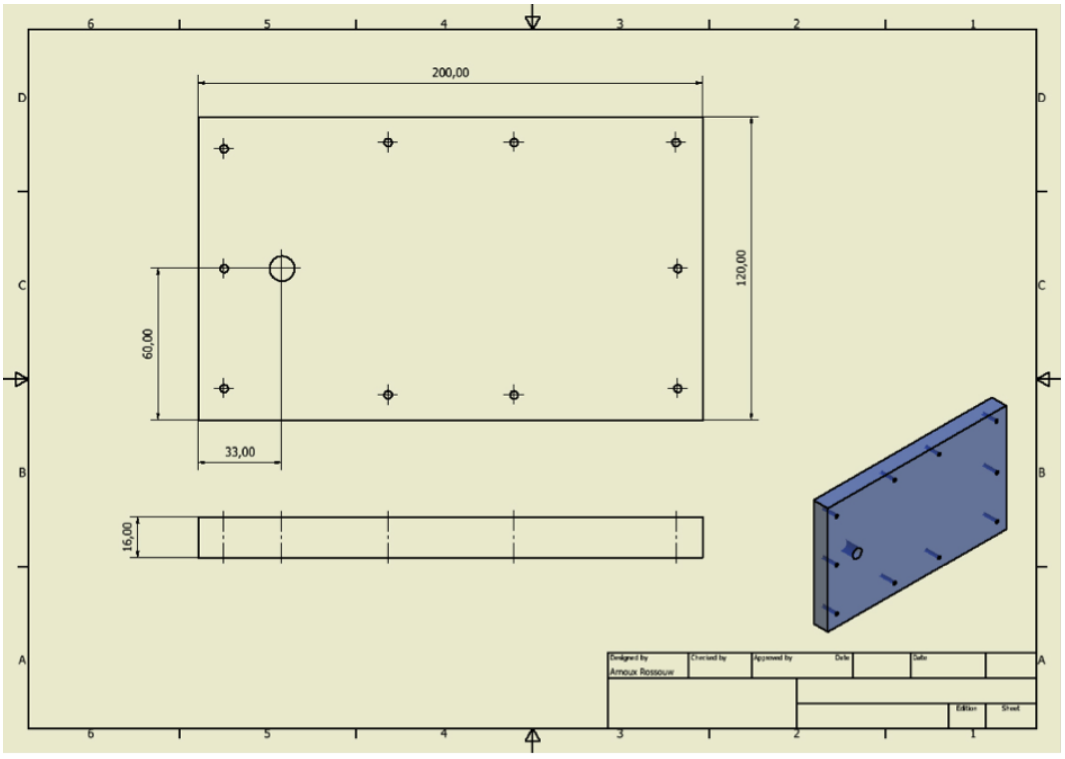

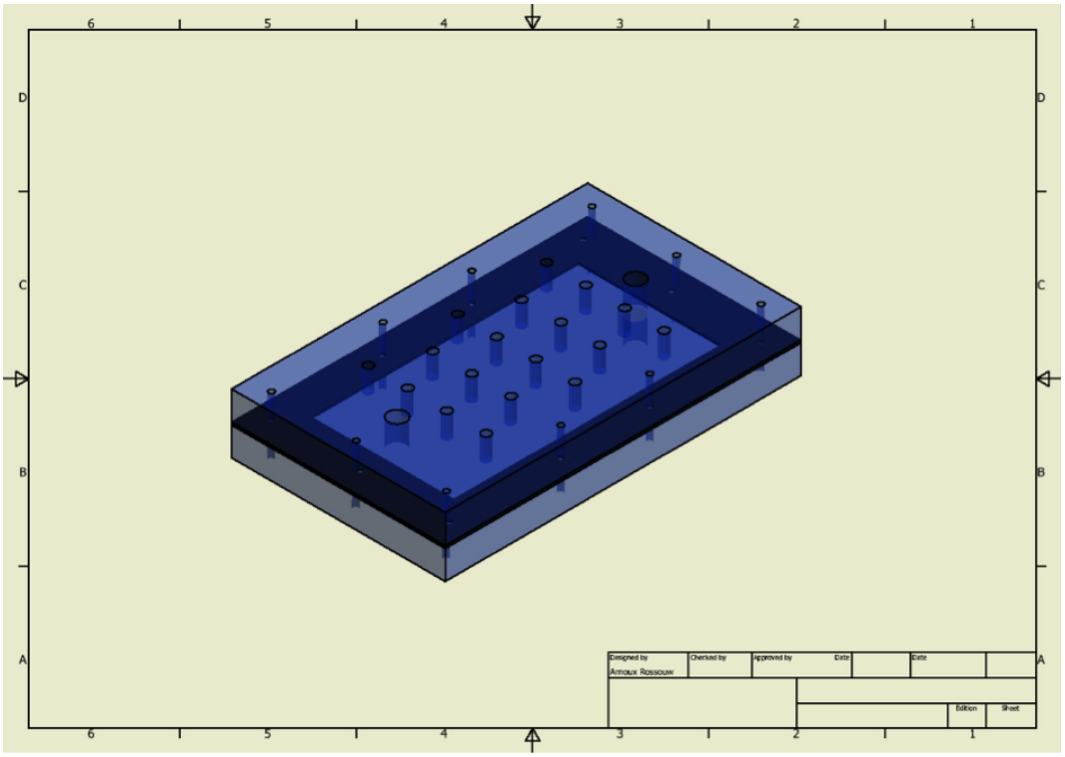

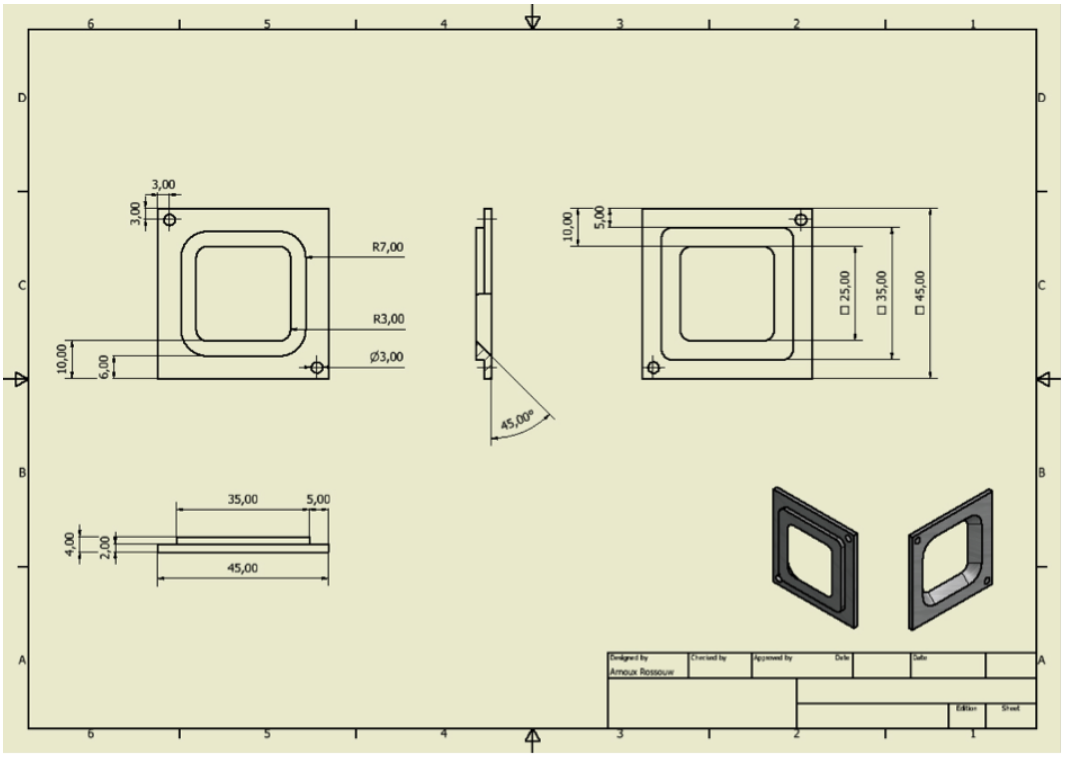

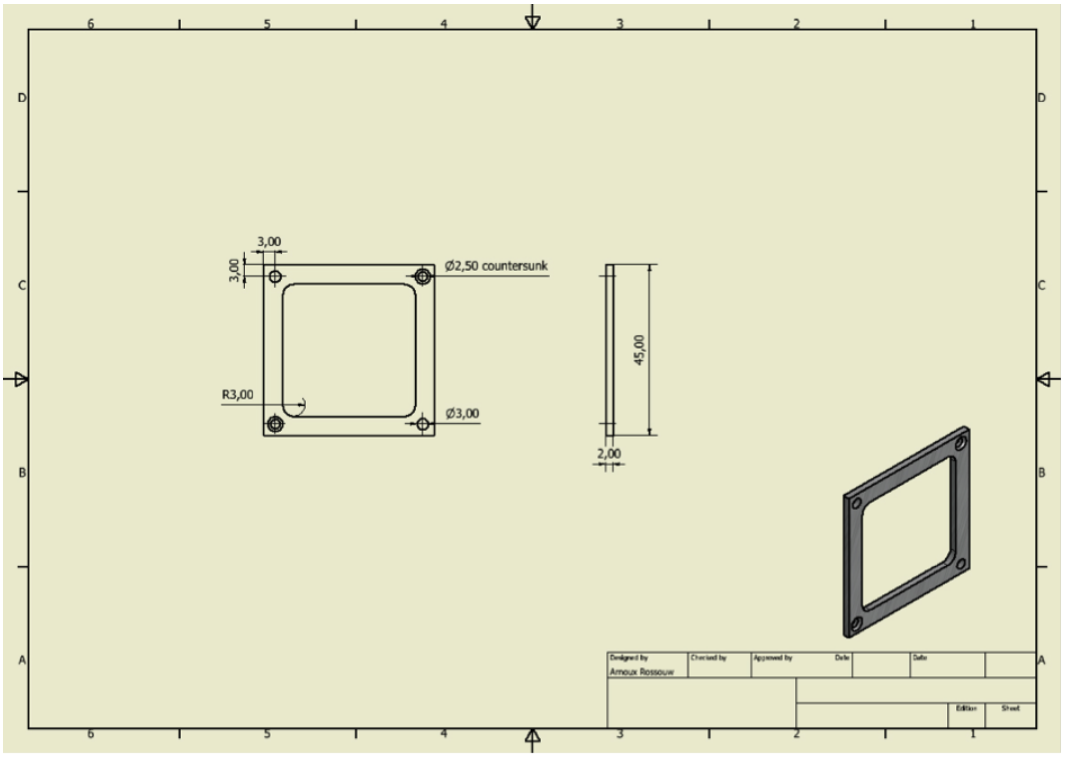

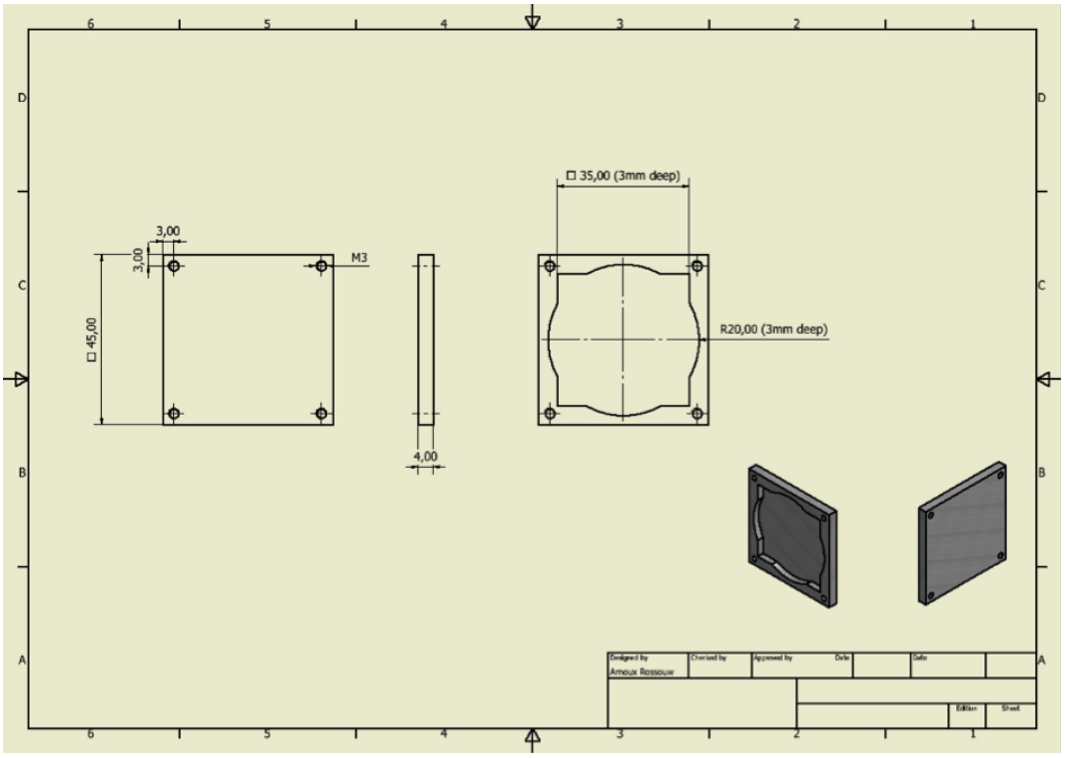

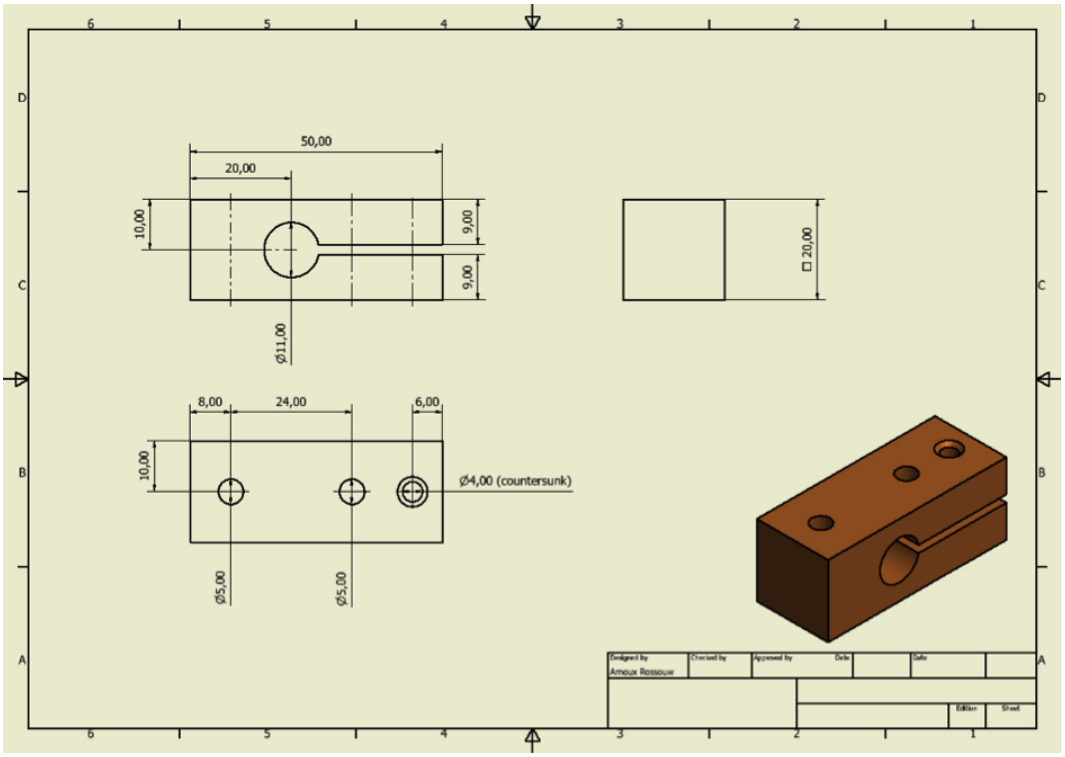

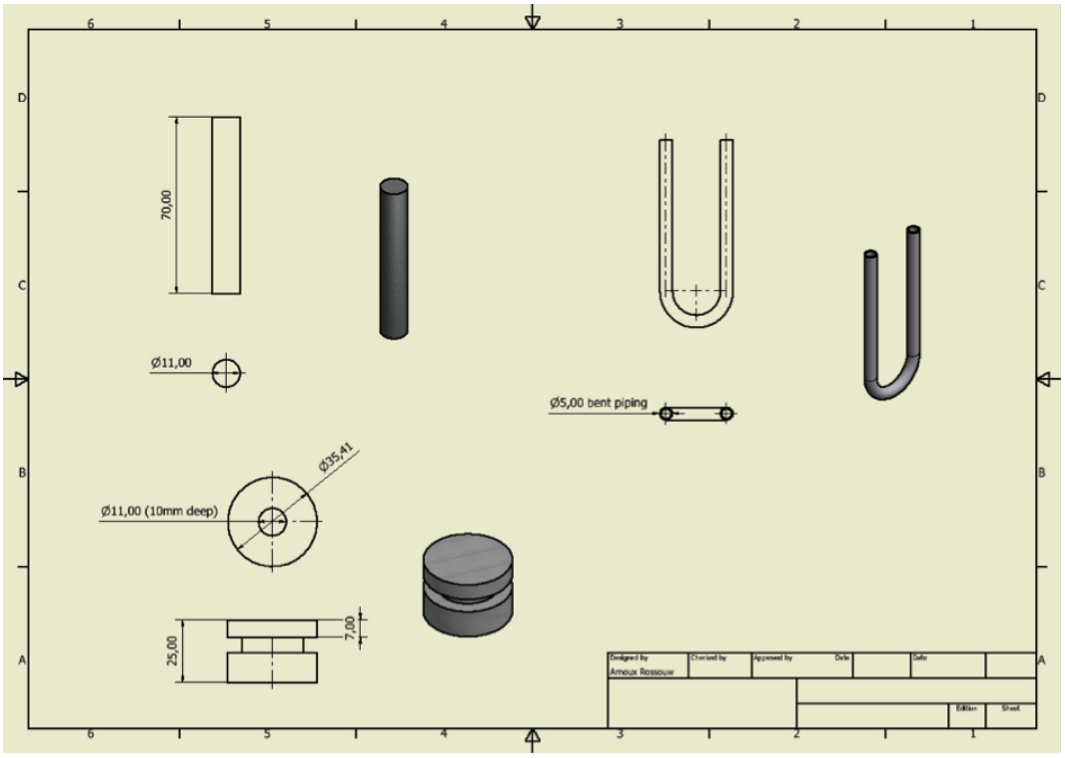

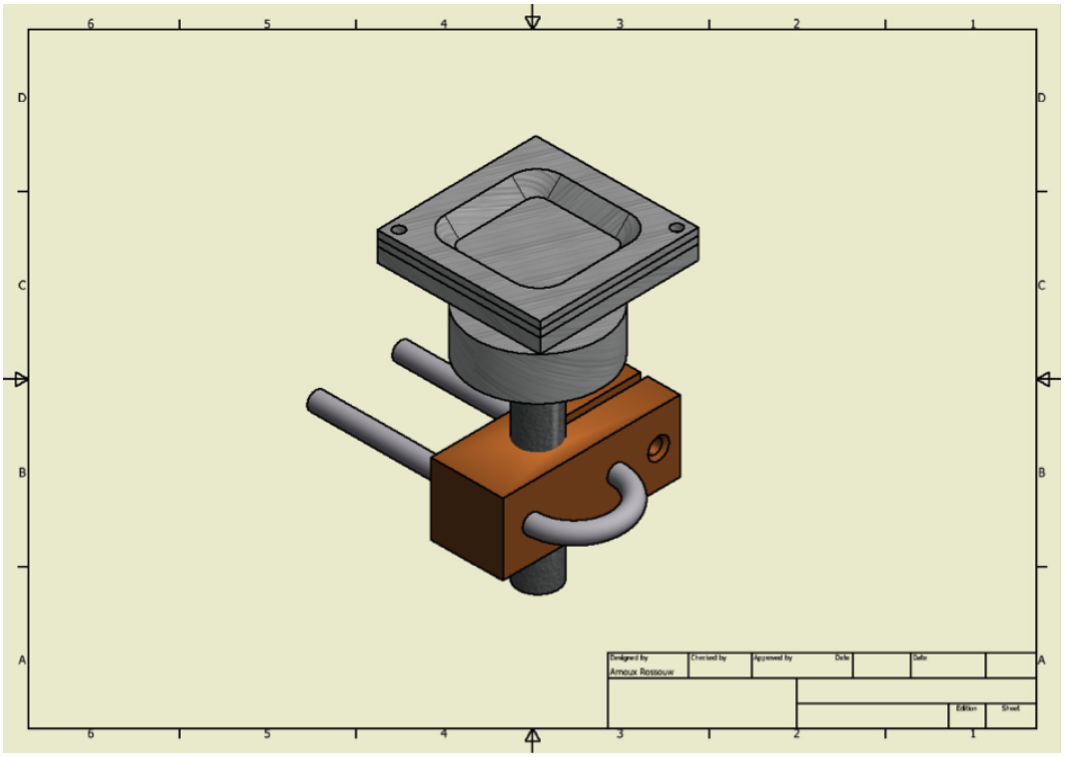

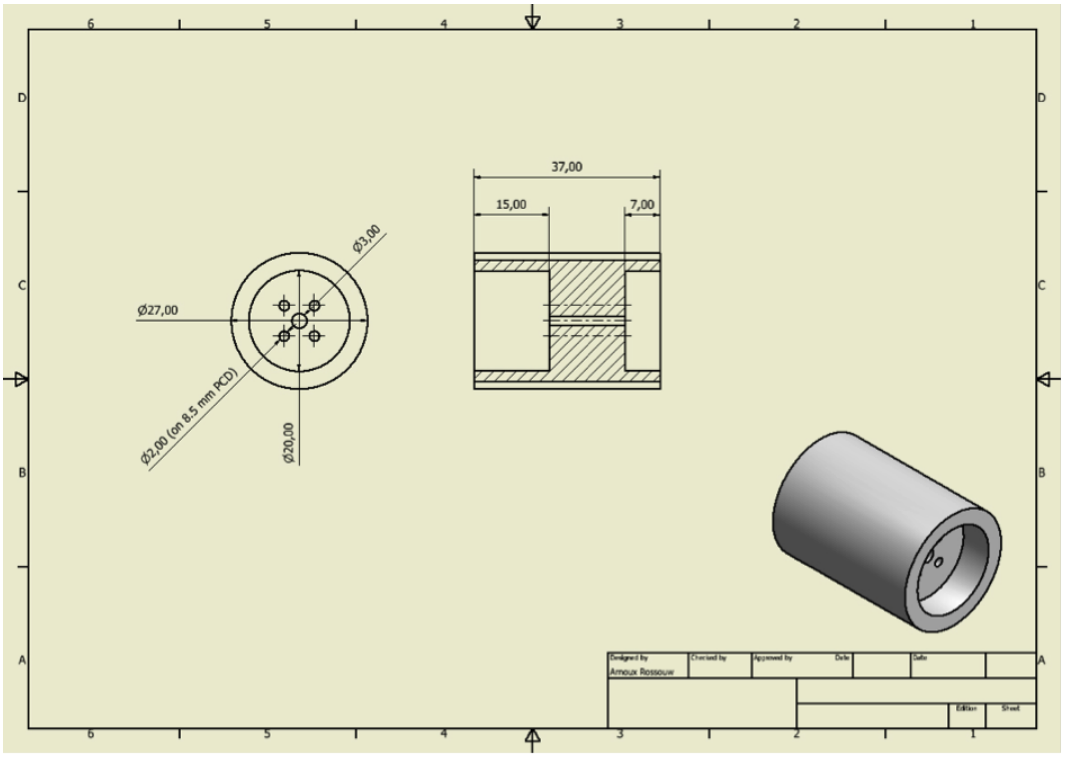

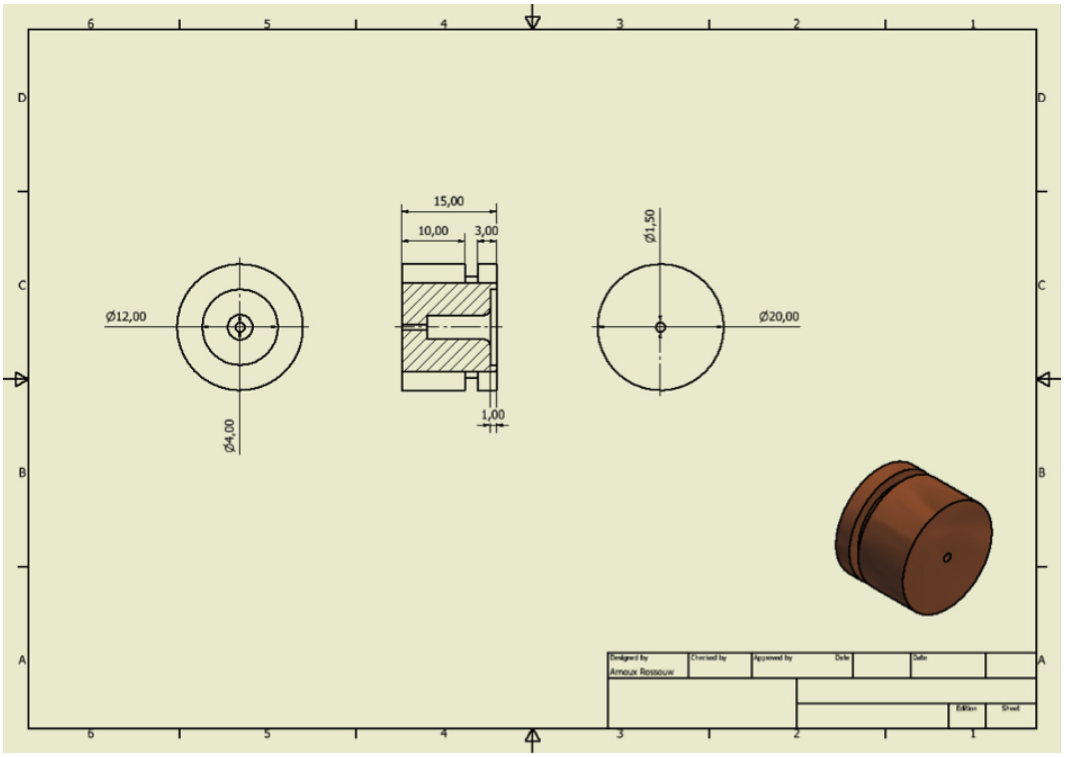

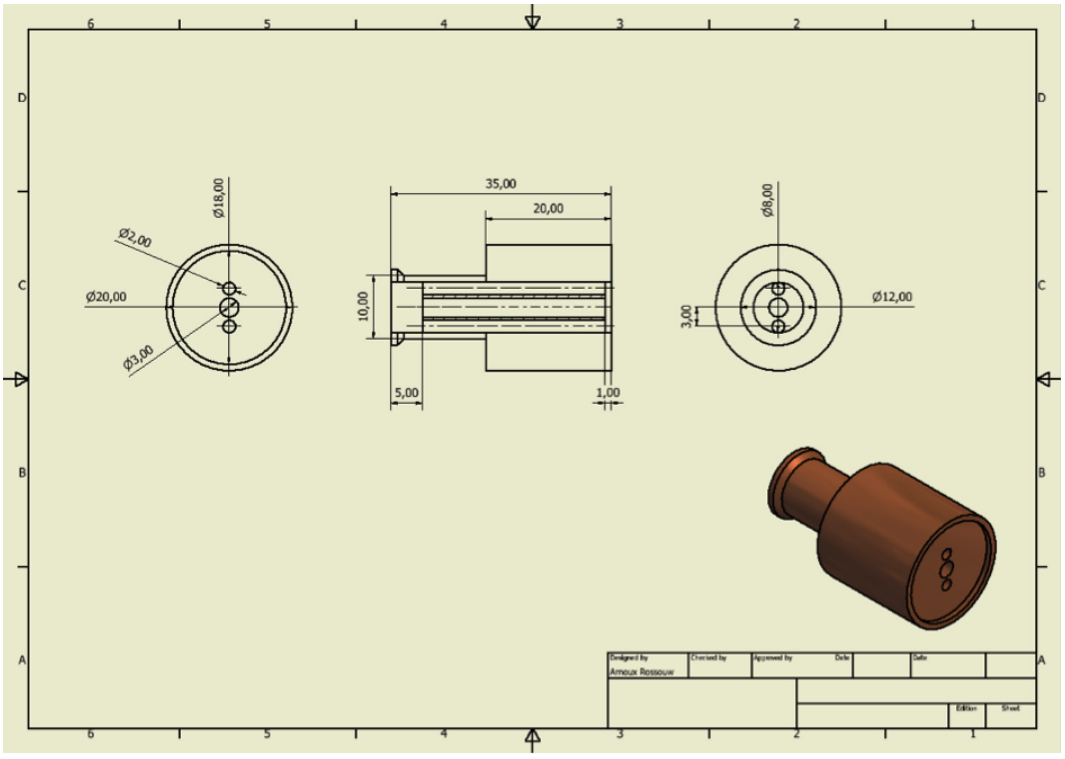

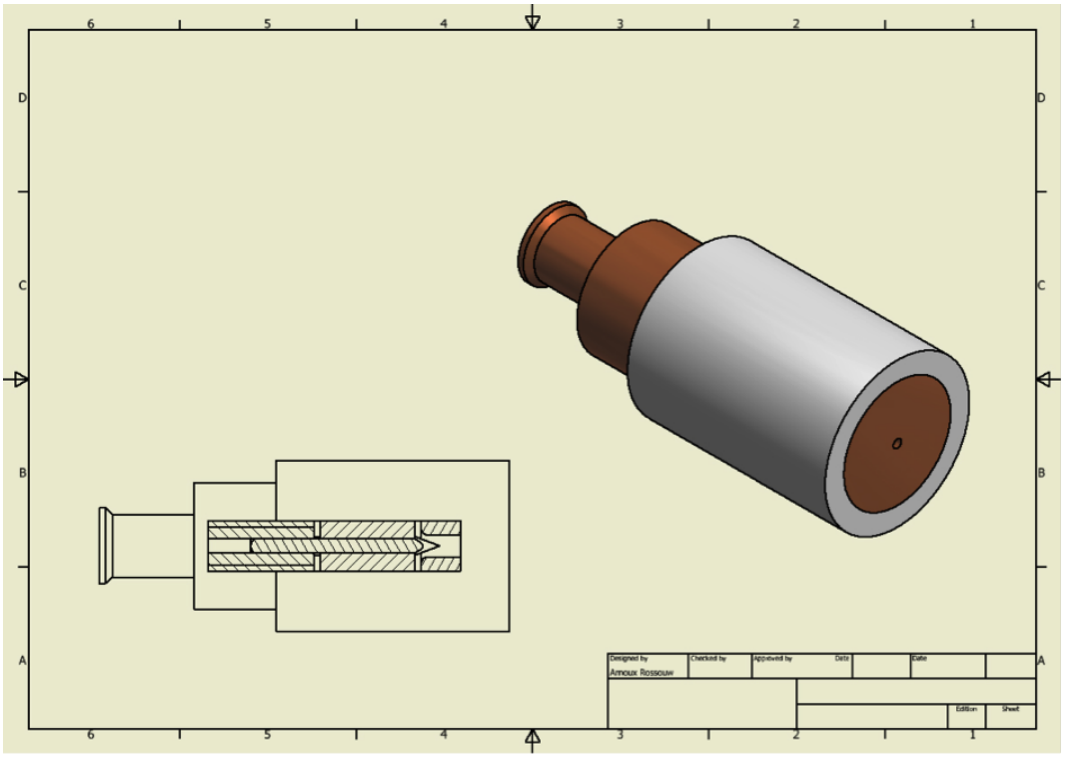

List of References

[1] X. Z. A. Fujishima and D. A. Tryk, *Surface Science Reports*, vol. 63, p. 515, 2008.

[2] C. H. O. Carp and A. Reller, *Progress in Solid State Chemistry*, vol. 32, pp. 33–177, 2004.

[3] R. Asahi, T. Morikawa, T. Ohwaki, K. Aoki and Y. Taga, *Science*, vol. 293, p. 269, 2001.

[4] W. C. H. T. M. Wang, S. K. Zheng and C. Wang, *Surface and Coatings Technology*, vol. 155, p. 141, 2002.

[5] S. Tanemura, L. Miao, W. Wunderlich, M. Tanemura, Y. Mori, S. Toh and K. Kaneko, *Science and Technology of Advanced Mater*, vol. 6, p. 11, 2005.

[6] C. R. M. D. R. Acosta, A. MartÌnez and J. M. Ortega, *Thin Solid Films*, vol. 490, p. 112, 2005.

[7] H. Zhou and D. Smith, *Environmental Engineering Science*, vol. 1, pp. 247–264, 2002.

[8] L. Dorfman and G. E. Adams, "Reactivity of the hydroxyl radical in aqueous solutions," National Bureau of Standards, Tech. Rep., 1973.

[9] W.H. Glaze, J.W. Kang and D.H. Chapin, *Ozone Science & Engineering*, vol. 9, pp. 335–352, 1987.

[10] M. Mulder, *Basic Principles of Membrane Technology*, second, Ed. Kluwer Academic Publishers, 1996.

[11] T. S. W.J. Koros, Y.H. Ma, *Pure and Applied Chemistry*, vol. 7, pp. 1479–1489, 1996.

[12] W. Kujawski and S. Krajewski, *Separation and Purification Technology*, vol. 57, pp. 495–501, 2007.

[13] M. T. S. Mozia and A.W.Morawski, *Applied Catalysis B*, vol. 59, 2005.

[14] M. T. M. Gryta and K. Karakulski, *Desalination*, vol. 198, pp. 67–73, 2006.

[15] S.P. Tretyakova , P.Yu. Apel , L.V. Jolos , T.I. Mamonova and V.V. Shirkova, *Nuclear Tracks*, vol. 2, pp. 283–287, 1980.

[16] H. Lueck, "Kinetics and mechanism of the formation and etching of particle tracks in poly(ethylene terephthalate)." Zentralinst. Kernforsch., Rossendorf Dresden, Tech. Rep., 1982.

[17] R. Fleischer, P. Price, and R. Walker, *Nuclear tracks in solids: principles and applications*. Univ of California Press, 1975.

[18] S. E. Fleischer RL, Price PB, *Science*, vol. 143, pp. 249–250, 1964.

[19] B. Fischer and R. Spohr, "Production and use of nuclear tracks: imprinting structure on solids," *Reviews of Modern Physics*, vol. 55, pp. 907–948, 1983.

[20] J. Calvo, A. Hernandez, G. Caruana, and L. Martinez, "Pore size distributions in microporous membranes i. surface study of track-etched filters by image analysis," *Journal of colloid and interface science*, vol. 175, pp. 138–150, 1995.

[21] R. Beck and J. Schultz, "Hindrance of solute diffusion within membranes as measured with microporous membranes of known pore geometry," *Biochimica et Biophysica Acta (BBA)-Biomembranes*, vol. 255, pp. 273–303, 1972.

[22] V. Kuznetsov, A. Didyk, and P. Apel, "Production and investigation of nuclear track membranes at jinr," *International Journal of Radiation Applications and Instrumentation. Part D. Nuclear Tracks and Radiation Measurements*, vol. 19, pp. 919–924, 1991.

[23] P. Apel, "Heavy particle tracks in polymers and polymeric track membranes," *Radiation measurements*, vol. 25, pp. 667–674, 1995.

[24] D. Pall, E. Kirnbauer, and B. Allen, "Particulate retention by bacteria retentive membrane filters," *Colloids and Surfaces*, vol. 1, pp. 235–256, 1980.

[25] A.A. Yasminov, G.Z. Blum, A.A Efremov, V.F Volodin, "Microfiltration of high-purity substances," *High Purity Substances (USSR)*, vol. 3, pp. 160–170, 1987.

[26] P. Bisio, J. Cartledge, W. Keesom, and C. Radke, "Molecular orientation of aqueous surfactants on a hydrophobic solid," *Journal of Colloid and Interface Science*, vol. 78, pp. 225–234, 1980.

[27] W. Keesom, R. Zelenka, and C. Radke, "A zeta-potential model for ionic surfactant adsorption on an ionogenic hydrophobic surface," *Journal of colloid and interface science*, vol. 125, pp. 575–585, 1988.

[28] E. Tracey and R. Davis, "Protein fouling of track-etched polycarbonate microfiltration membranes," *Journal of colloid and interface science*, vol. 167, pp. 104–116, 1994.

[29] P. Van den Oetelaar, I. Mentink, and G. Brinks, "Loss of peptides and proteins upon sterile filtration due to adsorption to membrane filters," *Drug Development and Industrial Pharmacy*, vol. 15, pp. 97–106, 1989.

[30] T. Brock, *Membrane filtration: a user's guide and reference manual*. Science Tech, 1983.

[31] B. Stevenson, J. Anderson, and S. Bullivant, "The epithelial tight junction: structure, function and preliminary biochemical characterization," *Molecular and cellular biochemistry*, vol. 83, pp. 129–145, 1988.

[32] T. Sergent-Engelen, C. Halleux, E. Ferain, H. Hanot, R. Legras, and Y. Schneider, "Improved cultivation of polarized animal cells on culture inserts with new transparent polyethylene terephthalate or polycarbonate microporous membranes," *Biotechnology techniques*, vol. 4, no. 2, pp. 89–94, 1990.

[33] M. Peterson and D. Gruenhaupt, "Protamine increases the permeability of cultured epithelial monolayers," *Journal of Applied Physiology*, vol. 68, no. 1, pp. 220–227, 1990.

[34] J. Rothman and L. Orci, "Movement of proteins through the golgi stack: a molecular dissection of vesicular transport." *The FASEB journal*, vol. 4, no. 5, pp. 1460–1468, 1990.

[35] V. Van Hinsbergh, M. Scheffer, and E. Langeler, "Macro-and microvascular endothelial cells from human tissues," *Cell Culture Techniques in Heart and Vessel Research*, pp. 179–204, 1990.

[36] *TranswellÆ Permeable Supports Selection and Use Guide*, Corning Incorporated, One Riverfront Plaza, Corning, NY 14831-0001 Std.

[37] G. Nash, "Filterability of blood cells: methods and clinical applications." *Biorheology*, vol. 27, no. 6, p. 873, 1990.

[38] R. DeBlois and C. Bean, "Counting and sizing of submicron particles by the resistive pulse technique," *Review of Scientific Instruments*, vol. 41, no. 7, pp. 909–916, 1970.

[39] D. Koutsouris, R. Guillet, J. Lelievre, M. Guillemin, P. Bertholom, Y. Beuzard, M. Boynard *et al.*, "Determination of erythrocyte transit times through micropores. i–basic operational principles." *Biorheology*, vol. 25, no. 5, p. 763, 1988.

[40] P. Meares and K. Page, "Rapid force-flux transitions in highly porous membranes," *Philosophical Transactions for the Royal Society of London. Series A, Mathematical and Physical Sciences*, pp. 1–46, 1972.

[41] W. Deen, "Hindered transport of large molecules in liquid-filled pores," *AIChE Journal*, vol. 33, no. 9, pp. 1409–1425, 1987.

[42] A. Mitrofanov, F. Pudonin, P. Apel, and T. Gromova, "The ultraviolet transmittance of porous vuv and x-ray diffraction filters," *Nuclear Instruments and Methods in Physics Research Section A: Accelerators, Spectrometers, Detectors and Associated Equipment*, vol. 308, no. 1, pp. 347–351, 1991.

[43] C. Pasternak, G. Alder, P. Apel, C. Bashford, D. Edmonds, Y. Korchev, A. Lev, G. Lowe, M. Milovanovich, C. Pitt *et al.*, "Nuclear track-etched filters as model pores for biological membranes," *Radiation measurements*, vol. 25, no. 1, pp. 675–683, 1995.

[44] T. Whitney, P. Searson, J. Jiang, C. Chien *et al.*, "Fabrication and magnetic properties of arrays of metallic nanowires." *Science (New York, NY)*, vol. 261, no. 5126, pp. 1316–1319, 1993.

[45] C. Martin, "Nanomaterials–a membrane-based synthetic approach," DTIC Document, Tech. Rep., 1994.

[46] L. Piraux, J. George, J. Despres, C. Leroy, E. Ferain, R. Legras, K. Ounadjela, and A. Fert, "Giant magnetoresistance in magnetic multilayered nanowires," *Applied physics letters*, vol. 65, no. 19, pp. 2484–2486, 1994.

[47] N. Zhitariuk, A. Le Moël, N. Mermilliod, and C. Trautmann, "Polymerization of pyrrole into track membranes," *Nuclear Instruments and Methods in Physics Research Section B: Beam Interactions with Materials and Atoms*, vol. 105, no. 1, pp. 204–207, 1995.

[48] M. Nishizawa, V. Menon, and C. Martin, "Metal nanotubule membranes with electrochemically switchable ion-transport selectivity." DTIC Document, Tech. Rep., 1995.

[49] V. Augugliaro, M. Litter, L. Palmisano, and J. Soria, "The combination of heterogeneous photocatalysis with chemical and physical operations: A tool for improving the photoprocess performance," *Journal of Photochemistry and Photobiology C: Photochemistry Reviews*, vol. 7, no. 4, pp. 127–144, 2006.

[50] M. Rivero, S. Parsons, P. Jeffrey, M. Pidou, and B. Jefferson, "Membrane chemical reactor(mcr) combining photocatalysis and microfiltration for grey water treatment," *Water Science & Technology*, vol. 53, no. 3, pp. 173–180, 2006.

[51] J. Fu, M. Ji, Y. Zhao, L. Wang, *Separation and Purification Technology*, vol. 50, pp. 107–113, 2006.

[52] J. Fu, M. Ji, Z. Wang, L. Jin, D. An, *Journal of Hazardous Materials*, vol. 131, pp. 238–242, 2006.

[53] S. Geissen, W. Xi, A. Weidemeyer, A. Vogelpohl, L. Bousselmi, A. Ghrabi, and A. Ennabli, "Comparison of suspended and fixed photocatalytic reactor systems," *Water Science & Technology*, vol. 44, no. 5, pp. 245–249, 2001.

[54] M. J. O'Neil, Ed., *The Merck Index: An Encyclopedia of Chemicals, Drugs, and Biologicals*. John Wiley & Sons, 2006.

[55] A. Popov, A. Priezzhev, J. Lademann, and R. Myllylä, "Tio2 nanoparticles as an effective uv-b radiation skin-protective compound in sunscreens," *Journal of Physics D: Applied Physics*, vol. 38, no. 15, p. 2564, 2005.

[56] L. Phillips and D. Barbano, "The influence of fat substitutes based on protein and titanium dioxide on the sensory properties of lowfat milks," *Journal of dairy science*, vol. 80, no. 11, pp. 2726–2731, 1997.

[57] U. Diebold, "The surface science of titanium dioxide," *Surface science reports*, vol. 48, no. 5, pp. 53–229, 2003.

[58] *Card 21-1272 (anatase)*, International Centre for Diffraction Data Std.

[59] *Card 21-1276 (rutile)*, International Centre for Diffraction Data Std.

[60] *Card 29-1360 (brookite)*, International Centre for Diffraction Data Std.

[61] D. L. B. J. R. Smyth, *Crystal Structures and Cation Sites of the Rock-Forming Minerals*. Allen and Unwin, 1988.

[62] O. Carp, C. Huisman, and A. Reller, "Photoinduced reactivity of titanium dioxide," *Progress in Solid State Chemistry*, vol. 32, no. 1, pp. 33–177, 2004.

[63] L. Kavan, M. Grätzel, S. Gilbert, C. Klemenz, and H. Scheel, "Electrochemical and photoelectrochemical investigation of single-crystal anatase," *Journal of the American Chemical Society*, vol. 118, no. 28, pp. 6716–6723, 1996.

[64] C. Kılıc and A. Zunger, "n-type doping of oxides by hydrogen," *Applied physics letters*, vol. 81, no. 1, pp. 73–75, 2002.

[65] W. Chen, Y. Wang, and H. Chan, "Hydrogen: A metastable donor in TiO_2 single crystals," *Applied physics letters*, vol. 92, no. 11, pp. 112 907–112 907, 2008.

[66] P. Peacock and J. Robertson, "Behavior of hydrogen in high dielectric constant oxide gate insulators," *Applied physics letters*, vol. 83, no. 10, pp. 2025–2027, 2003.

[67] C. K. H.M. Lin and C. Tung, *Nanostructured Materials*, vol. 9, p. 747, 1997.

[68] G. Sberveglieri, E. Comini, G. Faglia, M. Atashbar, and W. Wlodarski, "Titanium dioxide thin films prepared for alcohol microsensor applications," *Sensors and Actuators B: Chemical*, vol. 66, no. 1, pp. 139–141, 2000.

[69] L. Francioso, D. Presicce, M. Epifani, P. Siciliano, and A. Ficarella, "Response evaluation of tio_2 sensor to flue gas on spark ignition engine and in controlled environment," *Sensors and Actuators B: Chemical*, vol. 107, no. 2, pp. 563–571, 2005.

[70] B. Karunagaran, P. Uthirakumar, S. Chung, S. Velumani, and E. Suh, "Tio_2 thin film gas sensor for monitoring ammonia," *Materials characterization*, vol. 58, no. 8, pp. 680–684, 2007.

[71] Jin Young Kim, Hyun Suk Jung, Jung Hong No, Jeong-Ryeol Kim, Kug Sun Hong, "Influence of anatase-rutile phase transformation on dielectric properties of sol-gel derived TiO_2 thin films," *Journal of Electroceramics*, vol. 16, pp. 447–451, 2006.

[72] B. Park, L. Li, B. Gibbons, J. Huang, and Q. Jia, "Photovoltaic response and dielectric properties of epitaxial anatase-tio_2 films grown on conductive $la_0.5sr_0.5coo_3$ electrodes," *Applied Physics Letters*, vol. 79, no. 17, pp. 2797–2799, 2001.

[73] S. Campbell, H. Kim, D. Gilmer, B. He, T. Ma, and W. Gladfelter, "Titanium dioxide (tio$_2$)-based gate insulators," *IBM journal of research and development*, vol. 43, no. 3, pp. 383–392, 1999.

[74] S. Kim, W. Kim, K. Kim, C. Hwang, and J. Jeong, "High dielectric constant TiO_2 thin films on a Ru electrode grown at 250°C by atomic-layer deposition," *Applied physics letters*, vol. 85, no. 18, pp. 4112–4114, 2004.

[75] S. Dueñas, H. Castán, H. García, L. Bailón, K. Kukli, J. Lu, M. Ritala, and M. Leskelä, "Selection of post-growth treatment parameters for atomic layer deposition of structurally disordered TiO_2 thin films," *Journal of Non-Crystalline Solids*, vol. 354, no. 2, pp. 404–408, 2008.

[76] J. Niinistö, K. Kukli, M. Heikkilä, M. Ritala, and M. Leskelä, "Atomic layer deposition of high-k oxides of the group 4 metals for memory applications," *Advanced engineering materials*, vol. 11, no. 4, pp. 223–234, 2009.

[77] M. Lee, J. Huang, and T. Wu, "Low Leakage Current Fluorinated LPD-SiO_2/MOCVD TiO_2 Films," *Electrochemical and solid-state letters*, vol. 8, no. 1, pp. F8–F11, 2005.

[78] M. Lee and C. Yen, "Electrical Improvement of Fluorine-Passivated Metal-Organic Chemical Vapor Deposited TiO_2 Film on (NH_4) $2S_x$-treated GaAs," *Japanese Journal of Applied Physics*, vol. 46, pp. L1173–L1175, 2007.

[79] S. Kim, G. Choi, S. Lee, M. Seo, S. Lee, J. Han, H. Ahn, S. Han, and C. Hwang, "Al-Doped TiO_2 Films with Ultralow Leakage Currents for Next Generation DRAM Capacitors," *Advanced Materials*, vol. 20, no. 8, pp. 1429–1435, 2008.

[80] W. Jeon, H. Chung, D. Joo, and S. Kang, "TiO_2/ Al_2O_3/ TiO_2 Nanolaminated Thin Films for DRAM Capacitor Deposited by Plasma-Enhanced Atomic Layer Deposition," *Electrochemical and Solid-State Letters*, vol. 11, no. 2, pp. H19–H21, 2008.

[81] K. Kukli, M. Ritala, M. Leskelä, J. Sundqvist, L. Oberbeck, J. Heitmann, U. Schröder, J. Aarik, and A. Aidla, "Influence of TiO_2 incorporation in HfO_2 and Al_2O_3 based capacitor dielectrics," *Thin solid films*, vol. 515, no. 16, pp. 6447–6451, 2007.

[82] Y. Kim and S. Jin Yun, "Nanolaminated al$_2$ol$_3$–tiol$_2$ thin films grown by atomic layer deposition," *Journal of crystal growth*, vol. 274, no. 3, pp. 585–593, 2005.

[83] J. Yang, M. Pickett, X. Li, D. Ohlberg, D. Stewart, and R. Williams, "Memristive switching mechanism for metal/oxide/metal nanodevices," *Nature nanotechnology*, vol. 3, no. 7, pp. 429–433, 2008.

[84] J. Bennett, E. Pelletier, G. Albrand, J. Borgogno, B. Lazarides, C. Carniglia, R. Schmell, T. Allen, T. Tuttle-Hart, K. Guenther *et al.*, "Comparison of the properties of titanium dioxide films prepared by various techniques," *Applied optics*, vol. 28, no. 16, pp. 3303–3317, 1989.

[85] A. Fujishima, X. Zhang, and D. Tryk, "$TiOl_2$ photocatalysis and related surface phenomena," *Surface Science Reports*, vol. 63, no. 12, pp. 515–582, 2008.

[86] A. Linsebigler, G. Lu, and J. Yates Jr, "Photocatalysis on tio2 surfaces: principles, mechanisms, and selected results," *Chemical Reviews*, vol. 95, no. 3, pp. 735–758, 1995.

[87] M. Fox and M. Dulay, "Heterogeneous photocatalysis," *Chemical reviews*, vol. 93, no. 1, pp. 341–357, 1993.

[88] M. Hoffmann, S. Martin, W. Choi, and D. Bahnemann, "Environmental applications of semiconductor photocatalysis," *Chemical reviews*, vol. 95, no. 1, pp. 69–96, 1995.

[89] A. Wold, "Photocatalytic properties of titanium dioxide (tio2)," *Chemistry of materials*, vol. 5, no. 3, pp. 280–283, 1993.

[90] T. L. Thompson and J. John T. Yates, "Surface science studies of the photoactivation of tio2 - new photochemical processes," *Chemical Reviews*, vol. 106, pp. 4428–4453, 2006.

[91] A. Fujishima and X. Zhang, "Titanium dioxide photocatalysis: present situation and future approaches," *Comptes Rendus Chimie*, vol. 9, no. 5, pp. 750–760, 2006.

[92] A. Mills and S. Le Hunte, "An overview of semiconductor photocatalysis," *Journal of photochemistry and photobiology. A, Chemistry*, vol. 108, no. 1, pp. 1–35, 1997.

[93] O. Carp, C. Huisman, and A. Reller, "Photoinduced reactivity of titanium dioxide," *Progress in Solid State Chemistry*, vol. 32, no. 1, pp. 33–177, 2004.

[94] U. Gaya and A. Abdullah, "Heterogeneous photocatalytic degradation of organic contaminants over titanium dioxide: A review of fundamentals, progress and problems," *Journal of Photochemistry and Photobiology C: Photochemistry Reviews*, vol. 9, no. 1, pp. 1–12, 2008.

[95] K. Hashimoto, H. Irie, and A. Fujishima, "$TiOl_2$ photocatalysis: A historical overview and future prospects," *JAPANESE JOURNAL OF APPLIED PHYSICS PART 1 REGULAR PAPERS SHORT NOTES AND REVIEW PAPERS*, vol. 44, no. 12, p. 8269, 2005.

[96] T. Tachikawa, M. Fujitsuka, and T. Majima, "Mechanistic insight into the tio2 photocatalytic reactions: design of new photocatalysts," *The Journal of Physical Chemistry C*, vol. 111, no. 14, pp. 5259–5275, 2007.

[97] K. Kabra, R. Chaudhary, and R. Sawhney, "Treatment of hazardous organic and inorganic compounds through aqueous-phase photocatalysis: A review," *Industrial & engineering chemistry research*, vol. 43, no. 24, pp. 7683–7696, 2004.

[98] T. W. Akira Fujishima, Kazuhito Hashimoto, *TiO2 Photocatalysis: Fundamentals and Applications*. Bkc, Incorporated, 1999.

[99] K. Rajeshwar, M. Osugi, W. Chanmanee, C. Chenthamarakshan, M. Zanoni, P. Kajitvichyanukul, and R. Krishnan-Ayer, "Heterogeneous photocatalytic treatment of organic dyes in air and aqueous media," *Journal of Photochemistry and Photobiology C: Photochemistry Reviews*, vol. 9, no. 4, pp. 171–192, 2008.

[100] V. Augugliaro, M. Litter, L. Palmisano, and J. Soria, "The combination of heterogeneous photocatalysis with chemical and physical operations: A tool for improving the photoprocess performance," *Journal of Photochemistry and Photobiology C: Photochemistry Reviews*, vol. 7, no. 4, pp. 127–144, 2006.

[101] D. Chatterjee and S. Dasgupta, "Visible light induced photocatalytic degradation of organic pollutants," *Journal of Photochemistry and Photobiology C: Photochemistry Reviews*, vol. 6, no. 2, pp. 186–205, 2005.

[102] D. Blake, *Bibliography of work on the heterogeneous photocatalytic removal of hazardous compounds from water and air*. National Renewable Energy Laboratory, 2001.

[103] A. Kudo and Y. Miseki, "Heterogeneous photocatalyst materials for water splitting," *Chemical Society Reviews*, vol. 38, no. 1, pp. 253–278, 2009.

[104] M. Anpo, H. Yamashita, Y. Ichihashi, and S. Ehara, "Photocatalytic reduction of co$_2$ with h$_2$ o on various titanium oxide catalysts," *Journal of Electroanalytical Chemistry*, vol. 396, no. 1, pp. 21–26, 1995.

[105] I. K. Konstantinou and T. A. Albanis, "Tio2-assisted photocatalytic degradation of azo dyes in aqueous solution: kinetic and mechanistic investigations: A review," *Applied Catalysis B: Environmental*, vol. 49, no. 1, pp. 1 – 14, 2004. [Online]. Available: http://www.sciencedirect.com/science/article/pii/S0926337303005411

[106] L. Reutergådh and M. Iangphasuk, "Photocatalytic decolourization of reactive azo dye: A comparison between tio$_2$ and us photocatalysis," *Chemosphere*, vol. 35, no. 3, pp. 585–596, 1997.

[107] D. Mardare, M. Tasca, M. Delibas, and G. Rusu, "On the structural properties and optical transmittance of tio< sub> 2</sub> rf sputtered thin films," *Applied Surface Science*, vol. 156, no. 1, pp. 200–206, 2000.

[108] H. Fujii, M. Ohtaki, K. Eguchi, and H. Arai, "Preparation and photocatalytic activities of a semiconductor composite of cds embedded in a tio2 gel as a stable oxide semiconducting matrix," *Journal of Molecular Catalysis A: Chemical*, vol. 129, no. 1, pp. 61–68, 1998.

[109] L. Wu, J. Yu, and X. Fu, "Characterization and photocatalytic mechanism of nanosized cds coupled tio$_2$ nanocrystals under visible light irradiation," *Journal of Molecular Catalysis A: Chemical*, vol. 244, no. 1, pp. 25–32, 2006.

[110] W. Siripala, A. Ivanovskaya, T. F. Jaramillo, S.-H. Baeck, and E. W. McFarland, "A cu2o/tio2 heterojunction thin film cathode for photoelectrocatalysis," *Solar Energy Materials and Solar*

Cells, vol. 77, no. 3, pp. 229 – 237, 2003. [Online]. Available: http://www.sciencedirect.com/science/article/pii/S0927024802003434

[111] K. Guan, B. Lu, and Y. Yin, "Enhanced effect and mechanism of sio_2 addition in super-hydrophilic property of tio_2 films," *Surface and Coatings Technology*, vol. 173, no. 2, pp. 219–223, 2003.

[112] N. Kanai, T. Nuida, K. Ueta, K. Hashimoto, T. Watanabe, and H. Ohsaki, "Photocatalytic efficiency of tio_2/sno_2 thin film stacks prepared by dc magnetron sputtering," *Vacuum*, vol. 74, no. 3, pp. 723–727, 2004.

[113] X. Wang, Z. Hu, Y. Chen, G. Zhao, Y. Liu, and Z. Wen, "A novel approach towards high-performance composite photocatalyst of tio_2 deposited on activated carbon," *Applied Surface Science*, vol. 255, no. 7, pp. 3953–3958, 2009.

[114] B. Gao, Y. Ma, Y. Cao, W. Yang, and J. Yao, "Great enhancement of photocatalytic activity of nitrogen-doped titania by coupling with tungsten oxide," *The Journal of Physical Chemistry B*, vol. 110, no. 29, pp. 14 391–14 397, 2006.

[115] R. Wang, K. Hashimoto, A. Fujishima, M. Chikuni, E. Kojima, A. Kitamura, M. Shimohigoshi, and T. Watanabe, "Light-induced amphiphilic surfaces," *Nature*, vol. 388, no. 6641, pp. 431–432, 1997.

[116] ——, "Photogeneration of highly amphiphilic tio2 surfaces," *Advanced Materials*, vol. 10, no. 2, pp. 135–138, 1999.

[117] N. Sakai, A. Fujishima, T. Watanabe, and K. Hashimoto, "Quantitative evaluation of the photoinduced hydrophilic conversion properties of tio2 thin film surfaces by the reciprocal of contact angle," *The Journal of Physical Chemistry B*, vol. 107, no. 4, pp. 1028–1035, 2003.

[118] M. Nakamura, K. Makino, L. Sirghi, T. Aoki, and Y. Hatanaka, "Hydrophilic properties of hydro-oxygenated tio_x films prepared by plasma enhanced chemical vapor deposition," *Surface and Coatings Technology*, vol. 169, pp. 699–702, 2003.

[119] T. Zubkov, D. Stahl, T. Thompson, D. Panayotov, O. Diwald, and J. Yates Jr, "Ultraviolet light-induced hydrophilicity effect on tio_2 $(110)(1\times 1)$. dominant role of the photooxidation of adsorbed hydrocarbons causing wetting by water droplets," *The Journal of Physical Chemistry B*, vol. 109, no. 32, pp. 15 454–15 462, 2005.

[120] A. Mills and M. Crow, "In situ, continuous monitoring of the photoinduced superhydrophilic effect: Influence of uv-type and ambient atmospheric and droplet composition," *The Journal of Physical Chemistry C*, vol. 111, no. 16, pp. 6009–6016, 2007.

[121] *TiO2 Photocatalysis: Fundamentals and Applications*, 1999.

[122] K. Sunada, Y. Kikuchi, K. Hashimoto, and A. Fujishima, "Bactericidal and detoxification effects of tio2 thin film photocatalysts," *Environmental science & technology*, vol. 32, no. 5, pp. 726–728, 1998.

[123] E. Wolfrum, J. Huang, D. Blake, P. Maness, Z. Huang, J. Fiest, and W. Jacoby, "Photocatalytic oxidation of bacteria, bacterial and fungal spores, and model biofilm components to carbon dioxide on titanium dioxide-coated surfaces," *Environmental science & technology*, vol. 36, no. 15, pp. 3412–3419, 2002.

[124] M. Wong, W. Chu, D. Sun, H. Huang, J. Chen, P. Tsai, N. Lin, M. Yu, S. Hsu, S. Wang *et al.*, "Visible-light-induced bactericidal activity of a nitrogen-doped titanium photocatalyst against human pathogens," *Applied and environmental microbiology*, vol. 72, no. 9, pp. 6111–6116, 2006.

[125] E. Duffy, F. A. Touati, S. Kehoe, O. McLoughlin, L. Gill, W. Gernjak, I. Oller, M. Maldonado, S. Malato, J. Cassidy, R. Reed, and K. McGuigan, "A novel tio2-assisted solar photocatalytic batch-process disinfection reactor for the treatment of biological and chemical contaminants in domestic drinking water in developing countries," *Solar Energy*, vol. 77, no. 5, pp. 649 – 655, 2004, <ce:title>Photocatalysis</ce:title>. [Online]. Available: http://www.sciencedirect.com/science/article/pii/S0038092X04001112

[126] M. Raulio, V. Pore, S. Areva, M. Ritala, M. Leskelä, M. Lindén, J. Rosenholm, K. Lounatmaa, and M. Salkinoja-Salonen, "Destruction of deinococcus geothermalis biofilm by photocatalytic ald and sol-gel tio 2 surfaces," *Journal of industrial microbiology & biotechnology*, vol. 33, no. 4, pp. 261–268, 2006.

[127] A. Mills, A. Lepre, N. Elliott, S Bhopal, I.P. Parkin, and S.A. O'Neill, "Characterisation of the photocatalyst Pilkington Activ™: a reference film photocatalyst?" *Journal of Photochemistry and Photobiology A: Chemistry*, vol. 160, no. 3, pp. 213–224, 2003.

[128] R. Kubin and A. Fletcher, "Fluorescence quantum yields of some rhodamine dyes," *Journal of luminescence*, vol. 27, no. 4, pp. 455–462, 1983.

[129] M. Keshmiri, T. Troczynski, and M. Mohseni, "Oxidation of gas phase trichloroethylene and toluene using composite sol–gel tio_2 photocatalytic coatings," *Journal of hazardous materials*, vol. 128, no. 2, pp. 130–137, 2006.

[130] T. Obee and R. Brown, "TiO_2 photocatalysis for indoor air applications: effects of humidity and trace contaminant levels on the oxidation rates of formaldehyde, toluene, and 1, 3-butadiene," *Environmental Science & Technology*, vol. 29, no. 5, pp. 1223–1231, 1995.

[131] T. Noguchi, A. Fujishima, P. Sawunyama, and K. Hashimoto, "Photocatalytic degradation of gaseous formaldehyde using tio2 film," *Environmental science & technology*, vol. 32, no. 23, pp. 3831–3833, 1998.

[132] J. Dalton, P. Janes, N. Jones, J. Nicholson, K. Hallam, and G. Allen, "Photocatalytic oxidation of no_x gases using tio_2: A surface spectroscopic approach," *Environmental Pollution*, vol. 120, no. 2, pp. 415–422, 2002.

[133] T. Ibusuki and K. Takeuchi, "Removal of low concentration nitrogen oxides through photoassisted heterogeneous catalysis," *Journal of molecular Catalysis*, vol. 88, no. 1, pp. 93–102, 1994.

[134] Y. Paz, Z. Luo, L. Rabenberg, and A. Heller, "Photooxidative self-cleaning transparent titanium dioxide films on glass," *Journal of Materials Research*, vol. 10, no. 11, pp. 2842–2848, 1995.

[135] Y. Paz and A. Heller, "Photo-oxidatively self-cleaning transparent titanium dioxide films on soda lime glass: The deleterious effect of sodium contamination and its prevention," *Journal of materials research*, vol. 12, no. 10, pp. 2759–2766, 1997.

[136] J. Yu, X. Zhao, and Q. Zhao, "Effect of surface structure on photocatalytic activity of tio_2 thin films prepared by sol-gel method," *Thin solid films*, vol. 379, no. 1, pp. 7–14, 2000.

[137] Y. Takahashi and Y. Matsuoka, "Dip-coating of tio2 films using a sol derived from ti(o-i-pr)4-diethanolamine-h2o-i-proh system," *Journal of Materials Science*, vol. 23, pp. 2259–2266, 1988. [Online]. Available: http://dx.doi.org/10.1007/BF01115798

[138] K. Kato, A. Tsuzuki, Y. Torii, H. Taoda, T. Kato, and Y. Butsugan, "Morphology of thin anatase coatings prepared from alkoxide solutions containing organic polymer, affecting the photocatalytic decomposition of aqueous acetic acid," *Journal of Materials Science*, vol. 30, pp. 837–841, 1995. [Online]. Available: http://dx.doi.org/10.1007/BF00356349

[139] K. Wang, B. Yao, M. Morris, and J. Holmes, "Supercritical fluid processing of thermally stable mesoporous titania thin films with enhanced photocatalytic activity," *Chemistry of materials*, vol. 17, no. 19, pp. 4825–4831, 2005.

[140] N. Negishi, T. Iyoda, K. Hashimoto, and A. Fujishima, "Preparation of transparent tio_2 thin film photocatalyst and its photocatalytic activity," *Chemistry Letters*, vol. 24, no. 9, pp. 841–842, 1995.

[141] K. Shimizu, H. Imai, H. Hirashima, and K. Tsukuma, "Low-temperature synthesis of anatase thin films on glass and organic substrates by direct deposition from aqueous solutions," *Thin solid films*, vol. 351, no. 1, pp. 220–224, 1999.

[142] H. Imai, M. Matsuta, K. Shimizu, H. Hirashima, and N. Negishi, "Morphology transcription with tio_2 using chemical solution growth and its application for photocatalysts," *Solid state ionics*, vol. 151, no. 1, pp. 183–187, 2002.

[143] Q. Chen, Y. Qian, Z. Chen, W. Wu, Z. Chen, G. Zhou, and Y. Zhang, "Hydrothermal epitaxy of highly oriented tio_2 thin films on silicon," *Applied physics letters*, vol. 66, no. 13, pp. 1608–1610, 1995.

[144] W. Daoud and J. Xin, "Nucleation and growth of anatase crystallites on cotton fabrics at low temperatures," *Journal of the American Ceramic Society*, vol. 87, no. 5, pp. 953–955, 2004.

[145] P. Willmott and J. Huber, "Pulsed laser vaporization and deposition," *Reviews of Modern Physics*, vol. 72, no. 1, p. 315, 2000.

[146] T. Yang, C. Shiu, and M. Wong, "Structure and hydrophilicity of titanium oxide films prepared by electron beam evaporation," *Surface Science*, vol. 548, no. 1, pp. 75–82, 2004.

[147] I. Justicia, P. Ordejón, G. Canto, J. Mozos, J. Fraxedas, G. Battiston, R. Gerbasi, and A. Figueras, "Designed self-doped titanium oxide thin films for efficient visible-light photocatalysis," *Advanced Materials*, vol. 14, no. 19, pp. 1399–1402, 2002.

[148] I. Justicia, G. Garcia, G. Battiston, R. Gerbasi, F. Ager, M. Guerra, J. Caixach, J. Pardo, J. Rivera, and A. Figueras, "Photocatalysis in the visible range of substoichiometric anatase films prepared by mocvd," *Electrochimica acta*, vol. 50, no. 23, pp. 4605–4608, 2005.

[149] A. Mills, N. Elliott, I.P. Parkin, S.A. O'Neill and R.J. Clark, "Novel TiO_2 CVD films for semiconductor photocatalysis," *Journal of Photochemistry and Photobiology A: Chemistry*, vol. 151, pp. 171 – 179, 2002. [Online]. Available: http://www.sciencedirect.com/science/article/pii/S1010603002001909

[150] Bessergenev, VG and Khmelinskii, IV and Pereira, RJF and Krisuk, VV and Turgambaeva, AE and Igumenov, IK, "Preparation of tio_2 films by cvd method and its electrical, structural and optical properties," *Vacuum*, vol. 64, no. 3, pp. 275–279, 2002.

[151] V. Bessergenev, R. Pereira, M. Mateus, I. Khmelinskii, D. Vasconcelos, R. Nicula, E. Burkel, A. Botelho do Rego, and A. Saprykin, "Study of physical and photocatalytic properties of titanium dioxide thin films prepared from complex precursors by chemical vapour deposition," *Thin Solid Films*, vol. 503, no. 1, pp. 29–39, 2006.

[152] C. Guillard, D. Debayle, A. Gagnaire, H. Jaffrezic, and J. Herrmann, "Physical properties and photocatalytic efficiencies of tio_2 films prepared by pecvd and sol–gel methods," *Materials research bulletin*, vol. 39, no. 10, pp. 1445–1458, 2004.

[153] D. Byun, Y. Jin, B. Kim, J. Kee Lee, and D. Park, "Photocatalytic tio_2 deposition by chemical vapor deposition," *Journal of hazardous materials*, vol. 73, no. 2, pp. 199–206, 2000.

[154] O'Neill, S.A. and Robin. JH Clark, and and Parkin, I.P. and Elliott, N. and Mills, A., "Anatase thin films on glass from the chemical vapor deposition of titanium (iv) chloride and ethyl acetate," *Chemistry of materials*, vol. 15, no. 1, pp. 46–50, 2003.

[155] A. Mills, A. Lepre, N. Elliott, S. Bhopal, I. Parkin, and S. OíNeill, "Characterisation of the photocatalyst pilkington activô: a reference film photocatalyst?" *Journal of Photochemistry and Photobiology A: Chemistry*, vol. 160, no. 3, pp. 213–224, 2003.

[156] S. O'Neill, I. Parkin, R. Clark, A. Mills, and N. Elliott, "Atmospheric pressure chemical vapour deposition of titanium dioxide coatings on glass," *Journal of Materials Chemistry*, vol. 13, no. 1, pp. 56–60, 2003.

[157] Y. Guo, X. Zhang, and G. Han, "Investigation of structure and properties of n-doped tio_2 thin films grown by apcvd," *Materials Science and Engineering: B*, vol. 135, no. 2, pp. 83–87, 2006.

[158] P. Sigmund, "Sputtering by ion bombardment theoretical concepts," in *Sputtering by Particle Bombardment I*, ser. Topics in Applied Physics, R. Behrisch, Ed. Springer Berlin Heidelberg, 1981, vol. 47, pp. 9–71.

[159] D. Smith, *Thin-film deposition: principles and practice*. McGraw-Hill New York etc, 1995.

[160] W. Grove, "On the electro-chemical polarity of gases," *Philosophical Transactions of the Royal Society of London*, vol. 142, pp. 87–101, 1852.

[161] P. Sigmund, "Theory of sputtering. i. sputtering yield of amorphous and polycrystalline targets," *Physical Review*, vol. 184, no. 2, p. 383, 1969.

[162] R. Wendt and K. Ellmer, "Desorption of Zn from a growing ZnO: Al-film deposited by magnetron sputtering," *Surface and Coatings Technology*, vol. 93, no. 1, pp. 27–31, 1997.

[163] A. Penfold and J. Thornton, "Electrode type glow discharge apparatus," Patent 3,884,793, 1975, uS Patent.

[164] J. Vossen and W. Kern, *Thin film processes II*. Academic Pr, 1991, vol. 2.

[165] L. Wang, H. Yu, H. Yang, and H. Horng, "Optimum sputtering conditions on the in-situ growth of superconducting $YBa_2Cu_3O_y$ films with an off-axis RF sputtering configuration," *Physica. C. Superconductivity*, vol. 256, no. 1-2, pp. 57–63, 1996.

[166] I. Avci, M. Tepe and D. Abukay, "Effect of deposition conditions on $YBa_2Cu_3O_{7-\delta}$ thin films by inverted cylindrical magnetron sputtering and substrate effects," *Solid State Communications*, vol. 130, no. 5, pp. 357 – 361, 2004. [Online]. Available: http://www.sciencedirect.com/science/article/pii/S0038109804000894

[167] A. Westerheim, L. Yu-Jahnes, and A. Anderson, "Off-axis magnetron sputtering of ybco films: the influence of atomic oxygen," *Magnetics, IEEE Transactions on*, vol. 27, no. 2, pp. 1001–1005, 1991.

[168] J. Kana, J. Ndjaka, P. Ateba, B. Ngom, N. Manyala, O. Nemraoui, A. Beye, and M. Maaza, "Thermochromic vo_2 thin films synthesized by rf-inverted cylindrical magnetron sputtering," *Applied Surface Science*, vol. 254, no. 13, pp. 3959–3963, 2008.

[169] K. Wasa, M. Kitabatake, and H. Adachi, *Thin film materials technology: sputtering of compound materials*. Springer, 2004.

[170] I. Safi, "Recent aspects concerning dc reactive magnetron sputtering of thin films: a review," *Surface and Coatings Technology*, vol. 127, no. 2, pp. 203–218, 2000.

[171] J. Musil, P. Baroch, J. Vlček, K. Nam, and J. Han, "Reactive magnetron sputtering of thin films: present status and trends," *Thin Solid Films*, vol. 475, no. 1, pp. 208–218, 2005.

[172] D. A. Glocker, "Principles and applications of hollow cathode magnetron sputtering sources," in *Proceedings of the Annual SVC Technical Conference*, 1995.

[173] D. Siegfried and D. Cook, "Reactive cylindrical magnetron deposition of titanium nitride and zirconium nitride films," in *39th Annual Technical Conference Proceedings*, 1996.

[174] J. Thornton and V. Hedgcoth, "Tubular hollow cathode sputtering onto substrates of complex shape," *Journal of Vacuum Science and Technology*, vol. 12, no. 1, pp. 93–97, 1975.

[175] V. Lindberg, A. Woodard, and D. Glocker, "Reactive deposition of nitrides and oxides using a twin-cathode inverted cylindrical magnetron," *Surface and Coatings Technology*, vol. 133, pp. 484–488, 2000.

[176] A. Pradhan, S. Shah, and K. Unruh, "Reactive sputter deposition of alumina thin films using a hollow cathode sputtering source," *Review of scientific instruments*, vol. 73, no. 11, pp. 3841–3845, 2002.

[177] K. Chopra and I. Kaur, *Thin film device applications*. Plenum Press, New York, NY, 1983.

[178] R. Stuart, "Vacuum technology, thin films, and sputtering: an introduction," *Orlando, FL, Academic Press, Inc., 1983, 157 p.*, vol. 1, pp. 65–89, 1983.

[179] D. Scaini, Ph.D. dissertation, University of Trieste, 2008.

[180] B. Cullity and S. Stock, *Elements of X-ray Diffraction*. Prentice hall Upper Saddle River, NJ, 2001, vol. 3.

[181] *BRUKER ADVANCED X-RAY SOLUTIONS*, version 4.1.xx ed., Bruker.

[182] R. Bhargava, S. Wang, and J. Koenig, "Ftir microspectroscopy of polymeric systems," *Liquid Chromatography/FTIR Microspectroscopy/Microwave Assisted Synthesis*, pp. 93–96, 2003.

[183] L. Lee, "Characterization of metal and polymer surfaces. vol. 1. metal surfaces," in *Symposium on Advances in Characterization of Metal and Polymer Surfaces, New York*, vol. 5, no. 8, 1976.

[184] S. Wartewig, *IR and Raman Spectroscopy*. Wiley Online Library, 2003.

[185] L. Sawyer, D. Grubb, and G. Meyers, *Polymer microscopy*. Springer, 2008.

[186] D. Bower and W. Maddams, *The vibrational spectroscopy of polymers*. Cambridge University Press, 1992.

[187] J. Koenig, *Infrared and raman spectroscopy of polymers*. Smart Publications, 2001, vol. 134.

[188] S. Johansson, J. Campbell, and K. Malmqvist, "Particle-induced x-ray emission spectrometry," *Chemical Analysis Series*, vol. 133, 1995.

[189] T. Cahill, "Proton microprobes and particle-induced x-ray analytical systems," *Annual Review of Nuclear and Particle Science*, vol. 30, no. 1, pp. 211–252, 1980.

[190] J. Tesmer, M. Nastasi, J. Barbour, C. Maggiore, and J. Mayer, *Handbook of modern ion beam materials analysis*. Materials Research Society Pittsburgh, PA, 1995.

[191] J. Walls, *Methods of surface analysis: techniques and applications*. Cambridge University Press, 1990.

[192] L. Ward, *The optical constants of bulk materials and films*. Institute of Physics Publishing Ltd, 1994.

[193] F. Jenkins and H. White, *Fundamentals of optics*. McGraw-Hill, 1976, vol. 536.

[194] J. Pankove, *Optical processes in semiconductors*. Dover Publications, 2010.

[195] Donald Campbell, Daniel Campbell, Richard Arthur Pethrick, Jim R. White, *Polymer characterization: physical techniques*. CRC Press INC, 2000.

[196] M. Mayer, "Simnra, a simulation program for the analysis of nra, rbs and erda," in *AIP conference proceedings*, vol. 475, 1999, p. 541.

[197] L. Doolittle, "Algorithms for the rapid simulation of rutherford backscattering spectra," *Nuclear Instruments and Methods in Physics Research Section B: Beam Interactions with Materials and Atoms*, vol. 9, no. 3, pp. 344–351, 1985.